Technische Universität Braunschweig

emg

Xiaomei Chen

Atomic Force Microscope (AFM) Cantilevers as Encoder for Real-Time Displacement Measurements

Dissertation
Braunschweig 2011

Berichte aus dem **Institut für Elektrische Messtechnik und Grundlagen der Elektrotechnik**

Band **36**

Hrsg. Prof. Dr. Meinhard Schilling

ATOMIC FORCE MICROSCOPE (AFM) CANTILEVERS AS ENCODER FOR REAL-TIME DISPLACEMENT MEASUREMENTS

Von der Fakultät für Elektrotechnik und Informationstechnik
der Technischen Universität Carolo-Wilhelmina zu Braunschweig

zur Erlangung der Würde
einer Doktor-Ingenieurin (Dr.-Ing.)
genehmigte Dissertation

von: M. Eng. Xiaomei Chen
aus: Heilongjiang, Volksrepublik China

eingereicht am: 21.06.2011
mündliche Prüfung am: 12.10.2011

Referent: Prof. Dr. rer. nat. Meinhard Schilling
Referent: Prof. Dr. rer. nat. Marc Tornow
Vorsitzender: Prof. Dr. rer. nat. Andreas Hangleiter

2011

ATOMIC FORCE MICROSCOPE (AFM) CANTILEVERS AS ENCODER FOR REAL-TIME DISPLACEMENT MEASUREMENTS

Abstract

This thesis proposes that atomic force microscope (AFM) cantilevers be used as encoder for real-time high-resolution displacement measurements.

It first focuses on the displacement decoding mathematics. From the mathematical derivation it is found that four AFM cantilever signals are needed when a 2D sinusoidal grating is paired as a reference for real-time forward and backward displacement measurements in any planar direction, and two AFM cantilevers signals are needed when a 1D sinusoidal grating is paired as the reference for real-time forward and backward displacement measurements in *x*- or *y*-axis direction. Furthermore it demonstrates that so far a tuning fork (TF) cantilever is the best choice among AFM cantilevers for multi cantilevers to be integrated into a compact encoder head.

An AFM with one TF cantilever has been designed and built. The performance and feasibility of one TF cantilever used as encoder for real-time forward or backward displacement measurement has been investigated and experimentally tested. The decoding principle is based on direct count of integer periods plus calculation of two fractional parts of such periods standing at the beginning and at the actual position in the encoded signal corresponding to a given path of displacement. To ensure accurate implementation of this decoding process, a cross-correlation technique has been employed to filter a 1D grating encoded signal in real time. A half sinusoidal waveform template is proved to be very efficient and correct to filter 1D any waveform grating encoded signal by cross- correlating with it.

Finally an AFM head with three TF cantilevers as the encoder has been designed and built. It has been experimentally tested for its performance and feasibility of real-time forward and backward displacement measurements in *x*- or *y*- axis by using two cantilevers if the distance between two cantilever tips in the AFM head is preset by a special piezo in such that two 1D sinusoidal grating position-encoded signals have a quadrature phase shift. By

directly unwrapping the phase between two encoded signals, forward and backward displacements can be detected and measured in real time. Cross-correlation filtering and differentiation process of two encoded signals are found very successful to guarantee the implementation of real-time displacement measurements by suppressing noise and reducing the offset and tilt of the encoded signals.

Rasterkraftmikroskop (AFM) Cantilever als Encoder für Echtzeit Verschiebungsmessungen

Zusammenfassung

Diese Arbeit regt an die Cantilevern von Rasterkraftmikroskopen(AFM) als Encoder für hochauflösende Verschiebungsmessungen in Echtzeit verwendt werde.

In der Arbeit werden zunächst die mathematischen Voraussetzungen der Kodierung und Dekodierung für eine Verschiebemessung betrachtet. In der mathematischen Herleitung wird gezeigt, dass vier unabhängige AFM Cantilever-Signale benötigt werden, um bei einem 2D Sinusgitter als Referenz für laterale Bewegungen die Verschiebung und die Richtung in Echtzeit zu bestimmen. Benutzt man dagegen ein 1D Sinusgitter als Referenz für eindimensionale Bewegungen in x- oder y-Richtung, so benötigt man die Signale zweier AFM Cantilever zur Bestimmung. Außerdem wird gezeigt, dass zurzeit für diesen Zweck „tuning-fork“ (TF) Cantilever die beste Wahl unter den verfügbaren AFM Cantilevern sind, um in einem kompakten Encoderkopf integriert zu werden.

Ein TF Cantilever wurde experimentell in einem AFM hinsichtlich seiner Leistung als AFM Sonde und für die Durchführbarkeit von Verschiebemessungen in beiden Bewegungsrichtungen und in Echtzeit getestet. Das Dekodierungsprinzip für die Bestimmung der Verschiebung mit einem AFM Cantilever beruht auf der direkten Zählung von ganzzahligen Perioden eines Gitters mit bekannter Periode zuzüglich der Teilbereiche am Anfang der Bewegung und an der jeweils aktuellen Position. Zur Verbesserung der Dekodierung ist ein Verfahren mittels Kreuzkorrelation eingesetzt worden, um die codierten Signale eines 1D Gitters in Echtzeit zu filtern. Es ist festgestellt worden, dass eine halbe Sinusschwingung als Vorlage für die Kreuzkorrelation kodierte Signale unterschiedlicher 1D-Wellenformen eines Gitters sehr effizient und genau filtern kann.

Schließlich wurde ein AFM Kopf mit drei TF Cantilevern entworfen und gebaut. Dieser ist hinsichtlich der Leistung und der Durchführbarkeit von Echtzeit-Verschiebungsmessungen in x- oder y- Richtung unter Benutzung von zwei Cantilevern als Encoder untersucht worden. Die Distanz zwischen

den benutzen Cantileverspitzen konnte mittels spezieller Piezos des AFM-Kopfes so eingestellt werden, dass zwischen beiden Signalen eine Phasenverschiebung von 90° lag. Durch Entfaltung der Phase zwischen den beiden Encodersignalen ist es möglich, Vorwärts- und Rückwärtsbewegungen in Echtzeit zu detektieren und zu messen. Kreuzkorrelation und Differenzierung der kodierten Signale sind sehr erfolgreich eingesetzt worden, um durch die damit verbundene Rauschunterdrückung und Reduzierung von Einflüssen durch einen Offset Verschiebemessungen in Echtzeit sicherzustellen.

ACKNOWLEDGEMENTS

Although this thesis prints my name, it wouldn't have been accomplished by going so far toward a very promising direction if it were not the help and support of numerous people behind me. First I would like to express my greatest gratitude to my research supervisor Dr Ludger Koenders, for what he has done for my PhD project: the guidance in theory and practice; the advice from physics and engineering points of view; the support in various aspects, from finance and material to human resource; the tremendous effort and energy he devoted. His solid foundation knowledge on basic theory and plenty of practice experience have set an example for me to follow.

Great thanks should go to Dr Frank Haertig, another supervisor of mine in Physikalische-Technische Bundesanstalt (PTB). This PhD research work is based on his patent on "Verfahren und Vorrichtung zur Bestimmung einer Winkelteilung", in which he put forward the idea of rotation angle measurement by using multi-atomic force microscope (AFM) cantilevers. He also supports my PhD research work from finance and material to human resources. He provided me with opportunity to visit some world renowned coordinate measuring machine (CMM) manufacturers in Germany, which broaden my thought to take a different approach to my PhD work. Many thanks must go to Professor Dr Meinhard Schilling, my supervisor in Technische Universität Braunschweig. He is the speaker of Braunschweig International Graduate School of Metrology (B-IGSM), without hesitating to recruit me as a PhD member in B-IGSM so that I was granted the fellowship to pursue this PhD work from September 2008 to August 2009. Besides intensive and pressing PhD research work, I benefited a lot from the arrangements of diverse topics of lectures, presentations of other PhD students, field trips and international conferences and seminars etc in B-IGSM under his leadership. Those academic events and social practice activities also made my life in Deutschland very pleasant and won't be forgotten in my lifetime. Also I would like to thank Dr Dezhen Li, the course director of B-IGSM, for her help and guide with my academic administration work.

I owe a debt of gratitude to Mr Helmut Wolff for his magic hands and great mind of designing, fabricating and testing three TF AFM cantilevers encoder. I also feel grateful to Mr Holger Neddermeyer for his help with fabricating

and developing printed circuit board (PCB) and other electrical control units. Both are very patient and cooperative.

Of course, at the beginning and progress of my PhD work more or less I got the help or advice from those colleagues of mine in PTB, they are Mr T Dziomba, Mr A Felgner, Mr L Jusko, Mr F Pohlenz, Dr H-U Danzbrink, Dr G Dai, Dr P Thomsen-Schmidt, Dr S Buetefisch, Mr J Pilarczyk, Mr R Popadic etc. I want to give them my best regards.

Finally, but very importantly, I would like to thank my daughter Rachel and my husband Joe, for their great encouragement and support to me for doing whatever I like. I am very thankful to myself for keeping an optimistic, positive, healthy and youthful mind and attitude toward my PhD research and study in Deutschland, although physically I am no longer young and not so healthy.

TABLE OF CONTENTS

1 Introduction of displacement measurement

With the development of nanotechnology, semiconductor lithography and inspection tools as well as mass data of optical disk storage servo writing, real-time displacement measurements and servo control of micro-moving stages with nanometre scale resolution are increasingly demanded. Here the real-time displacement denotes the difference between the path of the initial and the real-time position traversed by it. Except the requirement of high accuracy and high resolution, the displacement measurement techniques have a tendency of development toward

(1) non-contact, low-cost and high speed measurement. Non-contact can guarantee the long-time use of the probing sensor and high speed can save time and increase the production efficiency.
(2) miniaturization, integration and digitalization. Therefore displacement measuring sensors can take only a little space, can easily be integrated into or mounted onto the measured micro-moving stages and can digitally display the measured displacement results in real time.
(3) metrologically direct SI-traceability. It means that the displacement measurement methods directly take optic wavelength as the reference, because SI basic quantity of length – meter is the path traversed by the light during 1/ 299 792 458 seconds in vacuum.

Among the displacement measurement techniques which are commercially available at present, the linear encoders [1] as the sensors, transducers or read heads when paired with the reference scales or gratings to encode position perhaps are the most widely used for displacement measurement in high precision machine tools, especially in metrological instruments ranging from digital callipers to coordinate measuring machines (CMM). Even so, some of the linear encoder such as magnetic one [2], inductive one [3] and capacitive one [4] etc usually only have the resolution down to a micrometer or sub-micrometers. Although optical encoders with new type of physical principle such as Moiré diffraction or holographic etc [5-9] now are investigated to be used for nanometre resolution displacement measurements, their resolution is limited due to the relatively long light wavelength so that typical incremental scales or grating periods vary from hundreds only down to a few micrometers. By using interpolation techniques they can reach the resolutions as fine as one nanometre, nevertheless their accuracy is limited due to the

nonlinearity in the interpolation or due to the complication of optical setup.

1.1 Nanoscale resolution displacement measurement techniques

The techniques that can realize displacement measurement of micro-moving stage in micrometers range and nanometre scale resolution include optical measurement techniques such as laser interferometer, optical grating interferometer and x-ray interferometer; electrical measurement techniques such as inductive sensor and capacitive sensor and scanning probe microscopy (SPM) techniques.

The main specifications of those techniques are listed in table 1.1. The displacement measurement principles based on those techniques will be discussed in the following subsections.

Table 1.1 Comparison between nanometre displacement measurement methods

	Resolution (nm)	Measurement range (nm)	Measurement speed (nm/s)
Laser heterodyne interferometer	< 1	5×10^7	2.5×10^6
X-ray interferometer	< 0.01	2×10^5	3×10^3
Diffraction grating encoder	< 1	5×10^7	10^6
Capacitive position sensor	< 0.01	2.5×10^4	10^6
SPM	< 1	10^3 ~10^5	$<10^3$

1.1.1 Optical measurement

Optical displacement measurement techniques, such as laser interferometer, taking laser wavelength as the reference, metrologically can be directly traced back to SI units. Their measurement resolutions can be enhanced by using such techniques as multiplication of optical path, interpolation of interference fringe, phase-lock multi-frequency and phase demodulation etc. There are

different measurement principles and proposals. They are briefly introduced as follows.

(1) Laser interferometer

Figure 1.1 and figure 1.2 show the typical configuration of the laser interferometric position measurement systems for three axes and one axis plus angle measurements respectively. According to reference [10], the resolution can be as high as 0.1nm and measurement range is up to 2000mm.

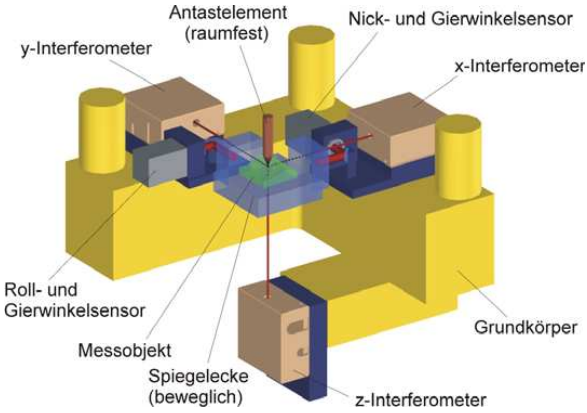

Figure1.1 Interferometers in Nano-positioning and nanomeasuring machine [10].

Figure 1.2 Stage position metrology configuration by using Zygo displacement-measurement interferometer [11].

In both laser interferometers of such high resolution and long measurement range, typical value of the vacuum wavelength for He-Ne laser is 633nm. Thus sub-nanometre resolution is achievable by folding the optical path and interpolating the measurement signal in firmware but mostly in software for several thousand times. Nevertheless, they are generally very bulky and very expensive. Taking SIOS Nanopositioning and Nanomeasuring Machine (NNM) as an example, measurement range is 25 mm × 25 mm × 5 mm, however the mechanical structure takes 420 mm × 420 mm × 340 mm (length × width × height). If laser interferometer is used for long displacement measurement, or applied for time-consuming position monitoring such as fabrication of larger scale integrated circuit, the changes of ambient temperature, atmospheric pressure and moisture etc have to be taken into account to avoid generating larger measurement errors. Usually laser interferometers require complex sensors to sense slight ambient changes to compensate the displacement measurement errors caused by the change of ambient conditions by using the algorithm. The measurement accuracy is restrained by its nonlinearity which is caused by many reasons.

(2) X-ray interferometer

X-ray interferometer, using the short distances of crystalline lattice, e.g. 0.192nm for lattice spacing of the silicon (220) crystal as the reference, has the potential of high resolution. The principle of transmission X-ray interferometer is illustrated in figure 1.3 (a).

Three thin crystal lamellas (LLL) constitute the X-ray-optical components at which the X-rays are - by means of Bragg reflection - in the first lamella S split up, in the second M deflected and in the third A superposed for interference. As the magnitudes of the X-ray wavelength and the lattice parameter are of comparable order, the splitting angles are relatively large and the interference pattern reacts sensitively to relative movements of the crystal lamellas. This characteristic is employed for the measurement of the lattice parameter in the unit of length – meter. To ensure adequate stability, the whole interferometer is cut from a single crystal block, leaving three thin crystal lamellas S, M and A standing on one base as shown in figure 1.3 (b).

Since first proposed and experimented three thin crystal lamellas (LLL) X-ray interferometer was reported [12], it seems that it had been used to investigate measurement tasks in nanotechnology as, for example, the

calibration of transfer length standards for scanning tunnel microscopy and verification of the interpolation procedures in light interferometer [13-14] within several internationally prominent metrology institutes such as PTB and National Physics Laboratory (NPL) before 2000. However due to its complexity, full-scale application of this X-ray method in industrial practice is not possible yet [15].

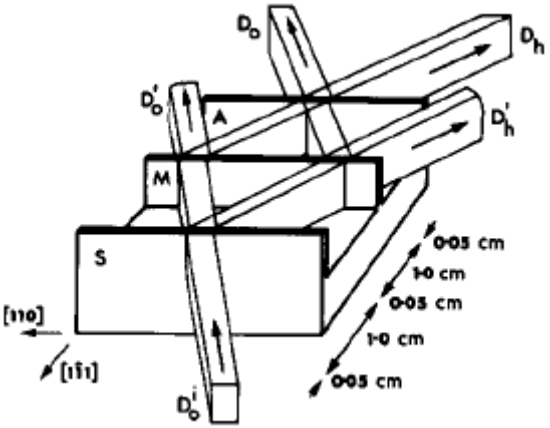

(a)

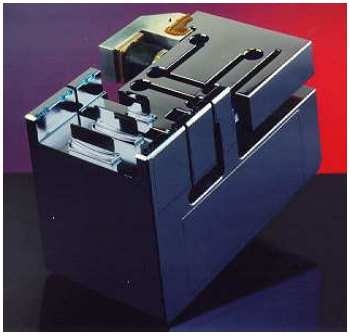

(b)

Figure 1.3 X-ray interferometer schematic in (a) [12] and its prototype in (b) [15].

（3）Laser diffraction grating interferometer [16-18]

A typical laser diffraction grating interferometer shown in figure 1.4 (a) employs a single, reflecting diffraction grating operating as both the beam splitter and the reference surface. The measured displacement no longer affects the optical path difference. The reference is changed from laser wavelength to the pitch of the grating. A laser beam from the laser diode (LD) emits directly onto the surface of a diffraction grating and is diffracted into two separate beams, namely a test beam and a reference beam. The diffraction beams of +1 order and -1 order are half reflected and half transmitted by a beam splitter (BS) respectively onto photo detector D1 and D2 and generate interference signals that can be processed to be converted into displacement of the grating. With electrical interpolation, it is possible to achieve sub-nanometre in resolution and several millimetres in measurement range.

However, the latest optical heterodyne grating interferometer [18] which can achieve such a high measurement resolution as 3nm actually has such a complicated and bulky optical system as shown in figure 1.4 (b).

1.1.2 Electrical measurement - capacitive position sensor

The resolution of a capacitive position sensor can also reach sub-nanometre scale. Linearity of the capacitive position sensors is on the order of 0.10-0.20% of full measuring range of 10 μm ~ 500 μm, and repeatability is highly dependent on ambient condition, but can be on the order of two to five times the resolution. Resolution is on the order of 1 part in full measuring range. They are compact and low cost. For dual-plate capacitive position sensor, at present the measurement range can reach several hundreds of micrometers [19].

The dual-plate capacitive position sensor has such a measurement principle: two conductive surfaces with short distance in between setup an electric field, and the applied voltage is proportional to the distance between the plates shown in figure 1.5. Dual-plate sensors measure the distance between two well-defined sensor plates 1 and 2 with carefully aligned surfaces which generate the most accurate electric field and hence provide optimal results.

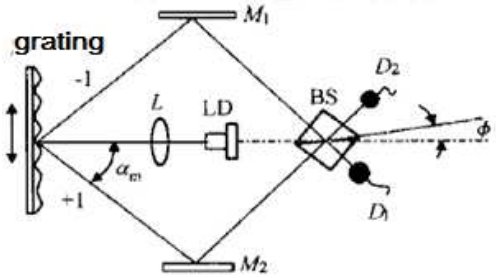

(a)

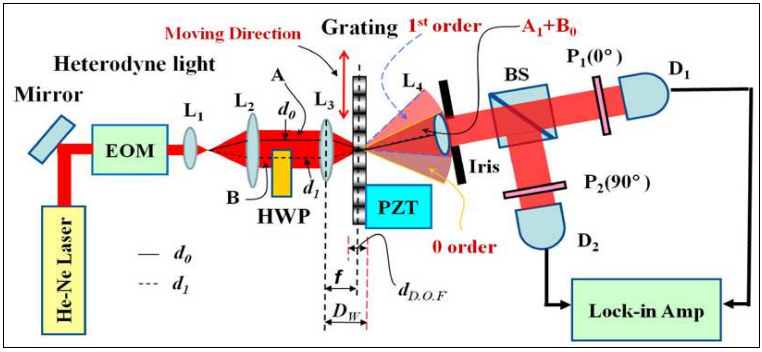

(b)

Figure 1.4 (a) A typical laser diffraction grating interferometer; (b) a high resolution optical heterodyne grating interferometer [18].

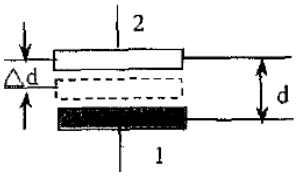

Figure 1.5 Schematic of capacitive position sensor

Capacitive position sensors have wide measurement range and high resolution. But they also have high requirements to the ambient conditions. The changes of temperature, moisture, internal frame structure and electrical circuit etc have influence on their accuracies and sensitivities, therefore at

present they need to be calibrated frequently by using an interferometer or other means which can metrologically trace the capacitance change caused by displacement back to SI unit.

1.3.3 Scanning probe microscopy (SPM)

1.3.3.1 Brief introduction

Scanning probe microscopes (SPMs) are a family of instruments used for studying surface properties of the material from the micron level down to the atomic level. Generally SPMs contain the components illustrated in figure 1.6, in which two fundamental components that make SPM possible are the probe and the scanner or especially the piezoelectric scanner.

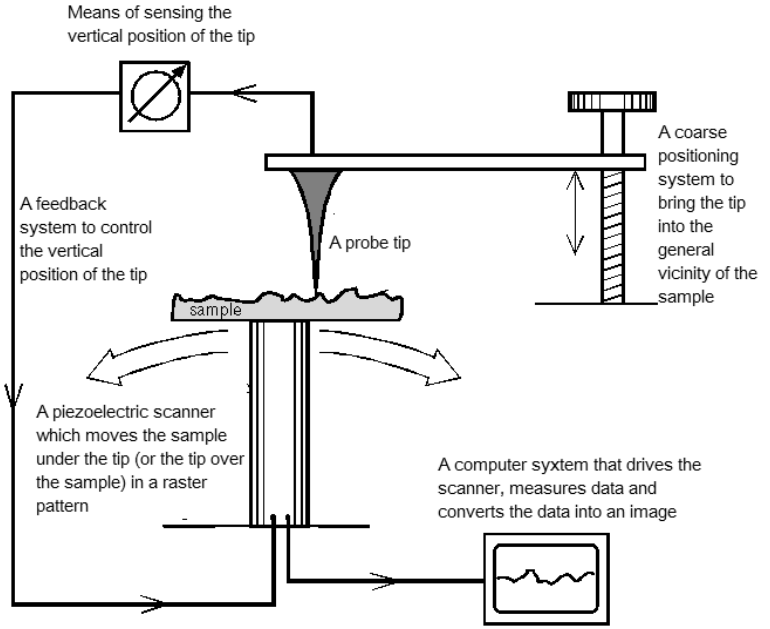

Figure 1.6 Schematic of generalized SPM. From reference [20].

Reference [21] describes that the probe is the point of interface between the SPM and the sample. When two materials are brought very close together, various interactions forces are present at the atomic level. An SPM probe is particularly sensitive to such interaction forces and is designed to sense them. The piezoelectric scanner is used to control the precise position of the probe in relation to the surface both vertically and laterally. Vertically it can bring an SPM probe close to or leave far away from a sample surface, and laterally the piezoelectric scanner controls the probe to scan over the sample surface precisely with the control help of *z* feedback system shown in figure 1.6. As a result the magnitudes of interaction force variation as a function of the probe-sample distance can be detected by the sensing element in figure 1.6, and the sample surface topographic data can be mapped or imaged.

Based on different means of sensing elements and different principles of the probes, there are mainly scanning tunneling microscope (STM), atomic force microscope (AFM) and near-field scanning optical microscope (NSOM) in an SPM family. They are concisely introduced in Appendix A.

1.3.3.2 SPM as encoder for displacement measurement

Up to now in SPM family, especially STM and AFM are used in a large variety of disciplines, including fundamental surface science, surface roughness measurement, and three-dimensional imaging—from atoms of silicon to micron-sized particles. In general, they are used to measure physical properties such as surface conductivity, static charge distribution, localized friction, magnetic fields, and elastic modulus etc by detecting different tip-sample interactions. In the nanometre dimension metrology area, only AFM, especially metrological AFM and critical dimension (CD) AFM have been successfully applied to measure the pitches of periodic patterns such as line-scales or gratings [24-26].

In another case, SPM probe can also sense the position changes of a periodic pattern such as a line-scale or a grating, when it is moved with piezoelectric micro-scanning stage if its parameters, especially the pitch of the grating, are well defined and well calibrated. Just like optical encoders mentioned at the beginning of this chapter, an SPM probe tip scans the periodic pattern to convert the encoded position into an analogue or digital signal. With the

knowledge of the pitch and decoding criteria briefly introduced below, the periodic pattern position-encoded signal can be decoded into displacement with high resolution. Therefore it is possible to determine the displacement and the position.

When paired with crystalline lattice, STM technology has been explored by several people for the position or displacement measurement [27-33].

H. Kawakatsu et al were the very first who used a crystalline lattice for metrology and positioning control [27]. They built dual-tunneling unit (DTU) STM with an objective of developing a positioning and measuring device, which uses the crystalline lattice as a reference scale, one tunneling unit to realize a crystal reference *x-y* positioning table and another tunneling unit to measure other samples such as micro electromechanical system (MEMS) [28] or another crystals [29] by counting the number of lattices. For counting the number of lattices, the STM tip has to be dithered at high frequency to track the apexes of the atoms. It seems that it failed to count the lattice number as a result in reference [28] and [29] because the length comparison was done by comparing image of crystals for *x-y* positioning table with the image of other samples.

Tetsuo Ohara, once a PhD researcher at Massachusetts Institute of Technology (MIT) in his thesis in 1995 [30] first proposed an idea to use SPM or specially STM [31] paired with 1D sinusoidal and non-sinusoidal reference scale as well as grid reference scale to measure high precision position. Later on this proposed high precision and high speed position measurement system was defined as scanning probe position encoder (SPPE) [32].

In the proposed system shown in figure 1.7, the reference scale is attached to the surface whose position must be controlled to move, the sensor probe measures the real-time position of the reference scale. This information is fed back through a computer to the control system to control the surface movement along the axis. The sensor probe is oscillated at high frequency with amplitude from submicron to several nanometres while it scans the reference scale. The probe oscillates in linear motion for 1D position sensing and circular motion for 2D position sensing as shown in figure 1.7 (a) and figure 1.7 (b) respectively.

Based on the oscillation of the sensor probe, the position decoding mathematic models have been derived by him. Then a position sensor prototype by using an STM was setup. However, except for a STM image of graphite and the topography signal of a grating with 200 nm in pitch, no position measurement result was presented then. Even today, 15 years later, SPM has been highly developed, nevertheless, SPPE technique was only successfully applied to a scanning interference optical encoder [33].

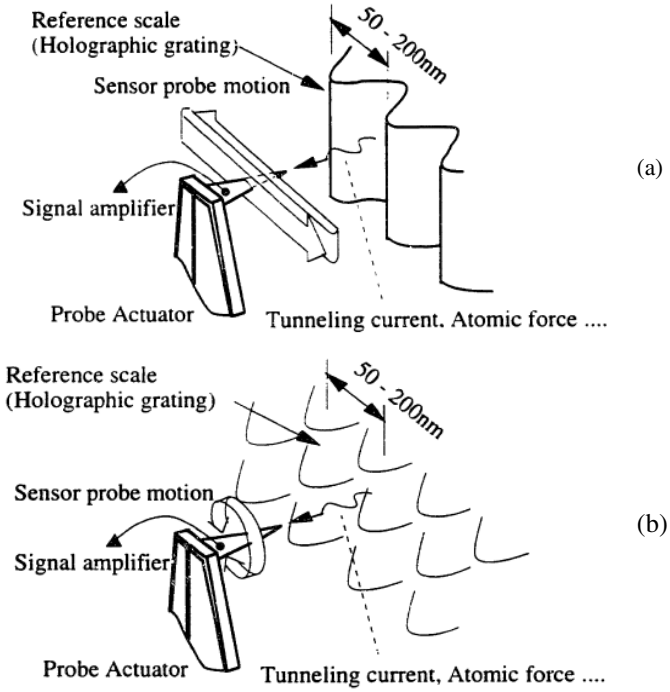

Figure 1.7 Schematic of SPPE: probe oscillates linearly in (a) and circularly in (b) [32]

From 1997 to 1999, M Aketagawa and his group have published several papers which described the comparative length measurement in the range of 1μm in 1997 and 5μm in 1999 using a regular crystalline lattice as a reference scale and a dual tuning unit-STM (DTU-STM) as a detector [34-35]. The DTU-STM shown in figure 1.8 with one *x-y* stage and two tunneling units independently controlled in z axis direction was utilized for

comparative length measurement, which means two samples of highly oriented pyrolytic graphite (HOPG) were put on the x-y scanning table under the two tunneling units. The displacement was determined by counting the number of "visible" lattice points (0.246nm) in the STM image along the displacement direction offline but not online or in real time.

Ten years later starting from 2007, M Aketagawa et al in their published papers [36-38] described the setup of real-time atomic encoder by using only one tunneling unit of DTU-STM and regular crystalline surface. The displacement was determined by a new decoding technique—STM tip lateral circular dithers on multi specific points on the HOPG crystalline surface to be considered as multi-tunneling-probes. When multi-points satisfy some relationship on the HOPG crystalline surface on the *x-y* scanning stage, the 2D displacement of STM tip relative to *x-y* scanning stage can be determined from the multi-current signals corresponding to the multi-points. The most successful experiment was done based on six-points [38].

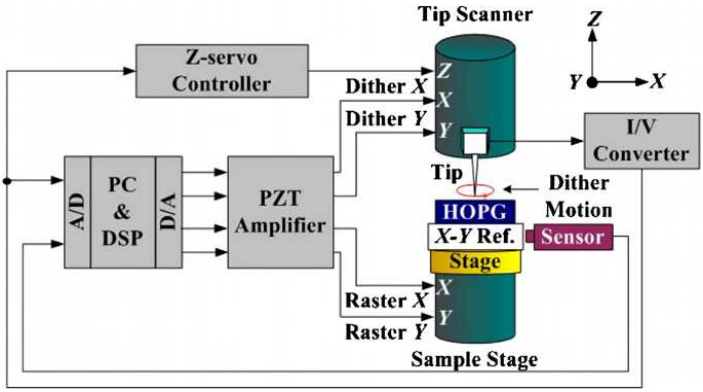

Figure 1.8 Schematic of DTU-STM encoder [38].

Aketagawa has applied STM as atomic encoder combined with HOPG crystalline lattice and tried to achieve the real-time displacement measurements. This was a significant advance in the exploration of the displacement measurements that are based on crystalline gratings.

However, the application of STM is limited to electrically conductive samples. This problem can be solved by using AFM techniques that are

capable of achieving atomic resolution on crystalline surfaces [39]. AFM cantilevers can sense the position changes of a line-scale or grating, when it linearly moves or it rotates with micro-scanning stage if its parameters especially the pitch is well defined and well calibrated. Especially F Haertig et al in their patent on "Verfahren und Vorrichtung zur Bestimmung einer Winkelteilung" put forward the idea of rotation angle measurement by using multi-AFM cantilevers [40].

It is the theme of this thesis: finding and testing some decoding techniques to convert the line-scales or gratings position-encoded signal probed by AFM cantilevers into the position so as to determine the displacement in real time.

The decoding principles which are implied in this thesis and mathematics modelling are explained in chapter 2.

A prototype of one cantilever AFM has been designed, built and experimentally tested in chapter 3.

In chapter 4, for the feasibility study of known direction (forward or backward) real-time displacement measurement, by using one AFM cantilever as encoder, the decoding principle, real-time filtering of encoded signal and mathematics modelling behind this filtering technique are explained. In this chapter the experiments and results on known direction real-time displacement, specifications such as resolution, repeatability and speed etc of displacement measurement are presented too.

In chapter 5, a prototype of an AFM head with three cantilevers has been designed, built and experimentally tested.

In chapter 6, for the feasibility study of real-time forward and backward displacement measurement in *x*- or *y*- axis by using two AFM cantilevers, the decoding principle by using two AFM cantilevers is reiterated. The algorithm of unwrapping the quadrature phase is explained. Experiments and results of real-time filtering process and differentiation process of the encoded signal, real-time forward and backward displacement measurements and comparison of decoding methods of one AFM cantilever encoder and two AFM cantilevers encoder are presented in this chapter.

Finally conclusion is drawn and prospects are surveyed in chapter 7.

2 Mathematics and principle - AFM cantilevers as encoder to measure displacement in real time

2.1 Introduction

AFM displacement measurement technique can definitely reach nanometre and sub-nanometre measurement resolution. Although in metrology it cannot be directly traced back to SI units, it can be traced back indirectly to SI units when it is paired with a reference scale or grating whose parameters especially the pitch is well known and well calibrated just as optical, capacitive and other encoders do. A reference scale or grating position-encoded signal probed by one AFM cantilever is the topography of its surface. The principle to decode the encoded signals into the displacement of a reference will be discussed in this chapter.

2.2 In-plane an arbitrary direction displacement in real time

At a given time, for an arbitrary α direction displacement, considering a 2D sinusoidal grating as the reference pairs with AFM cantilevers. A 2D sinusoidal grating is simulated in Figure 2.1 with pitch of P and amplitude of $2A$. As defined in reference [21], the point of interface between the AFM and the sample represents cantilever tip.

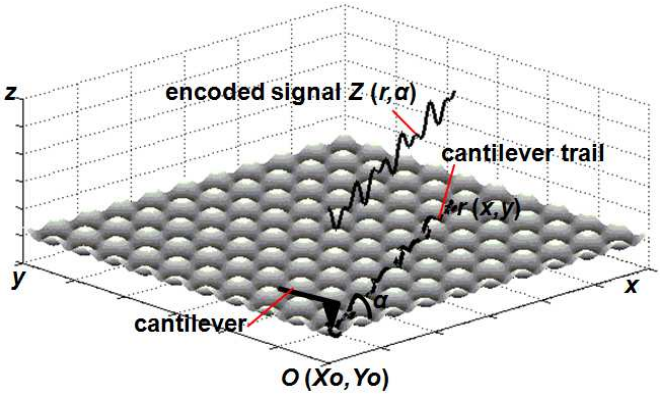

Figure 2.1 Schematic of AFM cantilever to encode 2D sinusoidal grating position r along α direction.

2D sinusoidal grating topography can be mathematically expressed as

$$z = f(x, y) = Ax \cdot \sin(\frac{2\pi}{Xp} x) + Ay \cdot \sin(\frac{2\pi}{Yp} y) \qquad (2\text{-}1)$$

where Xp and Yp are the pitches along x- and y-axis of 2D sinusoidal grating respectively, Ax and Ay are the amplitudes along x- and y-axis of 2D sinusoidal grating. It is supposed that $Xp = Yp = P$, and $Ax = Ay = A$. If 2D sinusoidal grating starts moving relatively to AFM cantilever tip from an initial position $O(X_0,Y_0)$ to a position $r(x,y)$ along an arbitrary α direction, the displacement r can be resolved into $x = r\cdot\cos\alpha + X_0$ and $y = r\cdot\sin\alpha + Y_0$. If all those four algebraic expressions are put back into equation (2-1), 2D sinusoidal grating encoded signal probed by one AFM cantilever along α direction can be expressed as

$$Z(r,\alpha) = f(r,\alpha) = A\sin[\frac{2\pi}{P}(r\cos\alpha + X_0)] + A\sin[\frac{2\pi}{P}(r\sin\alpha + Y_0)] \qquad (2\text{-}2)$$

If equation (2-2) is evolved, four unknown variables have been found, they are:

$$\gamma = \sin(\frac{2\pi}{P} \cdot r \cdot \cos\alpha) \qquad (2\text{-}3)$$

$$\eta = \cos(\frac{2\pi}{P} \cdot r \cdot \cos\alpha) \qquad (2\text{-}4)$$

$$\psi = \sin(\frac{2\pi}{P} \cdot r \cdot \sin\alpha) \qquad (2\text{-}5)$$

$$\zeta = \cos(\frac{2\pi}{P} \cdot r \cdot \sin\alpha) \qquad (2\text{-}6)$$

This means for the displacement r in an arbitrary α direction, four signals or four AFM cantilevers are needed.

Four independently AFM cantilever tips are put at positions of $S(X_S,Y_S)$, $T(X_T,Y_T)$, $U(X_U,Y_U)$ and $V(X_V,Y_V)$ respectively, and the positions are randomly selected as shown in figure 2.2. If they all equally move a distance r in α direction from the initial position, the four 2D sinusoidal grating position-encoded signals probed by AFM cantilever S, T, U and V in α direction can be respectively expressed as

$$Z_S(r,\alpha) = A\sin[\frac{2\pi}{P}(r\cdot\cos\alpha + X_S)] + A\sin[\frac{2\pi}{P}(r\cdot\sin\alpha + Y_S)] \qquad (2\text{-}7)$$

$$Z_T(r,\alpha) = A\sin[\frac{2\pi}{P}(r\cdot\cos\alpha + X_T)] + A\sin[\frac{2\pi}{P}(r\cdot\sin\alpha + Y_T)] \quad (2\text{-}8)$$

$$Z_U(r,\alpha) = A\sin[\frac{2\pi}{P}(r\cdot\cos\alpha + X_U)] + A\sin[\frac{2\pi}{P}(r\cdot\sin\alpha + Y_U)] \quad (2\text{-}9)$$

$$Z_V(r,\alpha) = A\sin[\frac{2\pi}{P}(r\cdot\cos\alpha + X_V)] + A\sin[\frac{2\pi}{P}(r\cdot\sin\alpha + Y_V)] \quad (2\text{-}10)$$

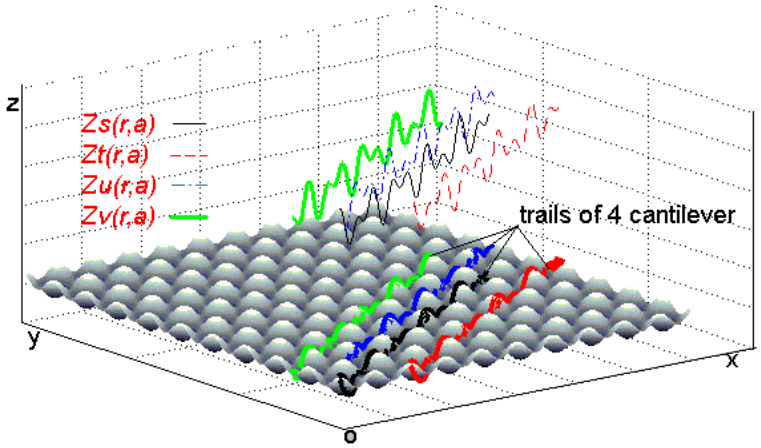

Figure 2.2 Schematic of four randomly positioned AFM cantilevers encoding 2D sinusoidal grating position along r direction.

Equation (2-7), (2-8), (2-9) and (2-10) can be evolved respectively as

$$Z_s(r,\alpha) = A\sin(\frac{2\pi}{P}\cdot r\cdot\cos\alpha)\cdot\cos(\frac{2\pi}{P}\cdot X_S) + A\cos(\frac{2\pi}{P}\cdot r\cdot\cos\alpha)\cdot\sin(\frac{2\pi}{P}\cdot X_S) \quad (2\text{-}11)$$
$$+A\sin(\frac{2\pi}{P}\cdot r\cdot\sin\alpha)\cdot\cos(\frac{2\pi}{P}\cdot Y_S) + A\cos(\frac{2\pi}{P}\cdot r\cdot\sin\alpha)\cdot\sin(\frac{2\pi}{P}\cdot Y_S)$$

$$Z_T(r,\alpha) = A\sin(\frac{2\pi}{P}\cdot r\cdot\cos\alpha)\cdot\cos(\frac{2\pi}{P}\cdot X_T) + A\cos(\frac{2\pi}{P}\cdot r\cdot\cos\alpha)\cdot\sin(\frac{2\pi}{P}\cdot X_T) \quad (2\text{-}12)$$
$$+A\sin(\frac{2\pi}{P}\cdot r\cdot\sin\alpha)\cdot\cos(\frac{2\pi}{P}\cdot Y_T) + A\cos(\frac{2\pi}{P}\cdot r\cdot\sin\alpha)\cdot\sin(\frac{2\pi}{P}\cdot Y_T)$$

$$Z_U(r,\alpha) = A\sin(\frac{2\pi}{P}\cdot r\cdot\cos\alpha)\cdot\cos(\frac{2\pi}{P}\cdot X_U) + A\cos(\frac{2\pi}{P}\cdot r\cdot\cos\alpha)\cdot\sin(\frac{2\pi}{P}\cdot X_U) \quad (2\text{-}13)$$
$$+A\sin(\frac{2\pi}{P}\cdot r\cdot\sin\alpha)\cdot\cos(\frac{2\pi}{P}\cdot Y_U) + A\cos(\frac{2\pi}{P}\cdot r\cdot\sin\alpha)\cdot\sin(\frac{2\pi}{P}\cdot Y_U)$$

$$Z_V(r,\alpha) = A\sin(\frac{2\pi}{P}\cdot r\cdot\cos\alpha)\cdot\cos(\frac{2\pi}{P}\cdot X_V) + A\cos(\frac{2\pi}{P}\cdot r\cdot\cos\alpha)\cdot\sin(\frac{2\pi}{P}\cdot X_V) \quad (2\text{-}14)$$
$$+A\sin(\frac{2\pi}{P}\cdot r\cdot\sin\alpha)\cdot\cos(\frac{2\pi}{P}\cdot Y_V) + A\cos(\frac{2\pi}{P}\cdot r\cdot\sin\alpha)\cdot\sin(\frac{2\pi}{P}\cdot Y_V)$$

If in equation (2-11) ~ (2-14), following constants are set,

$$\begin{cases} a_1 = A\cos(\frac{2\pi}{P}\cdot X_s) \\ b_1 = A\sin(\frac{2\pi}{P}\cdot X_s) \\ c_1 = A\cos(\frac{2\pi}{P}\cdot Y_s) \\ d_1 = A\sin(\frac{2\pi}{P}\cdot Y_s) \end{cases} \quad (2\text{-}15) \qquad \begin{cases} a_2 = A\cos(\frac{2\pi}{P}\cdot X_T) \\ b_2 = A\sin(\frac{2\pi}{P}\cdot X_T) \\ c_2 = A\cos(\frac{2\pi}{P}\cdot Y_T) \\ d_2 = A\sin(\frac{2\pi}{P}\cdot Y_T) \end{cases} \quad (2\text{-}16)$$

$$\begin{cases} a_3 = A\cos(\frac{2\pi}{P}\cdot X_U) \\ b_3 = A\sin(\frac{2\pi}{P}\cdot X_U) \\ c_3 = A\cos(\frac{2\pi}{P}\cdot Y_U) \\ d_3 = A\sin(\frac{2\pi}{P}\cdot Y_U) \end{cases} \quad (2\text{-}17) \qquad \begin{cases} a_4 = A\cos(\frac{2\pi}{P}\cdot X_V) \\ b_4 = A\sin(\frac{2\pi}{P}\cdot X_V) \\ c_4 = A\cos(\frac{2\pi}{P}\cdot Y_V) \\ d_4 = A\sin(\frac{2\pi}{P}\cdot Y_V) \end{cases} \quad (2\text{-}18)$$

and if those constants and four unknown parameters in equations (2-3) ~ (2-6) are also put into equations (2-11) ~ (2-14), they can be expressed as the system of linear equations with four unknown parameters:

$$\begin{cases} a_1\gamma + b_1\eta + c_1\psi + d_1\zeta = Z_s(r,\alpha) \\ a_2\gamma + b_2\eta + c_2\psi + d_2\zeta = Z_T(r,\alpha) \\ a_3\gamma + b_3\eta + c_3\psi + d_3\zeta = Z_U(r,\alpha) \\ a_4\gamma + b_4\eta + c_4\psi + d_4\zeta = Z_V(r,\alpha) \end{cases} \quad (2\text{-}19)$$

Equation (2-19) can be changed into the matrix form as

$$\begin{bmatrix} a_1 & b_1 & c_1 & d_1 \\ a_2 & b_2 & c_2 & d_2 \\ a_3 & b_3 & c_3 & d_3 \\ a_4 & b_4 & c_4 & d_4 \end{bmatrix} \begin{bmatrix} \gamma \\ \eta \\ \psi \\ \zeta \end{bmatrix} = \begin{bmatrix} Z_S(r,\alpha) \\ Z_T(r,\alpha) \\ Z_U(r,\alpha) \\ Z_V(r,\alpha) \end{bmatrix} \tag{2-20}$$

From the system of linear equations (2-19), it can be derived that

$$r \cdot \cos\alpha = P \cdot \arcsin\gamma/(2\pi) \tag{2-21}$$
$$r \cdot \cos\alpha = P \cdot \arccos\eta/(2\pi) \tag{2-22}$$
$$r \cdot \sin\alpha = P \cdot \arcsin\psi/(2\pi) \tag{2-23}$$
$$r \cdot \sin\alpha = P \cdot \arccos\zeta/(2\pi) \tag{2-24}$$

and

$$\arcsin\gamma = \arccos\eta \tag{2-25}$$
$$\arcsin\psi = \arccos\zeta \tag{2-26}$$

From a pair of equations either (2-21) and (2-23) or (2-22) and (2-24), r and α can be derived as

$$r = \frac{P}{2\pi}\left|(\arcsin^2\gamma + \arcsin^2\psi)^{\frac{1}{2}}\right| \tag{2-27}$$

or

$$r = \frac{P}{2\pi}\left|(\arccos^2\eta + \arccos^2\zeta)^{\frac{1}{2}}\right| \tag{2-28}$$

and

$$\alpha = \arctan\left(\frac{\arcsin\psi}{\arcsin\gamma}\right) \tag{2-29}$$

or

$$\alpha = \arctan\left(\frac{\arccos\zeta}{\arccos\eta}\right) \tag{2-30}$$

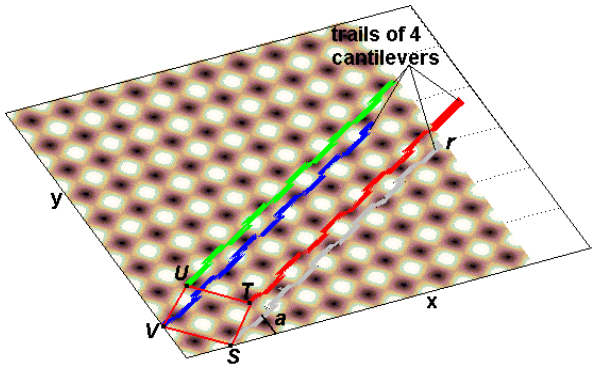

Figure 2.3 Four AFM cantilever tips regularly positioned in diamond shape.

Especially if four AFM cantilever tips are regularly put at $S(0,0)$, $T[(n+\frac{1}{4})P,(n+\frac{1}{4})P]$, $U[0,(2n+\frac{1}{2})P]$, $V[-(n+\frac{1}{4})P,(n+\frac{1}{4})P]$ ($n=1,2,\cdots$) respectively on the 2D sinusoidal grating so that four tips form a diamond shape shown in figure 2.3, the linear equations with four unknown variables have been expressed as:

$$\begin{cases} Z_S(r,\alpha)=A\sin[\frac{2\pi}{P}r\cos\alpha]+A\sin[\frac{2\pi}{P}r\sin\alpha] \\ Z_T(r,\alpha)=A\sin[\frac{2\pi}{P}(r\cos\alpha+(n+\frac{1}{4})P)]+A\sin[\frac{2\pi}{P}(r\sin\alpha+(n+\frac{1}{4})P)] \\ Z_U(r,\alpha)=A\sin[\frac{2\pi}{P}r\cos\alpha]+A\sin[\frac{2\pi}{P}(r\sin\alpha+(2n+\frac{1}{2})P)] \\ Z_V(r,\alpha)=A\sin[\frac{2\pi}{P}(r\cos\alpha-(n+\frac{1}{4})P)]+A\sin[\frac{2\pi}{P}(r\sin\alpha+(n+\frac{1}{4})P)] \end{cases} \tag{2-31}$$

Equation group (2-31) is simplified as

$$\begin{cases} Z_S(r,\alpha)=A\sin[\frac{2\pi}{P}r\cos\alpha]+A\sin[\frac{2\pi}{P}r\sin\alpha] \\ Z_T(r,\alpha)=A\cos[\frac{2\pi}{P}(r\cos\alpha)]+A\cos[\frac{2\pi}{P}(r\sin\alpha)] \\ Z_U(r,\alpha)=A\sin[\frac{2\pi}{P}r\cos\alpha]-A\sin[\frac{2\pi}{P}(r\sin\alpha)] \\ Z_V(r,\alpha)=-A\cos[\frac{2\pi}{P}(r\cos\alpha)]+A\cos[\frac{2\pi}{P}(r\sin\alpha)] \end{cases} \tag{2-32}$$

In this situation, the solution of equations (2-32) can be represented by equation (2-33) and (2-34), which are the mathematical decoding methods for the displacement *r* and arbitrary direction α.

$$r = \frac{P}{2\pi}(\arctan^2 \frac{z_S + z_U}{z_T - z_V} + \arctan^2 \frac{z_S - z_U}{z_T + z_V})^{\frac{1}{2}} \tag{2-33}$$

$$\alpha = \arctan(\frac{\arctan \frac{z_S - z_U}{z_T + z_V}}{\arctan \frac{z_S + z_U}{z_T - z_V}}) \tag{2-34}$$

From equation (2-33), it can be seen that *r* is a periodically trigonometric function of the arithmetic operation of Z_S, Z_T, Z_U, Z_V. They are the signals picked-up respectively by four AFM cantilevers. Therefore for the displacement decoding in an arbitrary direction α, the integer periods count and fractional period calculation are needed. However, the period is difficult to be decided from equation (2-33).

2.3 Displacement in *x*- or *y*-axis direction in real time

In equation (2-32) if $\alpha = 0$, $Z_S(x) = Z_U(x)$ and $Z_T(x) = -Z_V(x)$. It means for *x*-axis displacement measurement only two AFM cantilevers are needed, for example, cantilevers *U* and *T*. In this situation, instead of a 2D sinusoidal grating, a 1D sinusoidal grating as the reference to pair with two AFM cantilevers is enough to encode sinusoidal grating position if 1D sinusoidal grating line is perpendicular to *x*-axis.

If one cantilever tip is motionless and another cantilever tip is controlled in advance moving to such a position that the distance of two tips in *x*-axis is equal to $(N+1/4)\cdot P$ (N=1, 2…), the phase shift between two position-encoded signals is about $\pi/2$, which means that the coordinates of two cantilevers are $U(X_0)$, $T[X_0 + (N + \frac{1}{4})P]$ $(N = 1, 2, \cdots)$ as shown in figure 2.4. In such case, two 1D sinusoidal grating position-encoded signals are

$$\begin{cases} Z_U(x) = A\sin(\frac{2\pi}{P}x) \\ Z_T(x) = A\cos(\frac{2\pi}{P}x) \end{cases} \tag{2-35}$$

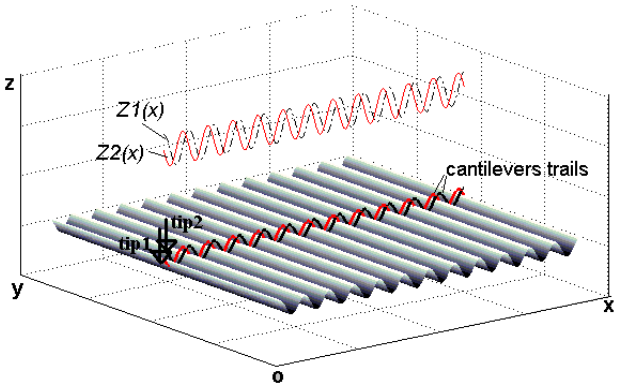

Figure 2.4 Two AFM cantilevers are positioned regularly on 1D sinusoidal grating surface.

The two encoded signals expressed in (2-35), sine component and cosine component, have a quadrature phase shift. Therefore the mathematical decoding for displacement x can be expressed as

$$x = \frac{P}{2\pi}\arctan(\frac{Z_U}{Z_T}) \tag{2-36}$$

From equation (2-36), it can be noticed that x is a periodically arc tangent function of the arithmetic ratio of two quadrature signal components Z_U and Z_T which are probed respectively by two AFM cantilevers *U* and *T*.

In the same way, for *y*-axis (α=90°) displacement measurement only two AFM cantilevers are needed too, for example cantilevers *S* and *V*. Again, instead of a 2D sinusoidal grating, a 1D sinusoidal grating as the reference to pair with two AFM cantilevers is enough to encode sinusoidal grating position. If one cantilever tip is motionless and another cantilever tip is position-controlled in advance to such a position that the distance of two tips in *y*-axis is equal to $(N+1/4)\cdot P$ (N=1, 2…) too, the phase difference between two position-encoded signals is $\pi/2$, which means that the coordinates of two AFM cantilever tips are $S(Y_0)$,

$V[Y_0 + (N + \frac{1}{4})P]$ ($N = 1, 2, \cdots$), respectively. In such a case, two 1D sinusoidal grating position-encoded signals are

$$\begin{cases} Z_S(y) = A\sin(\frac{2\pi}{P}y) \\ Z_V(y) = A\cos(\frac{2\pi}{P}y) \end{cases} \tag{2-37}$$

Then the mathematical decoding for displacement y will be expressed as

$$y = \frac{P}{2\pi}\arctan(\frac{Z_S}{Z_V}) \tag{2-38}$$

From equation (2-38), it can also be noticed that y is periodically arc tangent function of the arithmetic ratio of two quadrature signal components Z_S and Z_V which are probed respectively by two AFM cantilevers *S* and *V*.

2.4 Criteria on design and development of AFM cantilevers encoder

One of the important and desirable characteristics of a sensor head used in displacement measurement is its compactness. A compact sensor head can detect the cantilever deflection within a very small area or space, thus multiple AFM cantilevers could be used without jeopardizing the compactness of the sensor head. Since the decoding mathematics in the previous section of this chapter indicates that four AFM cantilevers are needed for arbitrary direction displacement and two AFM cantilevers with elaborately arranged position relationship are needed for displacements in the direction perpendicular to 1D grating lines, and following factors should be very carefully considered for the selection of AFM cantilever type and its deflection detecting method when an integrated multi-AFM cantilevers encoder is needed to be designed and developed.

The mechanical schematic of four AFM cantilevers head is shown in figure 2.5.

(1) The cantilever deflection detecting sensor should take less space and should be adjusted simply, so that the encoder head can be very compact,

(2) the area formed by four cantilever tips should be as small as possible due to the limited area of line-scale or grating as the reference,
(3) each cantilever is necessarily adjustable, because every cantilever tip needs to individually approach or retract the surface and to follow the tilt and topography of the grating which is used as the reference for encoding,
(4) each AFM cantilever should work in non-contact mode or intermittent contact mode in order that each cantilever can be used long-time without worn out quickly owing to the friction between cantilever tip and reference grating surface.

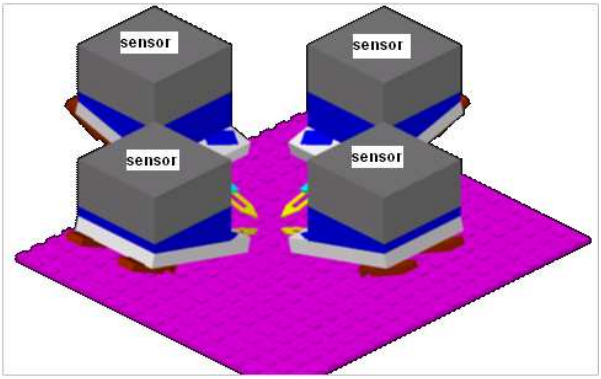

Figure 2.5 Mechanical schematic of four AFM cantilevers as encoder. Each cantilever has its own cantilever deflection detection sensor.

Most commercially available AFMs currently detect the cantilever deflection induced by surface forces with optical techniques. In the most common scheme, shown in Figure 2.6, a laser beam bounces off the back of the cantilever onto a position-sensitive photo detector (PSPD). As the cantilever bends, the position of the laser beam on the photo detector shifts. The PSPD itself can measure displacements of light as small as 10Å. The ratio of the path length between the cantilever and the detector to the length of the cantilever itself produces the amplification. As a result, the system can detect sub-angstrom vertical movement of the cantilever tip.

However, in optical deflection detection of AFM cantilever bending as shown in figure 2.6, large space is required for the installation of laser diode, a

PSPD and other optic components such as optical lens, optical reflectors and optical beam splitter etc.

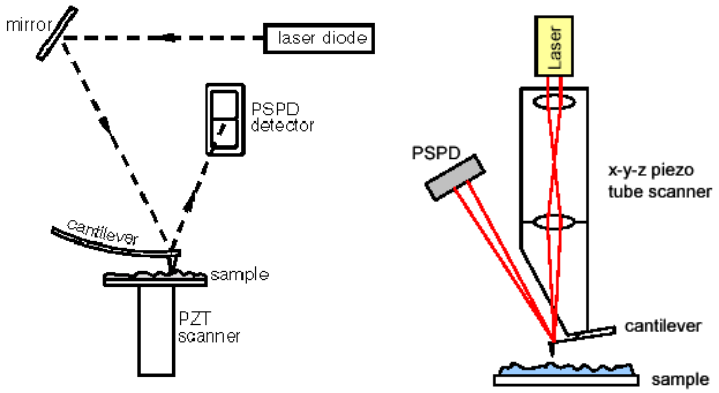

(a) (b)

Figure 2.6 Schematic of optical AFM cantilever deflection detection method [20]

One particularly technique is to fabricate the cantilever from piezoresistive material so that its deflection can be detected electrically [41]. In piezoresistive material, strain from mechanical deformation causes a change in the material's resistivity. For piezoresistive detection, a laser beam and a PSPD are not necessary. Nevertheless, available piezoresistive cantilever works in contact mode.

Considering all those issues addressed above, self-oscillating and self-sensing tuning-fork (TF) cantilevers [42] become the most favorite device as compared to its counterpart optical detection method because such method requires neither photo diode, nor laser diode, and it only requires a small volume of space above the scanning stage. The appearance of TF cantilever is shown in figure 2.7 (a). From the left to the right, it includes a ceramic plate with two gold-coated electrodes and three rectangular openings for the mechanical positioning, two quartz crystal prongs and a glued cantilever with tip which is zoomed in figure 2.7 (b). In operation, the electrical driving signal is directly applied to the electrodes of the ceramic plate to excite the two prongs of tuning fork at its resonant frequency. Two prongs are vibrating in-plane and have opposite phases, meaning that they approach and retract

from each other. Due to the twisting motion of the prongs, their opposite vibrations caused a small vibration at the ends of the glued cantilever in the direction perpendicular to the vibrations of prongs, which is the axis of the cantilever tip.

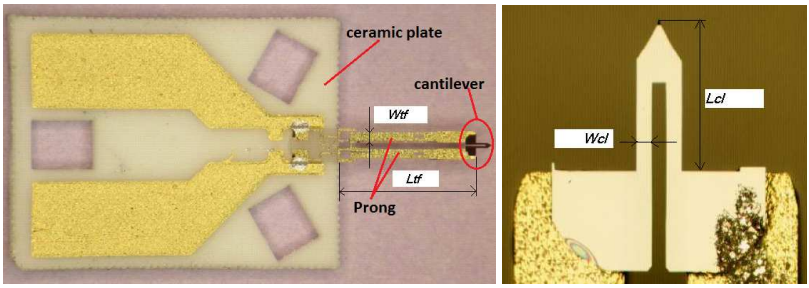

(a) (b)

Figure 2.7 TF cantilever is shown in (a) and cantilever is zoomed in (b) [42]

The dimensions of each part are listed together in table 2.1. Two prongs of tuning fork are long and narrow enough so that multi TF cantilever sensors are very likely to be integrated together as illustrated in figure 2.8.

Table 2.1 Dimensions of TF cantilever

	Length	Thickness	Width
Cantilever (μm)	*Lcl* = 310	*Tcl* = 3.7	*Wcl* = 30
Prong (μm)	*Ltf* = 2400	*Ttf* = 100	*Wtf* = 220
Ceramic plate (mm)	6.5	0.5	5.1

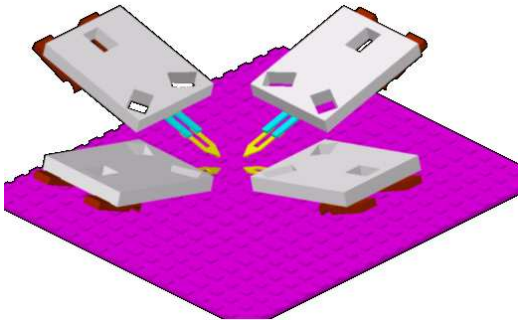

Figure 2.8 Simulation of four TF cantilevers are integrated into one encoder head.

2.5 Summary

In this chapter, mathematic models have been established for displacement decoding. When paired with 2D sinusoidal grating, four encoded signals or four AFM cantilevers are needed for displacement measurement in an arbitrary α direction. When paired with 1D sinusoidal grating, two AFM cantilevers are needed for the displacement measurement in *x*- or *y*-axis.

Since two or even four AFM cantilevers should be employed to make up an encoder for position decoding and displacement measurement, TF cantilever has been chosen for this purpose because of its compactness and the possibility to be integrated into one encoder head.

3 AFM with one TF cantilever

3.1 Working principle of TF cantilever

The mechanical structure of TF cantilever is shown in figure 3.1. The electrical driving signal is directly applied to the electrodes of the tuning fork to excite it at its resonant frequency, which is different from one to another, but usually between 40 and 50 kHz. In this design, the ends of the two prongs of a quartz tuning fork are vibrating in-plane with opposite phases, which means they approach and retract from each other. The in-plane vibration results in the out-of-plane vibration of the silicon cantilever and tip. The frequency and amplitude of TF cantilever are influenced by that of the tip vibration. The tip-sample interaction can cause a change of frequency and amplitude of the tip, which also affects the frequency of the tuning fork. The phase lock loop (PLL) detects the change and compensates this to keep the frequency constant. The schematic of tuning fork cantilever and its electronics is drawn in figure 3.2. Details can be found in reference [42].

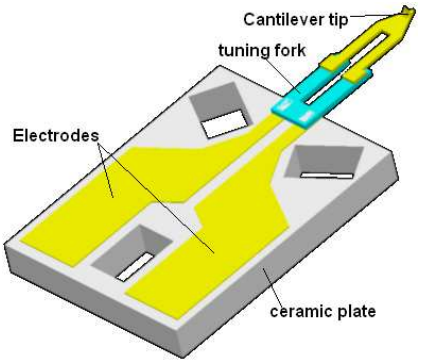

Figure 3.1 Mechanical structure of TF cantilever

According to the schematic illustrated in figure 3.2, a self-oscillation and PLL circuit and a preamplifier (I-V converter) circuit are developed. The design and layout of electronics are similar to that of Akiyama-probe (A-probe) technical guide [43]. The principle of self-oscillating and self-sensing will be discussed in the following subsections. The layout of electrical circuit of self-oscillating and self-sensing is attached in appendix B.

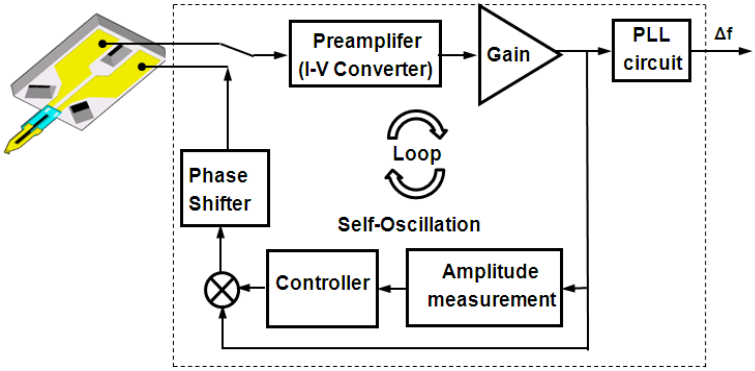

Figure 3.2 Schematic of TF cantilever and its electronics: self-oscillation and PLL circuit.

3.1.1 Preamplifier and self-oscillation circuits

Theoretically, the electrical properties of TF cantilever can be presented by an equivalent series circuit of a resistor R_{tf}, an inductor L_{tf} and a capacitor C_{tf} [44-46], which is shown in a part of figure 3.3 (a). If in the preamplifier circuit, the feedback resistor is R_f, the gains of preamplifier and automatic gain control (AGC) circuit are A and G respectively, when $R_{tf} = G \cdot R_f$, the equivalent series circuit of the tuning fork has a resonant frequency of $\omega_0 = 2\pi f_0 = 1/\sqrt{L_{tf} C_{tf}}$ [45].

To excite the tuning fork at its resonant frequency, self-oscillating signals are sinusoidal. The phase difference between signals coming out from preamplifier circuit and going to it is locked at 90° as shown in figure 3.4 (a). In this process, the amplitude-frequency property bears a resemblance of Lorentz-shaped curve, which is almost symmetrical to the resonance peak as shown in figure 3.4 (b). However a parasitic capacitance C_P around the TF cantilever can cause a parasitic frequency response so that the frequency response curves are no longer symmetric as shown in figure 3.4 (d), 3.4 (f) and 3.4 (h).The parasitic capacitor includes any parasitic capacitance from electrical contacts and connecting wires. In this case the driving signals going to and coming from preamplifier circuit are distorted, and the phase shift is larger than 90° as shown in figure 3.4 (c) and 3.4 (e) or locked at 180° and 0°

as shown in figure 3.4 (g). In addition, the self-oscillation frequency cannot be tuned to the resonant frequency of TF cantilever. To avoid this effect, a capacitance compensation circuit, as the same as that in reference [43], is integrated in the preamplifier circuit as shown in figure 3.3 (b), where the resistors in red can be replaced by the one with other resistances for this work in order to achieve a better signals like figure 3.4 (a). Because each TF cantilever has its own capacitance C_{tf}, for each new TF cantilever this capacitance has to be adjusted to a new value by using a variable electric resistor *VR* as a regulator in the capacitance compensation circuit.

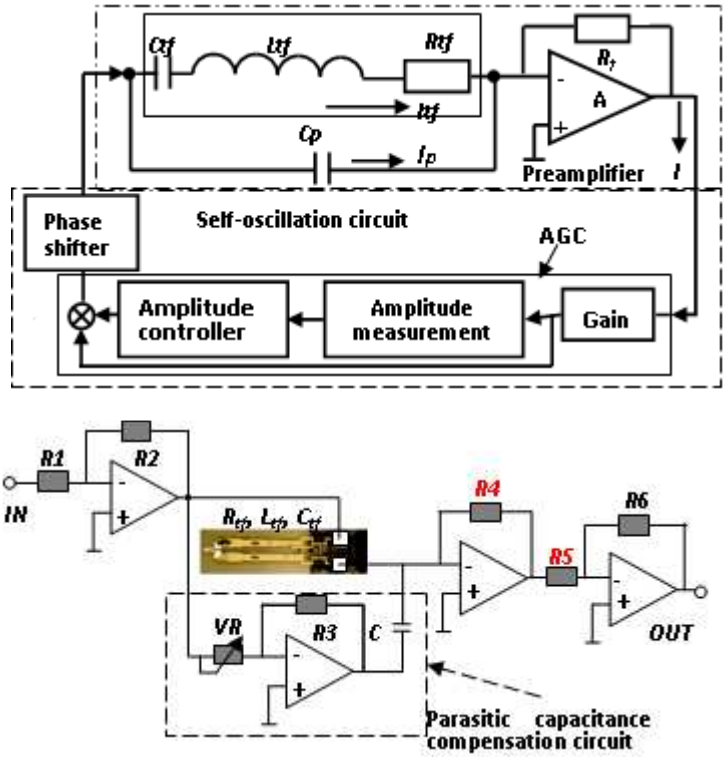

Figure 3.3 (a) is schematic of closed-loop control circuit of TF cantilever and (b) is preamplifier with parasitic capacitance compensation circuit from reference [43].

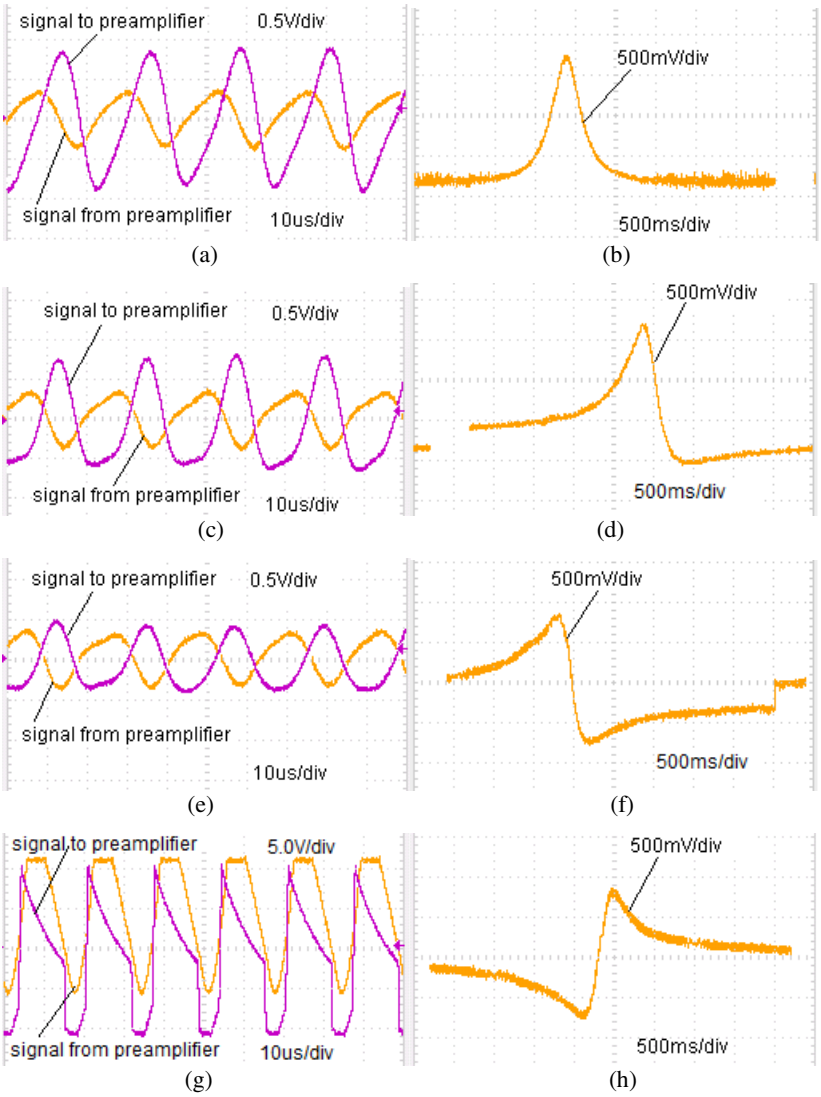

Figure 3.4 (a), (c), (e) and (g) are waveforms of input to and output from self-oscillation circuit; (b), (d), (f) and (h) are corresponding amplitude-frequency property curves with scale of 500ms/div or 100Hz/div.

The amplitude – frequency curves shown in figure 3.4 are plotted such:

(1) a sinusoidal signal with frequency sweep from a function generator is applied to the preamplifier input. The central frequency is the resonant frequency of TF cantilever, the frequency span is 1000 Hz and sweeping time is five seconds. The amplitude of sinusoidal signal may vary according to different cantilevers,

(2) the signal at the output from amplitude measurement model in self-oscillation circuit shown in figure 3.4 (b) appears on the oscilloscope, which depicts the enlarged amplitude – frequency curve of the signal coming from the preamplifier. The oscilloscope is set 500 ms/div, which is equal to 100 Hz/div.

According to reference [44], in figure 3.3 (a), if preamplifier gain is $A=R_f/R_{tf}$, self oscillation starts when

$$0 < G\frac{R_f}{R_{tf}} - 1 < \frac{2}{R_{tf}}\sqrt{\frac{L_{tf}}{C_{tf}}} \tag{3-1}$$

When self oscillation starting, its amplitude grows until the following condition is fulfilled:

$$G\frac{R_f}{R_{tf}} - 1 = 0 \tag{3-2}$$

Then the circuit oscillates at the resonant frequency of TF cantilever $f_O = 1/(2\pi\sqrt{L_{tf}C_{tf}})$.

3.1.2 PLL circuit

After the gain stage in self-oscillation circuit, the sinusoidal signal with the resonant frequency of a TF cantilever output from the preamplifier is fed to PLL circuit too. The output from the PLL in the design is a DC signal which gives a frequency difference between the input self-oscillation sinusoidal signal and the local voltage controlled oscillator (VOC) integrated inside the PLL IC chip (XR2212). The remaining AC components are eliminated by the low-pass filter at the final stage. Simple PLL circuit can also be referred in appendix B.

The properties and performance of TF cantilever need to be investigated by being integrated into an AFM mechanically and electrically. There is no commercially available or ready-made AFM which can do so. Therefore to design and develop an experimental device, a homebuilt AFM with one self-oscillating and self-sensing TF cantilever, is the priority. After that, TF cantilever will be tested in the designed and developed experimental device. All those will be discussed in the next section.

3.2 Homebuilt AFM with one TF cantilever

A homebuilt AFM using one self-oscillating and self-sensing TF cantilever, abbreviated to TF-AFM, is shown in figure 3.5 (a), figure 3.5 (b) is the zoomed photo of preamplifier board, TF cantilever and 1D grating.

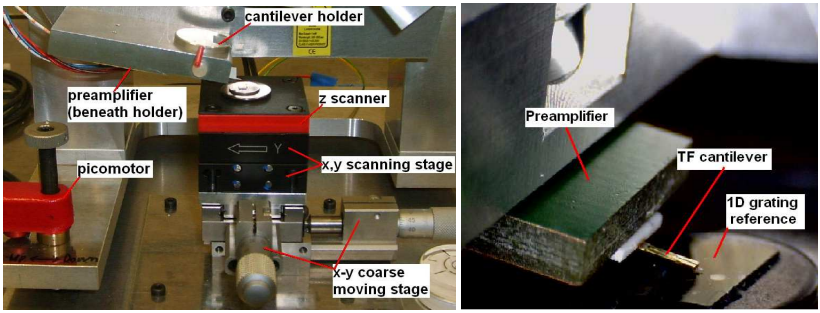

(a) (b)

Figure 3.5 (a) A homebuilt TF-AFM; (b) Zoomed TF cantilever and sample.

In figure 3.5 (a), a coarse moving stage electrically driven by a picomotor™ actuator is employed to make the cantilever tip approach and retract from the grating surface and a piezoelectric z scanner is adopted for the feedback control. For scanning, a 100 µm × 100 µm *x-y* piezoelectric scanning stage and its controller has been used (P-621.2 CD of Physik Instrumente GmbH). The *x-y* piezoelectric scanning stage can be used as micro displacement stage in open-loop mode as well as closed-loop mode, whereby the positions are controlled by its built-in capacitance sensors. A Newport M-461 *x-y* coarse moving stage is installed under the *x-y* piezoelectric scanning stage which is employed to coarsely move the sample position relative to the AFM cantilever beforehand. From figure 3.5 (b), it can be seen that the cantilever

holder together with preamplifier takes only a small volume of space. When multi TF cantilevers are mechanically integrated into one sensing head, actually it allows further reducing the volume of space above the holder and preamplifier because the preamplifier printed circuit board (PCB) is only 50 mm long, 15 mm wide and 5 mm thick.

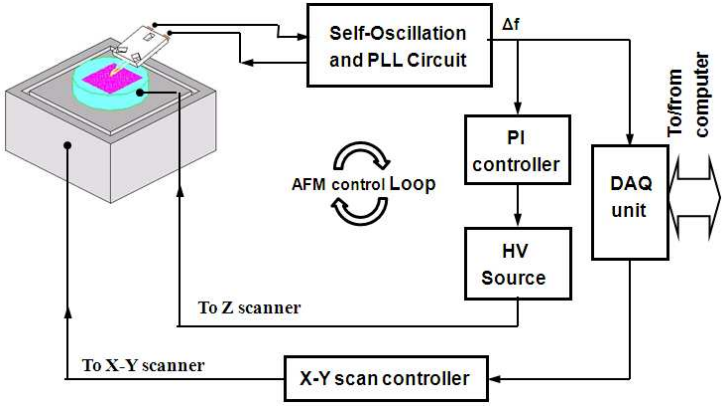

Figure 3.6 Schematic of self-oscillating and self-sensing TF-AFM.

The entire setup of TF-AFM is schematically illustrated in Figure 3.6. Unlike the conventional non-contact amplitude modulation (AM) mode of AFM which detects the change of amplitude with frequency shift, the TF-AFM works in the intermittent-contact frequency-modulation (FM) mode and oscillates at its resonant frequency f_0. In this test, the change of frequency is detected and measured as the cantilever tip approaches the measured sample surface as well as it retracts from it. The change of frequency is detected by a PLL circuit and converted to the DC voltage by it at the output port used for the AFM feedback control. Before approaching, a small DC offset voltage is preset, i.e. the surface is scanned at a constant frequency shift.

3.2.1 AFM controller

In figure 3.6, a PTB-homebuilt analogue proportional and integral (PI) controller and a PTB-homebuilt z-scan controller – high voltage (HV) source are called AFM controller in the following. Together with z scanner, self-

oscillation and PLL circuit as the driver and detector of TF cantilever, they constitute an AFM control loop. The TF cantilever picks up the signal from the measured surface and the signal is data-acquired by computer through a data acquisition (DAQ)-card (NI PCIe-6259).

3.3 Experiments and results

3.3.1 Noise level

With x-y scanner switched off and z scanner switched on, the cantilever is controlled to approach the sample by the picomotor^{TM} to such a position that z scanner HV source indicates zero volt voltage, and the effective amplitude (RMS) value of output voltage from HV source is recorded by acquiring 1000 points of data as one group. The typical noise graph is plotted in figure 3.7. The average RMS of 20 groups of data points is 14.82 mV (~1.5 nm) and 34.38 mV (~3.5 nm) when TF cantilever is oscillating in free space and in periodic contact with sample respectively.

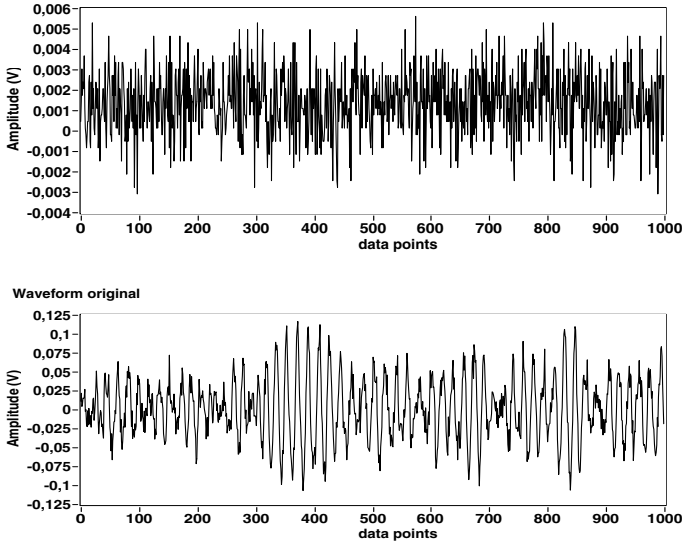

Figure 3.7 PLL noise when TF cantilever (a) in free space and (b) in periodic contact with sample.

3.3.2 Sensitivity of TF cantilever

Each TF cantilever has its own specifications: resonant frequency f_O, Q-factor, approximate capacitance (pF) and maximum frequency shift Δf_{max} etc which are the intrinsic characteristics for that cantilever. Δf_{max} and sensitivity can be calculated from approach curve. The sensitivity is defined as the maximum frequency shift divided by the amount of tip displacement in the periodic contact region. Nevertheless according to the reference [42], the maximum frequency shift Δf_{max} does not depend on the tip vibration amplitude, although the sensitivity differs for each setting of the tip vibration amplitude, which is increased as the tip vibration amplitude is decreased. Tip vibration amplitude can be manually adjusted before cantilever tip scans. Therefore each TF cantilever has its own sensitivity after stabilized sinusoidal self-oscillation signals with 90° phase shift have been gained. It is explained by the experiments on the following parameters.

3.3.2.1 Sensitivity of z piezoelectric scanner

When different voltages from HV source are applied to the z piezoelectric scanner, its sensitivity S_z is about 0.10 nm/mV or 100 nm/V depending on the different HV voltage applied. They are listed in table 3.1.

Table 3.1 measurement on sensitivity of z piezoelectric scanner

shift	Stroke (μm)	HV voltage (V)	Sensitivity S_Z (nm/mV)
1	9.0	±40.0	0.11
2	8.0	±36.5	0.11
3	7.0	±32.5	0.11
4	5.0	±25.5	0.10
5	4.0	±20.0	0.10
6	3.5	±19.5	0.09
7	2.5	±16.0	0.08
8	2.0	±12.5	0.08
average	---	---	0.10

3.3.2.2 Gains of PI controller and HV source

The AFM control loop in figure 3.6 is redrawn in figure 3.8 with schematic inside of PI controller. If the PLL output voltage $\delta(t)$ is input into the proportional part and the integral part of PI controller, the output voltage is $G_P \cdot \delta(t)$ (V) and $Gi \int \delta(t)dt$ (V) respectively, where G_P and Gi is the gain of the proportional part and the integral part respectively. The gain of PI controller is expressed as $G_P \cdot \delta(t) + Gi \int \delta(t)dt$ (V). It is continuously tuneable approximately from 0 to 8.

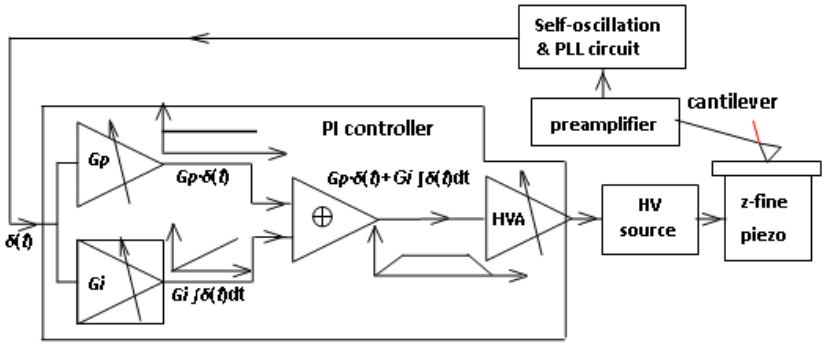

Figure 3.8 Schematic inside of PI controller and AFM control loop.

There are several gain shifts on the front panel of HV source; three of them are more often used. They are HV10, HV20 and HV40 which has voltage limit of 10 V, 20 V and 40 V and different gain respectively. When PI gain is set to its maximum, the gains of it and HV source at shift HV10, HV20 and HV40 are measured by voltmeter when the PLL voltage is tuned from 0 to 2 V. The measured data are drawn in graph shown in figure 3.9. Actually, when PLL voltage is set up to 1.5V, every shift of HV source has already come to its limit of 10 V, 20 V and 40 V respectively. The measured gains are listed in table 3.2, where 'gain' denotes individual gain of PI controller, HV10, HV 20 and HV 40, while 'combined gain' includes PI gain and HV source gain, which can be expressed as $K_i = k_i \times k_{PI}$ (i=10, 20 and 40 respectively).

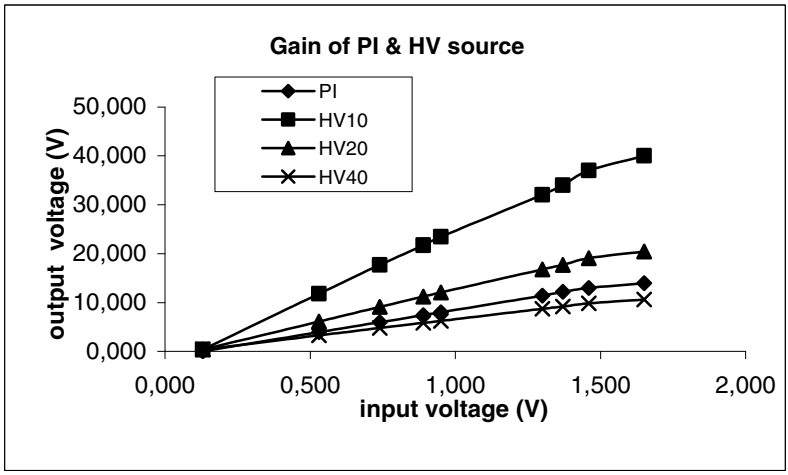

Figure 3.9 Gain measurement results of PI controller and shifts HV10, HV20 and HV 40 of HV source.

Table 3.2 Gain measurement results

Descriptions	PI	HV10	HV20	HV40
gain	$k_{PI} = 8.11$	$k_{10} = 0.72$	$k_{20} = 1.42$	$k_{40} = 2.77$
combined gain	----	$K_{10} = 6.58$	$K_{20} = 12.97$	$K_{40} = 25.2$

3.3.2.3 Approach curve and sensitivity of TF-AFM

The approach curve is tested according to the following procedure:

(1) set gain of HV source to HV40 shift ($k_{40} = 2.77$, see table 3.2), let TF-AFM work as usual as shown in figure 3.3, let cantilever tip approach the 1D grating surface to such a position that the PLL voltage is approximately 0 V and HV source voltage indicator displays "0" too, which means that z piezoelectric scanner neither extends nor contracts, and the distance between cantilever tip and sample is in the periodic contact region;

(2) disconnect the cable between PLL output and PI controller input, and connect oscilloscope to PLL output as shown in figure 3.10;

(3) set function generator to generate sinusoidal signal of 0.01 Hz in

frequency, -0.4 V in low level amplitude and +2 V in high level amplitude, so that amplitude of voltage is Vpp=2.4 V. The sinusoidal signal is input into HV source. Then it is amplified to control the z piezoelectric scanner to extend and contract periodically in 0.01Hz frequency.

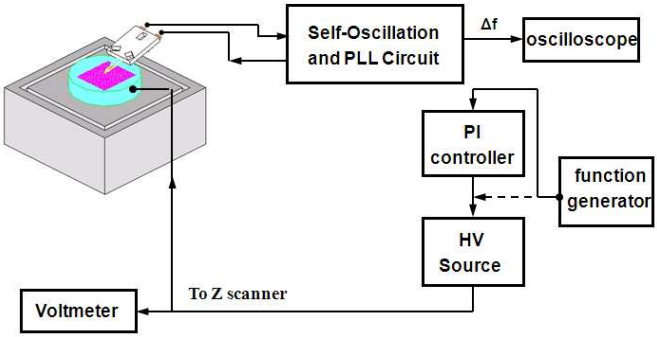

Figure 3.10 Schematic of experiment on approach curve of TF-AFM.

The PLL voltage changes from high level V_{PLLH} to low level V_{PLLL} and corresponding cantilever frequency changes from low frequency f_L to high frequency f_H. If the low level amplitude and high level amplitude of the sinusoidal signal from function generator input into HV source is set further lower and higher respectively, it is found V_{PLLH}, V_{PLLL}, f_L and f_H do not change anymore, which means TF cantilever frequency shift has already come to its maximum beforehand. Therefore from contraction to extension, the effective voltage V_{HVeff} applied to z-piezoelectric scanner which contributes to the maximum frequency shift of TF cantilever is calculated by multiplying not the total voltage V_{PP} but influential voltage $V_{PP\text{inf}}$ input into HV source with gain k_{40} of HV source, which is

$$V_{HVeff} = V_{PP\text{inf}} \times k_{40} \tag{3-3}$$

$V_{PP\text{inf}}$ can be derived from approach curve. Since it has been already known that the sensitivity of z-piezoelectric scanner is 100 nm/V, the effective stroke L_{eff} of the z-piezoelectric scanner should be

$$L_{eff} = V_{HVeff} \times 100 \text{ (nm)} \tag{3-4}$$

Thus, the sensitivity of TF cantilever can be calculated as

$$S_{TF} = (f_H - f_L) / L_{eff} \text{ (Hz/nm)} \tag{3-5}$$

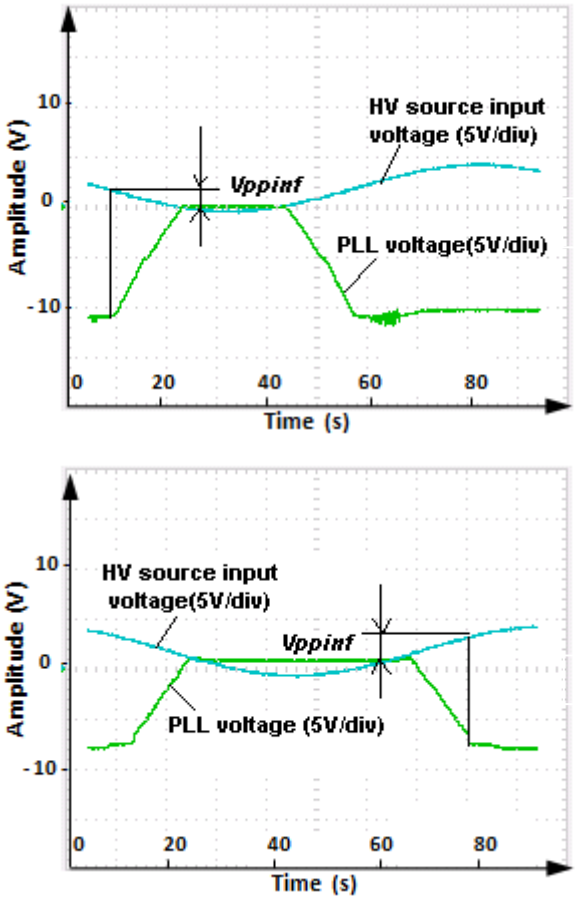

Figure 3.11 Approach curve tests to any two cantilevers with (a) low Q-factor and large Δf while (b) high Q-factor and small Δf.

The approach curves of AFM with two typical TF cantilevers are shown in figure 3.11 (a) and 3.11 (b). Figure 3.11 (a) is the approach curve of a TF cantilever with resonant frequency fo=40.179 kHz, maximum frequency shift Δf =398 Hz and 614 low Q-factor while figure 3.11 (b) is the approach curve of a TF cantilever with resonant frequency fo =42.557 kHz, maximum frequency shift Δf =123 Hz and 1487 high Q-factor. The related data directly

measured or derived by using equations (3-3) ~ (3-5) are listed in table 3.3. From the data, it can be seen that the cantilever with low Q-factor and large frequency shift is more sensitive than that with high Q-factor and small frequency shift.

Table 3.3 Cantilever sensitivity experiment results

	PLL voltage (V)		Frequency (kHz)		V_{PPinf}	V_{HVeff}	L_{eff}	Sensitivity
	V_{PLLH}	V_{PLLL}	Low f_L	High f_H	(V)	(V)	(nm)	S_{TF} (Hz/nm)
(a)	0	-10.6	40.1477	40.5324	2	5.54	554	0.69
(b)	0.9	-7.8	42.5231	42.6591	3	8.31	831	0.16

3.3.3 Experiments on the optimum scanning parameters

Scanning parameters include set-point, offset PLL voltage, the gain of PI controller and the stroke of z-scanner etc. The experiments are conducted.

3.3.3.1 Set-point and PLL voltage offset

In scanning, set-point is the voltage V_{set} which is maintained by AFM control loop in such a way that TF cantilever oscillates at a given amplitude and constant frequency shift. HV source is a floating but not ground voltage source, which means that it outputs positive or negative control voltage of equal amplitude to drive z piezoelectric scanner. Positive voltage extends z piezoelectric scanner and negative voltage contracts it. Therefore zero voltage (V_{set}=0 V) is chosen as the best set-point. PLL voltage offset V_{offset} determines the offset of frequency f which differs from resonant frequency f_O of cantilever at free space as illustrated in amplitude-frequency curve in figure 3.12. If V_{offset} is set too high, Δf becomes larger and the tip vibration amplitude is smaller when the tip comes to the set-point. Usually Δf is chosen in the range of 10 Hz ~20 Hz, which means V_{offset} is about 0.5 V ~1 V.

As charted in the schematic approach/retraction curve shown in figure 3.13, far away from the surface the cantilever oscillating in free space at its resonant frequency f_0; when it passes over the critical point A, the tip is coming in the region of periodic contact with sample and V_{offset} becomes smaller; From point A to point B the frequency increases and when it comes

a point in the range between A and B and V_{offset} drops to zero, it reaches set-point if V_{set}=0. If the cantilever tip is pushed further to approach critical point B, it jumps into contact with sample. V_{offset} may drop to the negative bottom line, which is -10 V for the homebuilt TF-AFM described in this paper. The further from B the cantilever tip is, the less negative (or more positive) the set-point voltage and PLL voltage become; the closer to B the cantilever tip is, the more negative (or less positive) the set-point voltage and PLL voltage become.

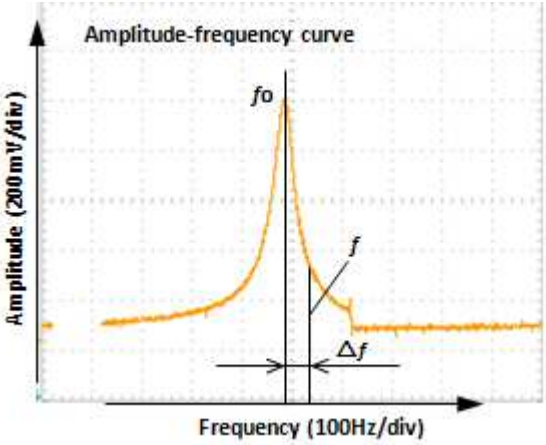

Figure 3.12 Amplitude–frequency curve.

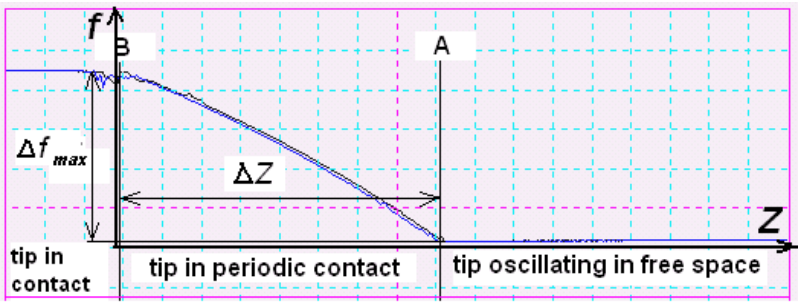

Figure 3.13 Schematic of approach and retraction curve.

However, from the topographies of 1D rectangular grating of 80 nm in pitch and 1D sinusoidal grating of 300 nm in pitch scanned by the TF-AFM at

different set-points shown in figure 3.14 there are no apparent differences if set-points are different.

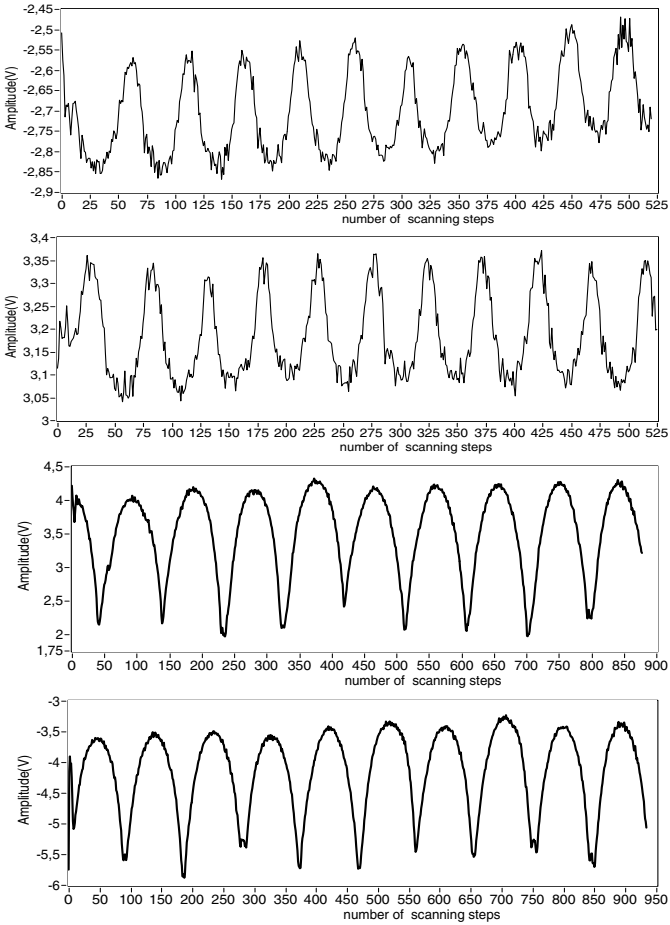

Figure 3.14 Topographies scanned at different set-point: (a) and (b) are that of 1D rectangular grating of 80 nm in pitch, (c) and (d) are that of 1D sinusoidal grating of 300 nm in pitch.

3.3.3.2 Gains of PI controller and strokes of *z*-scanner

In figure 3.8, the integral part of PI controller actually is a phase-reversing integrator with (as shown in figure 3.15), and its gain G_i is

$$G_i = \frac{1}{RC} \tag{3-6}$$

where, $\tau = RC$ is the integral time constant.

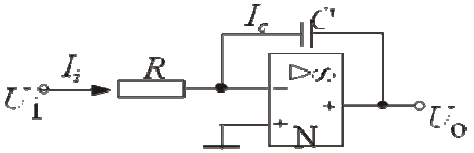

Figure 3.15 Schematic of phase-reversing integrator

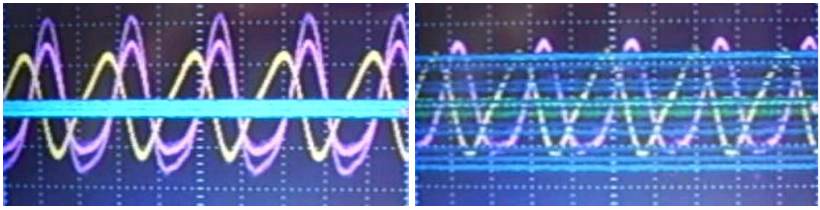

(a) (b)

Figure 3.16 Self-oscillation of PI output DC voltage: slight in (a) and severe in (b).

Usually the larger the integration gain G_i is set, the more sensitive the feedback loop is, and the better the tip scans along the sample surface. However, if the integral gain is set too large, on the oscilloscope there appears self-oscillating effect for the DC voltage output from PI controller in the AFM control loop as shown by the blue-colored signal in figure 3.16, where the two sinusoidal signals with approximate 90° phase shift on the background are the driving signals coming out and going in the TF cantilever preamplifier. The phenomenon would result in higher noise in the 1D grating position-encoded signal.

In figure 3.17 and figure 3.18, several surface topographies of 1D sinusoidal grating of 300 nm in pitch and 80nm amplitude obtained by TF-AFM are exhibited. Using different capacitances in figure 3.15 (e.g. C = 0.22 μF and 0.33 μF) and setting different z-scanner stroke (±5 μm in figure 3.17 and ±2 μm in figure 3.18), the noise level decreases from figure (a) to (b). In the figures, data points (number), the title of *x*-axis, means that one data point corresponds to one step of displacement of *x*-axis scanning stage. Thus the scanned surface topographies become smooth and clear by using a capacitance of 0.33 μF and setting the z-scanner stroke to ±1 μm for 1D sinusoidal grating of 300nm in pitch as shown in figure 3.19.

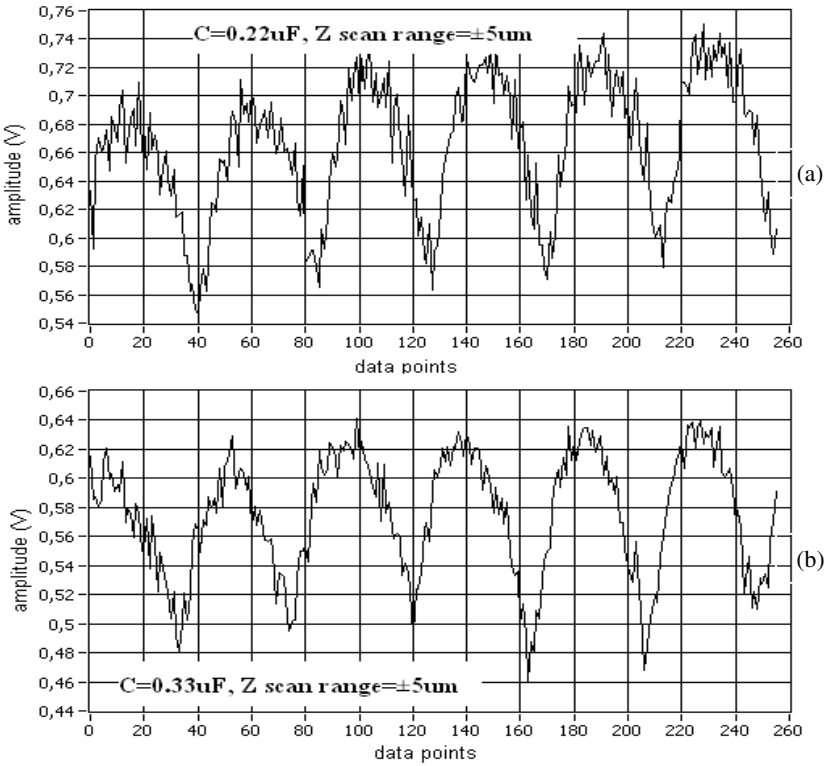

Figure 3.17 Topographies of 1D sinusoidal grating of 300 nm in pitch with z scan range of ±5 μm and capacitances of 0.22 μF in (a), 0.33 μF in (b).

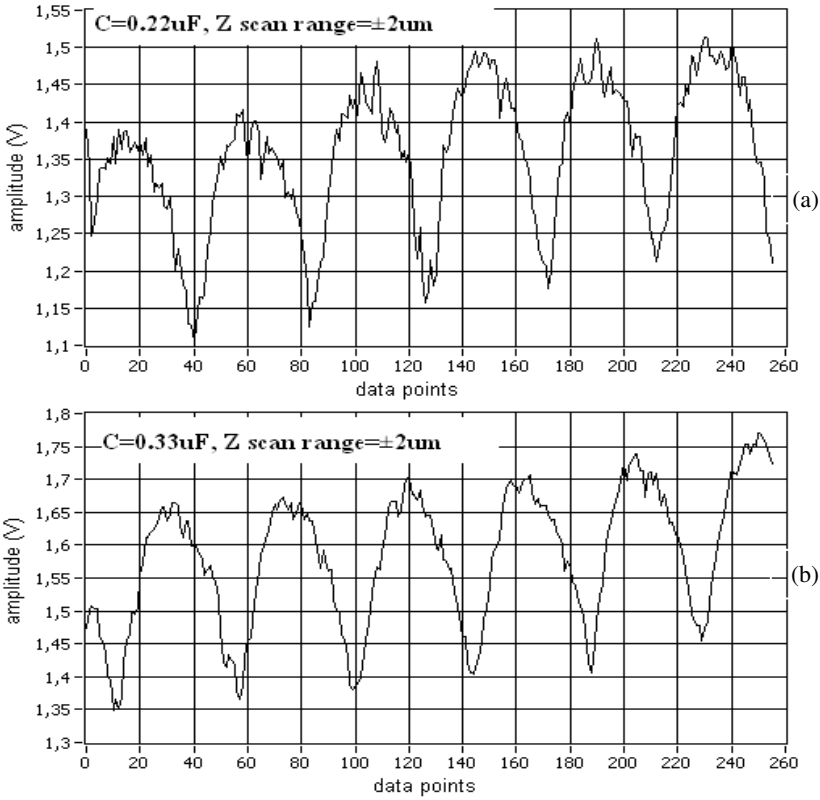

Figure 3.18 Topographies of 1D sinusoidal grating of 300 nm in pitch with z scan range of ±2 μm and capacitances of 0.22 μF in (a), 0.33 μF in (b).

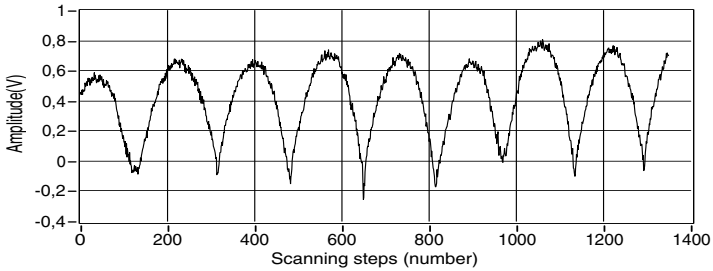

Figure 3.19 Topographies of 1D sinusoidal grating of 300 nm in pitch with z scan range of ±1 µm and capacitance of 0.33 µF.

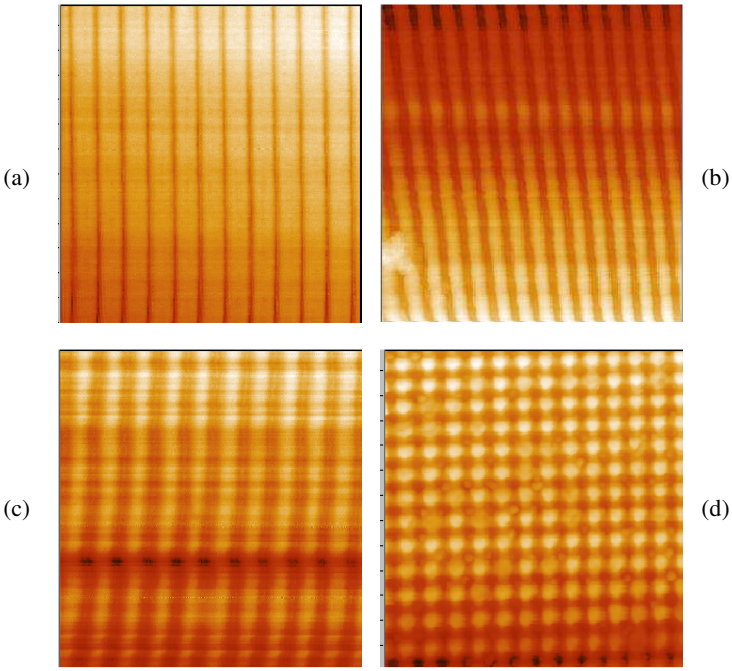

Figure 3.20 Images scanned by TF-AFM, where (a) rectangular grating of 200 nm in pitch (4 µm × 4 µm), (b) Motex grating of 300nm in pitch (5 µm × 5 µm), (c) home-fabricated grating of 80 nm in pitch (1 µm × 1 µm) and (d) NPL 2D grating of 300nm pitch (5 µm × 5 µm)

3.4 AFM performance based on image scanning

Clear and high-quality images can be obtained as shown in figure 3.20, when

(1) TF-AFM set-point is properly chosen by adjusting the output voltage of PLL according to the TF cantilever approaching curve or direct according to its frequency shift Δf written on the data sheet of products (see subsection 3.3.3.1),
(2) the parameters of the PI controller are selected properly after the experiment (see subsection 3.3.3.2),
(3) the stroke of z scanner is set properly based on the topography of measured sample (see subsection 3.3.3.2).

3.5 Summary

The performance of TF cantilever is investigated and tested in the homebuilt experimental setup: a self-oscillating and self-sensing TF-AFM.

The entire setup for the TF-AFM has been described schematically. Unlike the conventional non-contact AM mode of the AFM which detects the change of amplitude, the principle of TF-AFM is based on FM mode; the TF cantilever is driven at the resonant frequency f_0 and operated at constant frequency shift during scanning. The change in frequency is detected and measured during the cantilever tip is approached to and retracted from the measured surface. The change in frequency which is converted by a PLL to DC voltage at the output port is used for the feedback control.

4 One TF cantilever as an encoder based on TF-AFM for real-time displacement measurement

4.1 Decoding principle - direct decoding

When a 1D grating is probed by one AFM cantilever as an encoder along a known displacement direction (forward or backward) perpendicular to the lines of grating, recorded signal usually consists of many countable integer waveforms. Displacements can be calculated from the integer number and two fractional parts of a waveform at the beginning and at the actual position of the displacement. A part of 1D sinusoidal grating position-encoded signal scanned by a TF cantilever shown in figure 4.1 is an example. One waveform corresponds to one period of the1D grating. Therefore one directional (forward or backward) displacement of the micro-scanning stage can be measured by the count of integer number of periods and calculation of the fractional parts from the starting point to the real-time position, in between the integer period is numbered as *I* and fractional parts of a period is calculated as *fs* at the beginning and *fe* at the actual or end position. If the pitch of 1D grating is known as *P* (unit: μm or nm), and the displacement *S* will be:

$$S = (fs + I + fe) \cdot P \tag{4-1}$$

Here it is assumed that the alignment of the grating sample is coplanar to the scanning direction, i.e. the tilt of the sample is small and the alignment of the direction of the grating lines is perpendicular to the direction of displacement.

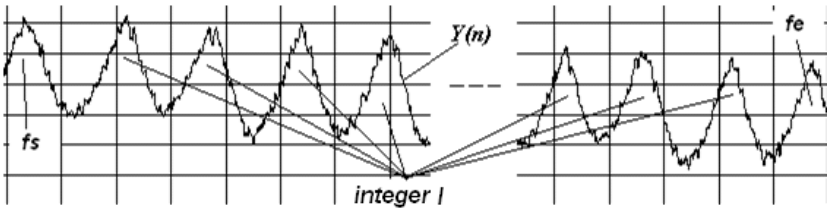

Figure 4.1 The 1D sinusoidal grating position-encoded signal *Y*(*n*) probed by one TF cantilever. It consists of integer waveforms *I* and fractional parts *fs* at the beginning and *fe* at the actual or end position.

4.2 Real-time filtering of 1D grating position-encoded signal

Besides 1D sinusoidal grating, 1D rectangular grating and 1D triangular grating etc can also be used to be paired with one AFM cantilever to measure displacement of scanning stage beneath them based on counting integer periods and calculating the fractional parts of a period from grating position-encoded signal in real time. However, real-time signal processing and real-time displacement measurement result displaying are very necessary.

No matter the grating position-encoded signal is sinusoidal, rectangular or other waveforms, the signal should have as less noise as possible. However, the normal encoded signal is always accompanied more or less by the noise. This will result in wrong or incorrect counting of integer periods as well as calculating the fractional parts of a period. Therefore it is very important to apply a filtering technique to filter the signal and to obtain a good signal-to-noise ratio (SNR). The technique should be able to filter the signal in real time, and the filtered signal should have no change of the period. For this purpose, study concerning the real-time filtering of 1D grating position-encoded signal have to be conducted prior to and during the research of real time displacement measurement by using AFM cantilevers as encoder .

In the following sections a real-time filtering technique in theory and practice is described. At first, a 1D sinusoidal grating position-encoded signal is taken as an example, and the principle of real-time filter will be mathematically explained. Afterwards the real-time filter will be used for filtering of 1D sinusoidal grating, 1D rectangular grating and 1D triangular grating position-encoded simulation signals. Last the real-time filter will be applied in the experimental displacement measurements for the signal encoded from 1D sinusoidal grating and 1D rectangular grating when they are scanned by an AFM cantilever.

4.2.1 Mathematical expression of 1D sinusoidal grating position-encoded signal

Let us assume that $Y(n)$ represents 1D sinusoidal grating position-encoded signal probed by an AFM cantilever in figure 4.1. It can be resolved into a sinusoidal signal $Z(n)$ without noise, a white noise $W(n)$ and a low frequency tilt signal $U(n)$, which is

$$Y(n) = Z(n) + U(n) + W(n) \tag{4-2}$$

Where $Y(n)$, $Z(n)$, $U(n)$ and $W(n)$ are all finite discrete sequences with number M of data points at a given time, and

$$Z(n) = A\sin(\frac{2\pi}{p}n), \quad 0 \le n < M-1 \tag{4-3}$$

$$W(n) = \frac{1}{M} \qquad 0 \le n < M-1 \tag{4-4}$$

Where p (data points) denotes the period of 1D sinusoidal grating position-encoded signal $Y(n)$.

$U(n)$ may be caused by the scanning stage or a tilted 1D grating. It can be expressed as a polynomial function

$$U(n) = H_0 + H_1 \cdot n + \cdots + H_K \cdot n^K, \qquad 0 \le n < M-1 \tag{4-5}$$

where, H_0, H_1, ···, H_K are the constant item, coefficient of monomial item, coefficient of quadratic item, ···, and coefficient of K^{th} order item respectively.

4.2.2 Real-time filtering to 1D sinusoidal grating position-encoded signal - mathematics

The signal detected by an AFM cantilever can be improved if the parameters of controller or electronics unit of the cantilever are properly optimized. Taking a TF cantilever as an example, clear and high quality signal can be obtained when

1. a new tip is installed,
2. the TF-cantilever set-point is properly chosen by adjusting the output voltage of PLL according to the pre-tested AFM cantilever approaching curve,
3. the proportional gain and integral gain of PI controller are selected properly, and

4. the stroke of Z scanner has been set properly on the basis of topography of measured specimen.

To reduce the remaining noise some digital filters such a Butterworth, Chebyshev, Bessel and FIR etc have been tried for point by point data filtering or array based data filtering, but the effect is unsatisfied because the filtered waveform remains not smooth enough due to the existence of rough and bumpy anywhere at the terrains of peaks, slops and valleys. Figure 4.2 demonstrates the waveforms after point by point filtering or array based filtering the simulated 1D sinusoidal grating position-encoded signal (a) of 1 arbitrary unit in amplitude with white noise of 0.2 arbitrary units in amplitude by using Butterworth low-pass filter.

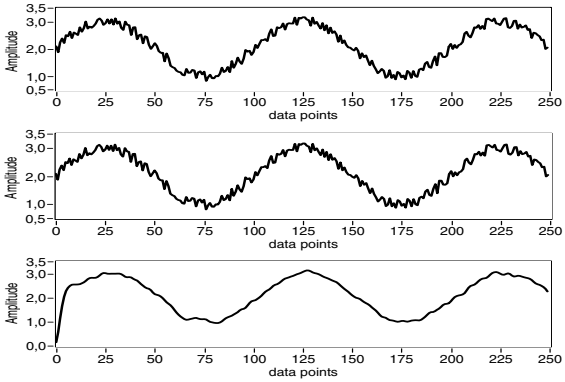

Figure 4.2 (a) Simulated sinusoidal grating encoded signal; (b) waveform point by point real-time filtering; (c) waveform after array based filtering.

In the signal processing, cross-correlation is a measurement of similarity of two structures, in telecommunication, a matched filter is named based on correlating a known signal or template with an unknown signal [47]. It also has applications in digital image processing such as pattern recognition etc, especially the application in single particle analysis and electron tomography averaging [48]. Recently correlation technique has been used for real-time oscilloscope triggering for complex waveforms [49].

For discrete finite sequences $f(n)$ and $g(n)$, the cross-correlation $R_{fg}(m)$ is defined as**:**

$$R_{fg}(m)=\frac{1}{N}\sum_{n=0}^{N-1}f(n)\cdot g(n+m) \tag{4-6}$$

where $m=-(N-1),-(N-2),\cdots,-1,\ 0,\ 1,\cdots,M-2,M-1$, which means in cross-correlation sequence total number is $(M+N)$, N is the number of elements in the sequence of f (n), M is the number of elements in the sequence of g (n).

Encoded signal $Z(n)$, probed by an AFM cantilever has been defined by equation (4-2). If a finite discrete sequence of sinusoidal template T (n) has N number of samples in the sequence and p_T numbers of samples in each period, which is

$$T(n)=B\sin(\frac{2\pi}{p_T}n),\quad 0\le n<N-1 \tag{4-7}$$

The cross-correlation of Z (n) and T (n) should be

$$R_{TY}(m)=R_{TZ}(m)+R_{TU}(m)+R_{TW}(m) \tag{4-8}$$

$R_{TY}(m)$, $R_{TX}(m)$, $R_{TU}(m)$ and $R_{TW}(m)$ are the cross-correlation filtered signal, cross-correlation sinusoidal signal, cross-correlation tilt signal and cross-correlation noise respectively.

Under some circumstances, for example, there is no correlation between $T(n)$ and $W(n)$, $R_{TW}(m)\approx 0$ and $R_{TY}(m)\approx R_{TZ}(m)+R_{TU}(m)$ in equation (4-8). If $R_{TU}(m)$ still is a low frequency tilt drift signal, it cannot modulate the period of $R_{Tz}(m)$, thus it has no influence to integer periods counting and fractional parts calculating. Therefore $Z(n)$ can be picked out or $W(n)$ can be filtered out from $Y(n)$ by calculating the cross correlation between $T(n)$ and $Y(n)$. $R_{TU}(m)$ and $R_{TZ}(m)$ are mathematically derived as follows.

$$\begin{aligned} R_{TU}(m) &= \frac{B}{N}\sum_{n=0}^{N-1}\{\sin(\frac{2\pi}{p_T}n)\cdot[H_0 + H_1\cdot(n+m)+\cdots+H_K\cdot(n+m)^K]\} \\ &= \frac{B}{N}\{\sum_{n=0}^{N-1}\sin(\frac{2\pi}{p_T}n)\cdot H_0 + \sum_{n=0}^{N-1}\sin(\frac{2\pi}{p_T}n)\cdot[H_1\cdot(n+m)]+\cdots+ \\ &\sum_{n=0}^{N-1}\sin(\frac{2\pi}{p_T}n)\cdot[H_K\cdot(n+m)^K]\} \end{aligned} \tag{4-9}$$

According to binominal theorem, in equation (4-9) the coefficient of each item can be expressed as J_j^i $(i,\ j=0,\ 1,\ 2,\ \cdots,\ K)$, which is

$$\begin{cases} \dfrac{B}{N}\displaystyle\sum_{n=0}^{N-1}\sin(\frac{2\pi}{p_T}n)\cdot H_0 = J_0^0 \\ \dfrac{B}{N}\displaystyle\sum_{n=0}^{N-1}\sin(\frac{2\pi}{p_T}n)\cdot[H_1\cdot(n+m)] = J_1^0 + J_1^1\cdot m \\ \cdots \\ \dfrac{B}{N}\displaystyle\sum_{n=0}^{N-1}\sin(\frac{2\pi}{p_T}n)\cdot[H_K\cdot(n+m)^K] = J_K^0 + J_K^1\cdot m + J_K^2\cdot m^2 + \cdots + J_K^K\cdot m^K \end{cases} \tag{4-10}$$

Where

$$\begin{cases} J_1^0 = \dfrac{B}{N}\displaystyle\sum_{n=0}^{N-1}[\sin(\frac{2\pi}{p_T}n)\cdot H_1\cdot n] \\ J_1^1 = \dfrac{B}{N}\displaystyle\sum_{n=0}^{N-1}[\sin(\frac{2\pi}{p_T}n)\cdot H_1] \\ \cdots \\ J_K^0 = \dfrac{B}{N}\displaystyle\sum_{n=0}^{N-1}[\sin(\frac{2\pi}{p_T}n)\cdot H_K\cdot n^K] \\ \cdots \\ J_K^K = \dfrac{B}{N}\displaystyle\sum_{n=0}^{N-1}[\sin(\frac{2\pi}{p_T}n)\cdot H_K] \end{cases} \tag{4-11}$$

If all the items in equation (4-11) are put back into equation (4-9), and coefficients in similar items are combined, equation (4-9) will become

$$R_{TU}(m) = L_K^0 + L_K^1\cdot m + L_K^2\cdot m^2 + \cdots + L_K^K\cdot m^K \tag{4-12}$$

where, L_K^0, L_K^1, L_K^2,$\cdots$,L_K^K are the constant item, coefficient of monomial item, coefficient of quadratic item, ···, and coefficient of K^{th} order item respectively.

where
$$\begin{cases} L_K^0 = J_0^0 + J_1^0 + J_2^0 + J_3^0 \cdots + J_K^0 \\ L_K^1 = J_1^1 + J_2^1 + J_3^1 + \cdots + J_K^1 \\ L_K^1 = J_2^2 + J_3^2 + \cdots + J_K^2 \\ \cdots \\ L_K^{K-1} = J_{K-1}^{K-1} + J_K^{K-1} \\ L_K^K = J_K^K \end{cases} \tag{4-13}$$

From equation (4-12), it can be seen that $R_{TU}(m)$ remains a low frequency tilt signal. It has no influence on or modulation to the period of $R_{TY}(m)$. As the systematic error, its influence to the accuracy of displacement and grating pitch measurement can easily be dealt with. Here suppose that it has been eliminated from *Y(n)*. Therefore

$$R_{TY}(m) \approx R_{TZ}(m) = \frac{AB}{N}\sum_{n=0}^{N-1} T(n)\cdot Z(n+m) \tag{4-14}$$
$$= \frac{AB}{N}\sum_{n=0}^{N-1} \sin(\frac{2\pi}{p_T}n)\cdot\sin[\frac{2\pi}{p}(n+m)]$$

The correlation equation (4-14) can be factorized as follows:

$$R_{TY}(m) = \frac{AB}{N}\sum_{n=0}^{N-1}[\sin(\frac{2\pi}{p_T}n)\cdot\sin(\frac{2\pi}{p}n)\cdot\cos(\frac{2\pi}{p}m)] + \tag{4-15}$$
$$\frac{AB}{N}\sum_{n=0}^{N-1}[\sin(\frac{2\pi}{p_T}n)\cdot\cos(\frac{2\pi}{p}n)\cdot\sin(\frac{2\pi}{p}m)]$$

To set
$$C_1[N, p_T] = \frac{AB}{N}\sum_{n=0}^{N-1}[\sin(\frac{2\pi}{p_T}n)\cdot\sin(\frac{2\pi}{p}n)] \tag{4-16}$$

$$C_2[N, p_T] = \frac{AB}{N}\sum_{n=0}^{N-1}[\sin(\frac{2\pi}{p_T}n)\cdot\cos(\frac{2\pi}{p}n)] \tag{4-17}$$

The equation (4-15) will become

$$R_{TY}(m) = C_1[N, p_T]\cdot\cos(\frac{2\pi}{p}m) + C_2[N, p_T]\cdot\sin(\frac{2\pi}{p}m) \tag{4-18}$$
$$= C[N, p_T]\cdot\sin(\frac{2\pi}{p}m + \phi)$$

where $C[N, p_T] = (C_1^2[N, p_T] + C_2^2[N, p_T])^{1/2}$, and
$\phi[N, p_T] = \tan^{-1}[C_2[N, p_T]/C_1[N, p_T]]$.

From equation (4-18), it can be concluded that $R_{TY}(m)$ remains sinusoidal signal sequence. It has the same period p as Z (n) although the amplitude has changed to $C[N, p_T]$ and the phase has a shift of $\phi[N, p_T]$.

The conclusion can be proved also by their frequency power spectra (FPS). The spectra of simulated 1D sinusoidal grating encoded signal of 1 arbitrary unit in amplitude without noise before and after cross-correlation filtering are plotted in figure 4.3 (a) and 4.3 (b), and with white noise of 0.5 arbitrary units in amplitude before and after cross-correlation filtering are plotted in figure 4.3 (c) and 4.3 (d), respectively. Apparently the spectra are almost in the same profiles before and after cross-correlation filtering.

Therefore, instead of directly counting the integer periods and calculating fractional parts from original encoded signal $Y(n)$, the cross-correlation signal $R_{TY}(m)$ seems to be quite reasonable to be used to count integer number of periods and to calculate fractional parts for the determination of the displacement. It is nearly free of noise if $R_{TW}(m) \approx 0$. This is discussed in the next section.

4.2.3 Optimum parameter of cross-correlation template

From equation (4-16) and (4-17), it can be seen that the template amplitude B only influences the amplitude but not the period p in $R_{TY}(m)$.

It is obvious from equation (4-18) that the change of template period p_T will also influence the amplitude of $R_{TY}(m)$. The influence will be discussed by simulation with programming in LabVIEW. The signal $Y(n)$ is generated by mixing the sinusoidal signal $Z(n)$ of 1 arbitrary unit in amplitude and 25 data points in period without noise and with white noise $W(n)$ of 0.5 arbitrary units in amplitude and 256 data points plotted in solid thin line as shown in figure 4.4. Taking it as an example, effective amplitude (RMS) of $R_{TY}(m)$, RMS of $R_{TW}(m)$ and the signal to noise ratio (SNR) are calculated respectively from it.

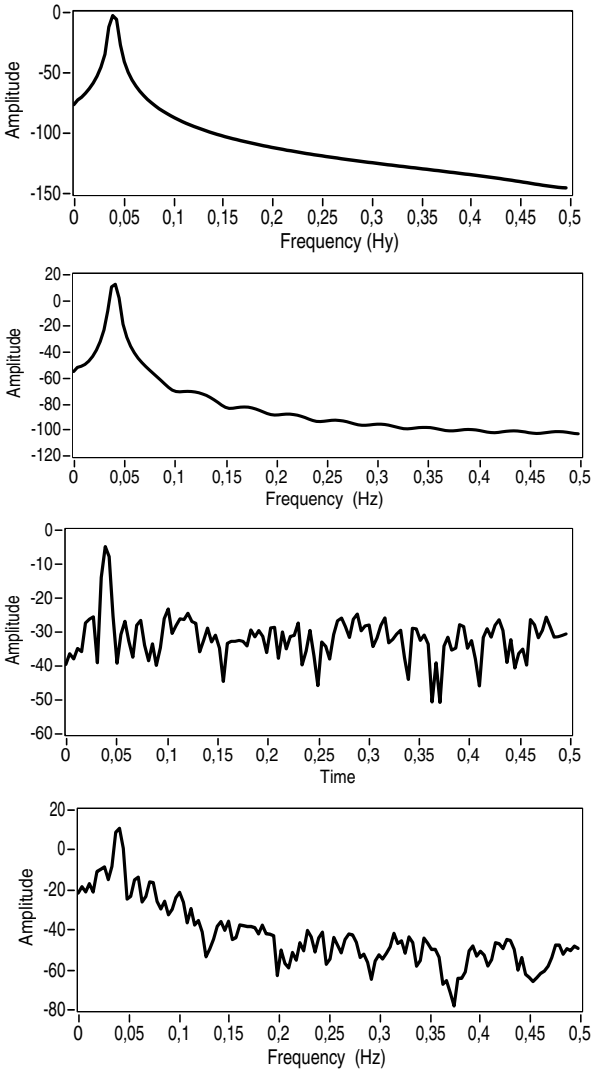

Figure 4.3 (a) and (c) are the spectra of sinusoidal signal without and with noise of 0.5 arbitrary units; (b) and (d) are the spectra of cross-correlation signals filtered from (a) and (c) respectively

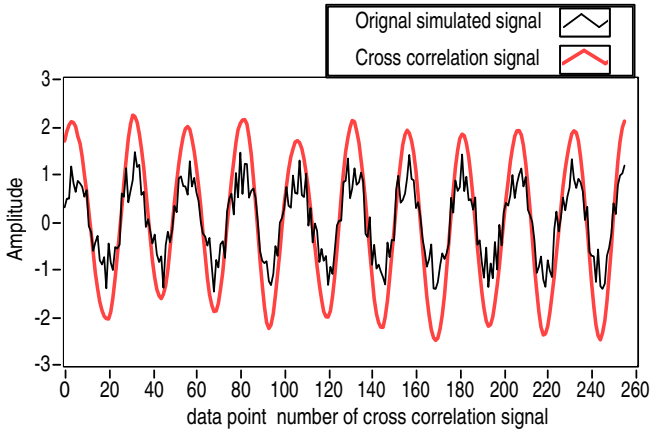

Figure 4.4 Simulation of 1D sinusoidal grating position-encoded signal of 1 arbitrary unit in amplitude and 25 points in period with white noise of 0 and 0.5 arbitrary units in amplitude in (a) and (b) respectively.

If mathematical expectations or means of $R_{TY}(m)$ and $R_{TW}(m)$ is μ_{TY} and μ_{TW} respectively, which can be calculated by

$$\begin{cases} \mu_{TY} = \dfrac{1}{M}\sum_{m=0}^{M-1} R_{TY}(m) \\ \mu_{TW} = \dfrac{1}{M}\sum_{m=0}^{M-1} R_{TW}(m) \end{cases} \tag{4-19}$$

RMS is calculated by

$$\begin{cases} \sqrt{A_{TY}} = \dfrac{1}{M}\left[\sum_{m=0}^{M-1}[R_{TY}(m) - \mu_{TY}]^2\right]^{1/2} \\ \sqrt{A_{TW}} = \dfrac{1}{M}\left[\sum_{m=0}^{M-1}[R_{TW}(m) - \mu_{TW}]^2\right]^{1/2} \end{cases} \tag{4-20}$$

SNR is derived from the quotient of RMS amplitude of $R_{TZ}(m)$ divided by RMS amplitude of $R_{TW}(m)$.

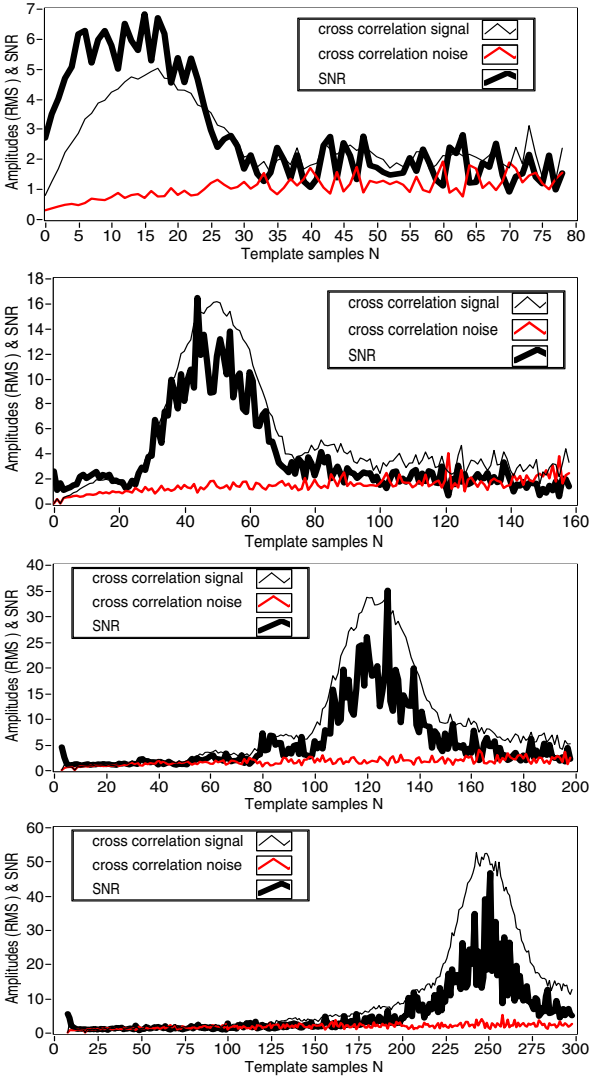

Figure 4.5 RMS amplitude changes of $R_{TY}(m)$, $R_{TW}(m)$ and SNR with template samples N when it has (a) a half sinusoidal waveform, (b) 2 sinusoidal waveforms, (c) 5 sinusoidal waveform and (d) 10 sinusoidal waveforms.

If the template has a half sinusoidal waveforms ($N=p_T/2$), the changes of $R_{TY}(m)$, $R_{TW}(m)$ and SNR with p_T are plotted in figure 4.5(a). If the template has more periods of sinusoidal waveforms ($N = i \cdot p_T/2$, $i \geq 2$), for example, two periods ($i = 4$), five periods ($i = 10$) and ten periods ($i = 20$), the changes of $R_{TY}(m)$, $R_{TW}(m)$ and SNR with p_T are plotted in figure 4.5 (b), figure 4.5 (c) and figure 4.5 (d) respectively. From figure 4.5 (a) to figure 4.5 (d) it can be seen that RMS amplitudes of $R_{TY}(m)$ and SNR is high when template period p_T is generally chosen between 20 and 30, which means template samples are chosen between 10 and 15 for a half waveform, 40 and 60 for two waveforms, 120 and 130 for five waveforms, 240 and 260 for ten waveforms respectively. Beyond those regions, RMS amplitudes of $R_{TY}(m)$ and SNR will drop as small as that of $R_{TW}(m)$. If p_T is chosen from any number in a mathematic interval including or closer to p, and especially $p_T \approx p$, $R_{TY}(m)$ and SNR usually have the highest amplitude value.

From equation (4-18), it cannot directly be distinguished whether or not the change of p_T can influence or modulate the period p of $R_{TY}(m)$ and cause it to change. LabVIEW simulations have indicated that it will change if p_T is chosen from different numbers. It is discussed as follows.

4.2.3.1 A half sinusoidal waveform template

When a half sinusoidal waveform ($N=p_T/2$) of discrete sequence is taken as the template to cross correlate with the 1D sinusoidal grating position-encoded signal $Y(n)$, the waveforms of cross-correlation signal $R_{TY}(m)$ are in varying degree of smoothness if $p_T/2$ is chosen with the number either equal to or different from $p/2$. Several typical cross-correlation signals $R_{TY}(m)$ have been plotted in figure 4.6.

Attention should be paid to the data points in $R_{TY}(m)$. It has data points equal to $256 + p_T/2$. In order to clearly make comparison to each other for signal periods, waveform smoothness etc, at first the extra data points of $p_T/2$ have been subtracted, then cross-correlation signals, resulted from the encoded signal cross-correlated with a half sinusoidal waveform template of 4 samples and 34 samples, are intentionally offset to 1 and 2 arbitrary unit respectively relative to cross-correlation signal which is resulted from encoded signal cross-correlated with a half sinusoidal waveform template of 12 samples. In figure 4.6 three cross-correlation signals are all normalized. From figure 4.6

it can be seen that the cross-correlation signal is the optimum in smoothness when $p_T/2 \approx p/2 = 12$, however the waveforms are rougher when $p_T/2 = 4$, then obviously the waveform has been so modulated when $p_T/2 = 34$ that the periods of the signal is hardly discriminated. In order to see the performance of a half sinusoidal waveform template of 12 samples, when it is cross-correlated with encoded signal, the optimum cross-correlation signal is also plotted there in figure 4.4 by solid gross line. For different $R_{TY}(m)$ signal, the average period $\overline{p}$ of $R_{TY}(m)$ can be calculated, after that the deviation $\delta = \overline{p} - p$ can be calculated too. If the pitch of 1D sinusoidal grating is P (unit: μm or nm), the pitch deviation Δ can be calculated by $\Delta = (\overline{\delta} / p) \cdot P$. For 1D sinusoidal grating encoded simulation signal shown in figure 4.4, with different template samples $N=p_T/2$, the deviations $\delta = \overline{p} - p$ are plotted in figure 4.7. When template sample $N=p_T/2$is chosen between 21 and 27, the arithmetic average of $\overline{\delta}$ is 0.02, the repeatability (STD) is 0.01. For the given simulated signal, p is 25 data points, if P=100 nm is taken as an example, the pitch deviation Δ is 0.08 nm.

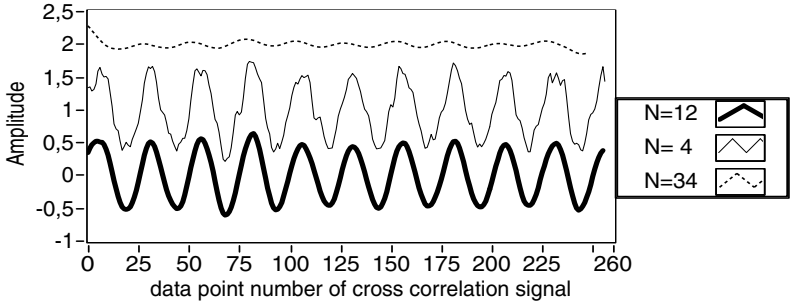

Figure4.6 Waveforms of cross-correlation signal $R_{TY}(m)$ when template samples $N = p_T/2$ is equal to 4, 12 and 34 respectively.

Therefore, when a half sinusoidal waveform ($N = p_T/2$) of discrete sequence is taken as the template, simulation experiments have indicated that the noise can be mostly depressed if p_T is chosen any number in a small mathematic interval including or closer to p, especially $p_T \approx p$. If $p_T << p$, the noise cannot be totally depressed. If $p_T >> p$, to a certain extent the amplitude of $R_{TY}(m)$ drops as small as that of $R_{TW}(m)$, so that SNR is too low to distinguish periodical signal from noise.

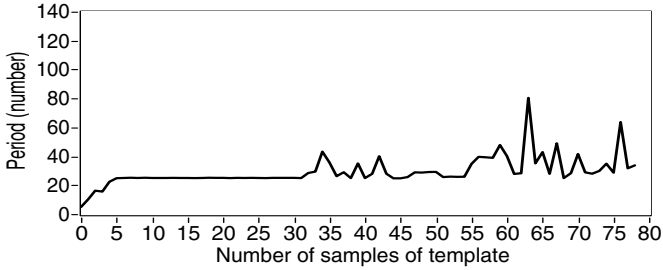

(a)

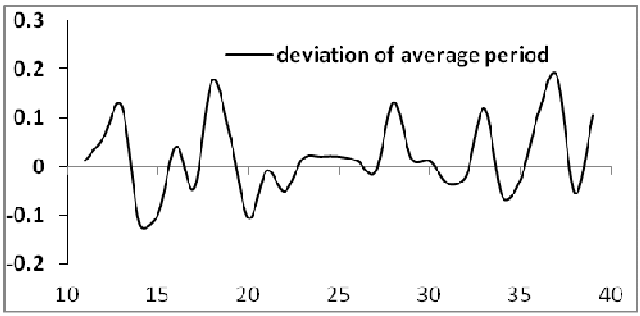

(b)

Figure 4.7 Average period of $R_{TY}(m)$ for 1D sinusoidal grating position-encoded simulation signal when template samples are changing (a) from 1 to 80 and (b) deviations of period from 11 to 39.

4.2.3.2 Multiple waveforms of sinusoidal template

If multiple sinusoidal waveforms of discrete sequence ($N = i \cdot p_T/2$ and $i \geq 2$) are taken as the template $T(n)$, only the situation of $p_T \approx p$ needs to be simulated because the simulation experiments in former section has proven $p_T \approx p$ is the most reliable and accurate choice for a half waveform and multiple waveforms of sinusoidal template.

$Y(n)$ is still simulated by the signal shown in figure 4.4. The sinusoidal template has multiple waveforms with 1 arbitrary unit in amplitude and 25 samples in period ($p_T = 25$). Normalized $R_{TY}(m)$ has been calculated. When the sinusoidal template has 2, 5 and 10 waveforms, which means $i = 4$, 10, 20

and N = 50, 125, 250, $R_{TY}(m)$ have been plotted in figure 4.8. Attention should be paid to the data points in the cross-correlation signals. It is equal to 256 + p_T /2. In order to make clear comparison to each other for signal periods, waveform smoothness etc, at first the extra data points of $i \cdot p_T / 2$ have been eliminated, then $R_{TY}(m)$ signals which result from $Y(n)$ cross-correlated with 5 and 10 sinusoidal waveforms of template are intentionally offset to 1 and 2 arbitrary unit respectively relative to the $R_{TY}(m)$ signal which result from $Y(n)$ cross-correlated with 2 sinusoidal waveforms of template. From figure 4.8 it can be seen that the waveforms of $R_{TY}(m)$ are all very smooth. Nevertheless, the total data points in the cross-correlation signal are $(M + N)$ or $(M + i \cdot p_T/2)$. For integer period counting and fractional parts calculating, only number M of data points in $R_{TY}(m)$ should participate in the displacement calculation, the extra number N of data points must be excluded. The more data points N which participate the cross-correlation calculation are used, the slower the measurement speed ist. Therefore a half waveform of sinusoidal signal sequence is the best choice to be the cross-correlation template, and the template samples $N = p_T/2$ is as equal as possible to the half of period p of 1D sinusoidal grating position-encoded signal.

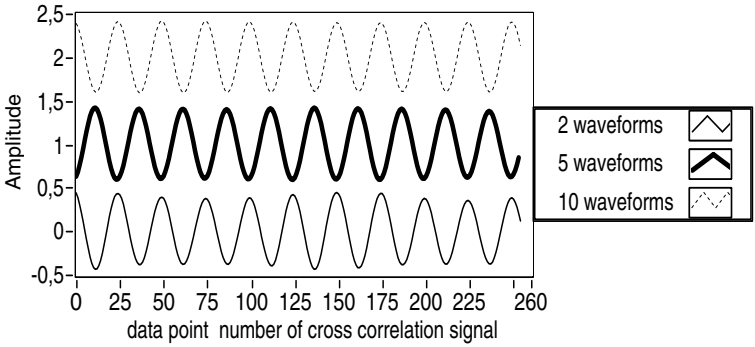

Figure 4.8 Waveforms of $R_{TY}(m)$ when $T(n)$ has the period of 25 samples and has 2, 5 and 10 waveforms respectively.

4.2.4 Real-time cross-correlation filtering to 1D other forms of grating position-encoded signal

A half sinusoidal waveform template can also be applied to filter the other forms of 1D grating position-encoded signals in real time, such as 1D rectangular grating, 1D triangular grating etc.

In section 4.2.2 it has been mathematically stated that a low frequency tilt signal express by a polynomial function $U(n) = H_0 + H_1 \cdot n + \cdots + H_K \cdot n^K$ ($0 \leq n < M$-1), after cross-correlated with a half sinusoidal waveform template, remains a low frequency tilt signal presented by $R_{TU}(m)$ as shown in equation (4-12). If the polynomial function has only constant item $U(n) = H_0$ or constant item plus monomial item $U(n) = H_0 + H_1 \cdot n$, it is a straight line parallel to or cross with the numerical axis. 1D rectangular waveform signal and 1D triangular waveform signal can be considered to be made up by many such horizontal lines and oblique straight lines respectively, therefore after cross-correlated with a half sinusoidal waveform template, the signals are still in rectangular waveform and triangular waveform.

Their FPS prove this. The spectra of simulated 1D rectangular grating and 1D triangular grating encoded signal of one arbitrary unit in amplitude without noise before and after cross-correlation filtering are plotted in figure 4.9 (a), figure 4.9 (b) and figure 4.10 (a), figure 4.10 (b) respectively, and with white noise of 0.5 arbitrary units in amplitude before and after cross-correlation filtering are plotted in figure 4.9 (c), figure 4.9 (d) and figure 4.10 (c) and figure 4.10 (d) respectively. Apparently the power spectra are almost in the same spectra distribution before and after cross-correlation filtering.

Compared with the derivation of cross-correlation tilt signal equations from (4-9) to (4-13), 1D rectangular grating and 1D triangular grating encoded signals are so similar and simple. Only the simulation results are presented 1D rectangular grating and 1D triangular grating position-encoded signal $Y(n)$ is generated respectively by mixing the square waveform signal and triangle waveform signal $Z(n)$ of 1 arbitrary unit in amplitude and 25 data points in period with white noise $W(n)$ of 0.5 arbitrary unit in amplitude and 256 data points. Taking them as an example, RMS amplitude of $R_{TY}(m)$, RMS amplitude of $R_{TW}(m)$ and SNR are calculated respectively from it.

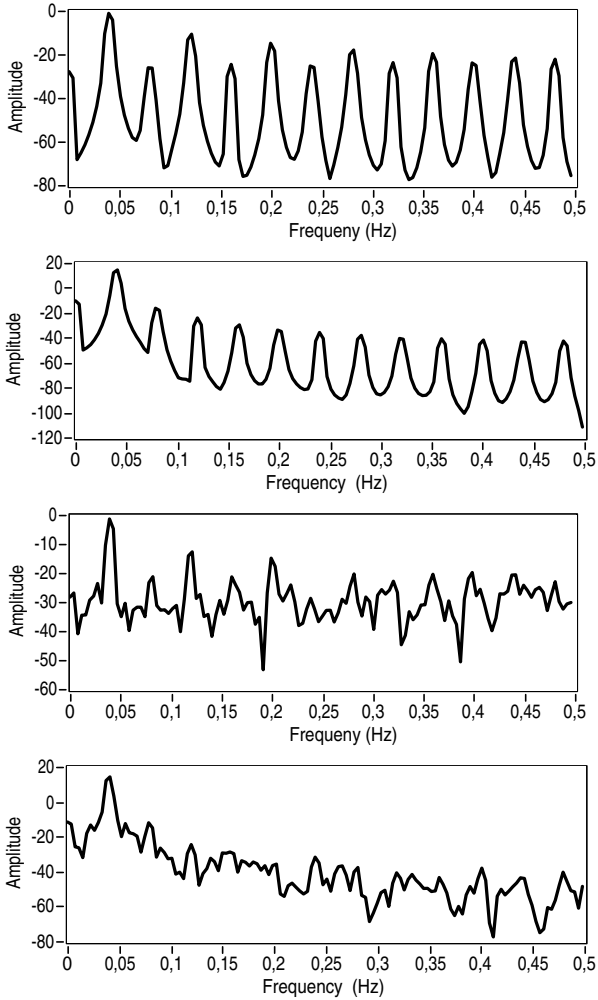

Figure 4.9 (a) and (c) are the spectra of rectangular signal without and with noise of 0.5 arbitrary units; (b) and (d) are the spectra of cross-correlation signals filtered from (a) and (c) respectively.

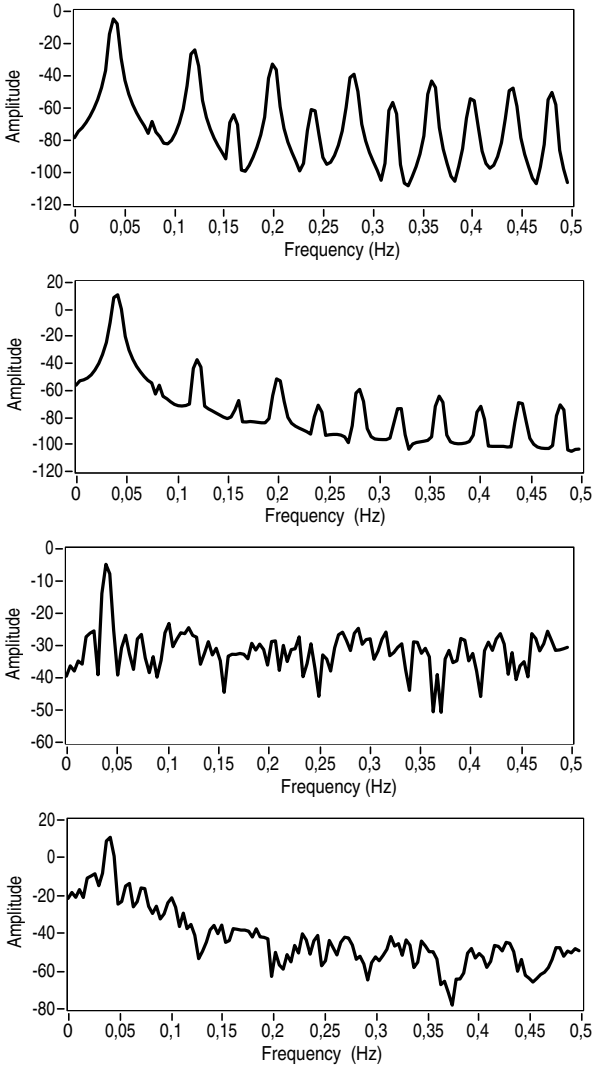

Figure 4.10 (a) and (c) are the spectra of triangular signal without and with noise of 0.5 arbitrary units; (b) and (d) are the spectra of cross-correlation signals filtered from (a) and (c) respectively.

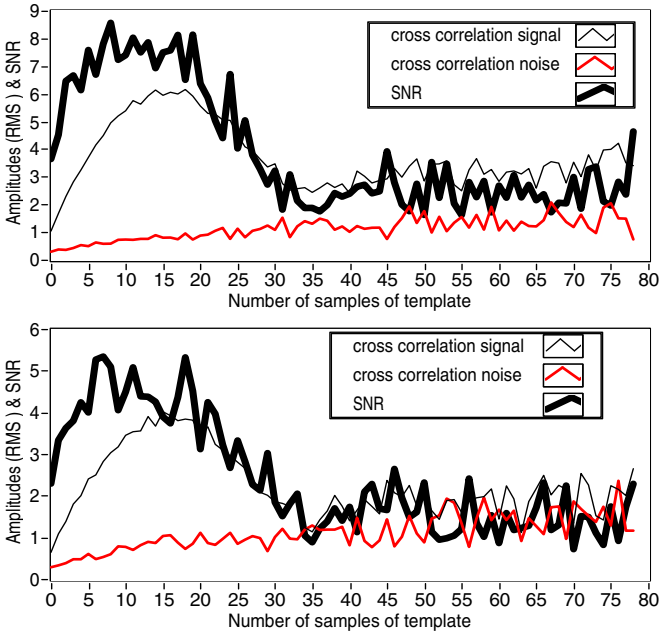

Figure 4.11 RMS amplitudes $R_{TY}(m)$, $R_{TW}(m)$ and SNR change with a half sinusoidal waveform template samples N for simulated encoding signal of 1D rectangular grating in (a) and 1D triangular grating in (b).

If the template has a half sinusoidal waveform ($N = p_T/2$), the changes of $R_{TY}(m)$, $R_{TW}(m)$ and SNR with p_T are presented in figure 4.11 (a) and figure 4.11 (b) respectively for 1D rectangular grating encoded signal and 1D triangular encoded signal. Cross-correlation signal $R_{TY}(m)$ generated by cross-correlating $Y(n)$ with a half sinusoidal waveform template $T(n)$ of 12 samples is shown by solid thick lines in figure 4.12 (a) and 4.12 (b) respectively, while 1D rectangular grating and 1D triangular grating encoded signals are shown by solid thin lines in figure 4.12 (a) and 4.12 (b) respectively. Also from different sequences of $R_{TY}(m)$, the average periods $\overline{p}$ of $R_{TY}(m)$ have been calculated. For different template samples $N = p_T/2$, from 1 to 80 the deviation $\delta = \overline{p} - p$ is plotted in figure 4.13 (a) and figure 4.13 (b) respectively. For small mathematical interval including p the deviation δ is plotted in figure 4.14 (a) and figure 4.14 (b) respectively.

When $N = p_T / 2$ is chosen from 12 to 25 for 1D rectangular grating position-encoded signal and from 22 to 25 for 1D triangular grating position-encoded signal, the arithmetic averages of $\overline{\delta}$ is 0.03 and 0.02 respectively, and the repeatability (STD) is 0.02 and 0.01 respectively. If P = 100 nm is taken as an example, the deviation of signal period Δ is 0.12 nm and 0.08 nm respectively.

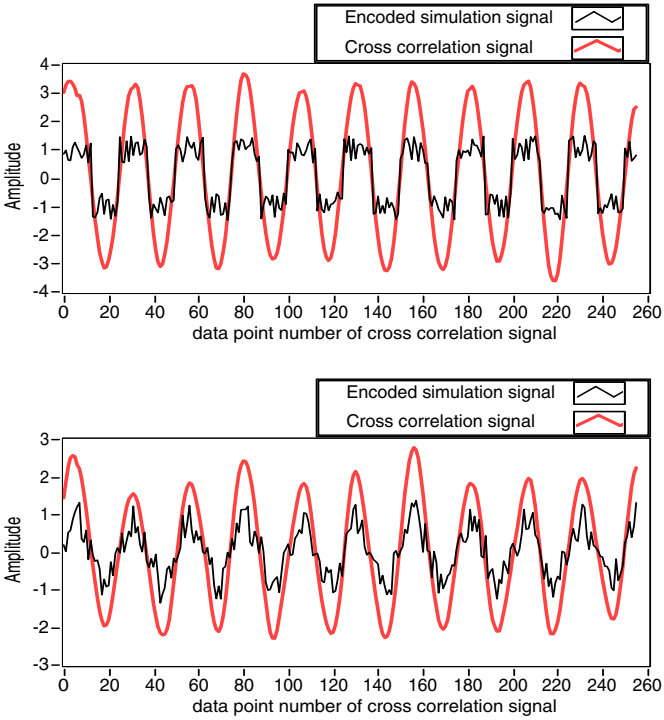

Figure 4.12 Simulation of 1D rectangular grating and 1D triangular grating position-encoded signal and their $R_{TY}(m)$ is shown in (a) and (b) respectively.

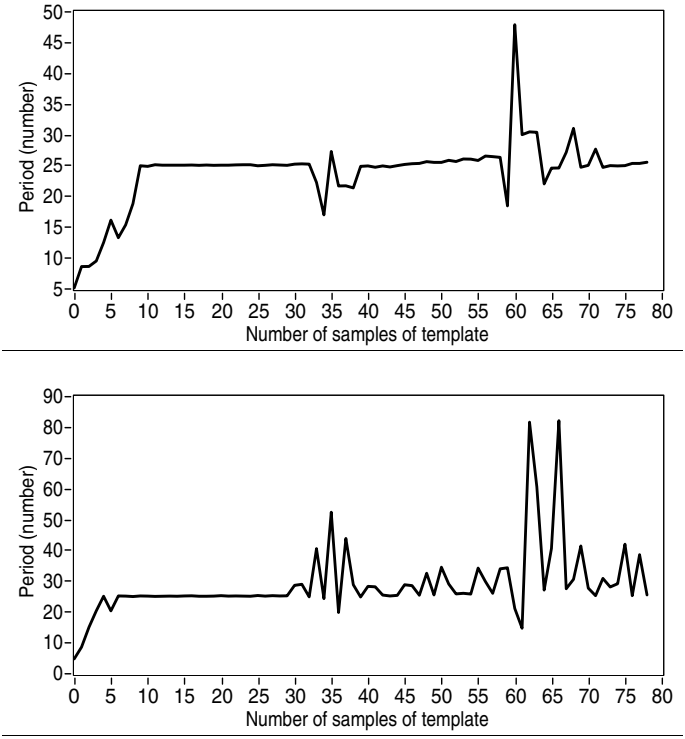

Figure 4.13 Average period of $R_{TY}(m)$ for 1D rectangular grating and 1D triangular grating position-encoded simulation signals are shown in (a) and (b) respectively when their template samples are changing from 1 to 80.

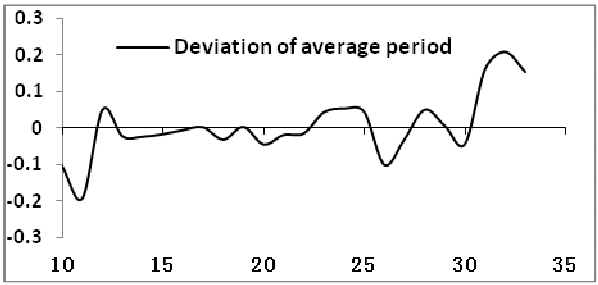

(a)

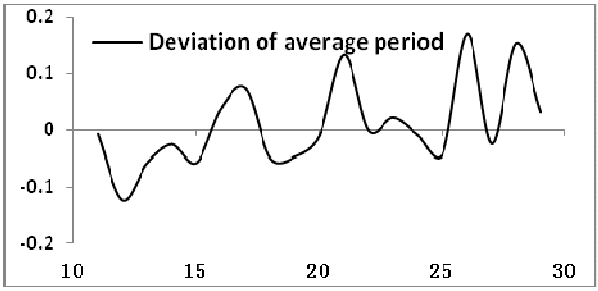

(b)

Figure 4.14 Deviations of average period of $R_{TY}(m)$ for 1D rectangular grating and 1D triangular grating position-encoded simulating signals are shown in (a) and (b) respectively when the template samples change from 10 to 33 and from 11 to 29.

4.3 Real-time one direction displacement measurement

4.3.1 Computing algorithm of displacement decoding

As discussed in the previous section, a half sinusoidal waveform template can be used as a real-time filter in combination with cross-correlation technique. When the template is cross-correlated with 1D grating position-encoded signal $Y(n)$ scanned by AFM cantilever, and if the period of this half sinusoidal waveform template is approximately equal to that of 1D grating position-encoded signal, the noise can be very effectively filtered in real time. The displacement is calculated by directly counting the integer pitch plus calculating the fractional part at the beginning and at the actual position from

the real-time processed cross-correlation signal $R_{TY}(m)$ but not from $Y(n)$, based on the following criteria and algorithms.

If encoded signal is directly decoded, the calculations of fractional part *fs* at the beginning and fractional part *fe* at the end need the first and the last integer period data point number of encoded signal as reference respectively. Take the signals in figure 4.1 as an example, if the peak positions of cross-correlation signal $R(n)$ are automatically detected as $A(1)$, $A(2)$,$\cdots$, $A(i\text{-}1)$, $A(i)$, and the scanning step number is n, the fractional parts *fs* and *fe* will be

$$fs = A(1)/[A(2) - A(1)] \tag{4-21}$$

$$fe = [n - A(i)]/[A(i) - A(i-1)] \tag{4-22}$$

Therefore the real-time displacement measurement results can only be given starting from the second or third pitch if equation (4-1) is directly applied. In such case, the disadvantage of this decoding technique is that there will be no real-time displacement measurement results corresponding to 1D grating position-encoded signal of fractional part *fs* from the beginning to the first integer period, although this part of displacement can be easily added after an elapse of one or several seconds of time.

4.3.2 Encoding modes

Based on the stage whose displacement needs to be measured, there are possibly two kinds of data acquisition mode: one can be called active encoding mode (AEM) and another can be called passive encoding mode (PEM).

In AEM, the micro-moving stage can be controlled by computer to move to a preset distance and stop using the displacement decoded from the 1D grating position-encoded signals. The movement is monitored by AFM cantilevers encoder through real-time displacement measurement. The flowchart for AFM cantilever is illustrated in figure 4.15 (a). Every time the 1D sinusoidal grating moves e.g. a step forward, a position-encoded data along its displacement direction will be picked up by AFM cantilever. The data will be decoded into the displacement according to the decoding principle explained

in the previous section. The result will be compared with the preset distance value. If the result is less than the preset distance the scanning stage will be controlled to move forward to the next point. The routine will continue until the measured displacement is equal to the preset distance. Then the movement of micro-moving stage and measurement process will be stopped automatically.

In PEM, the micro-moving stage is moved or stopped by other sources like signal generator or another computer. In this case AFM cantilever encoder does real-time displacement measurement to monitor it, but has no control to it. The flowchart for PEM is illustrated in figure 4.15 (b). In this case only the measurement process can be stopped no matter the preset distance is reached or not.

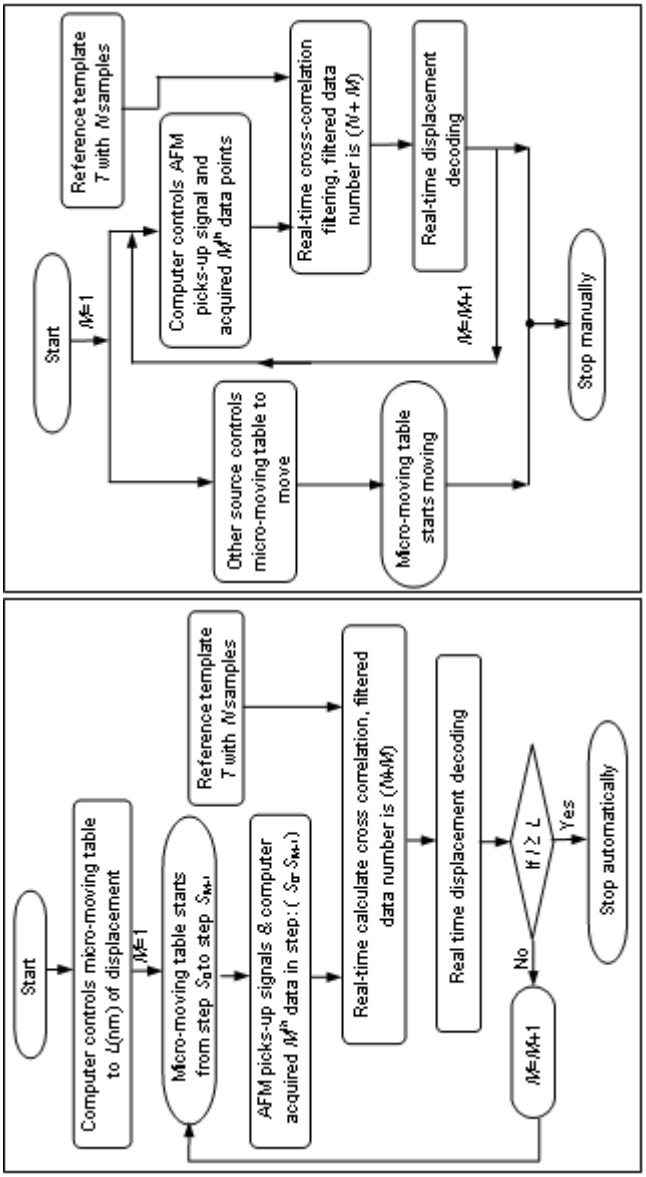

Figure 4.15 Flowcharts of real-time displacement measurements in (a) AEM and (b) PEM.

4.4 Experiments and results

If not specified, the data acquisition and displacement measurement are all based on AEM.

4.4.1 Real-time filtering to sinusoidal grating position-encoded signal

A typical 1D sinusoidal grating position-encoded signal $Y(n)$ with noise $W(n)$ and tilt $U(n)$ scanned by TF cantilever encoder is shown in figure 4.16 (a). Based on the rough calculation, the period of 1D sinusoidal grating encoded signal is about 85 data points. Therefore it is cross-correlated with a half sinusoidal waveform template $T(n)$ with 1 arbitrary unit in amplitude and 85 samples (N=85). Cross-correlation signal $R_{TY}(m)$ is shown in figure 4.16 (b). The low frequency tilt component in encoded signal shown in figure 4.16 (a) can be seen in cross-correlation signal shown in figure 4.16 (b).

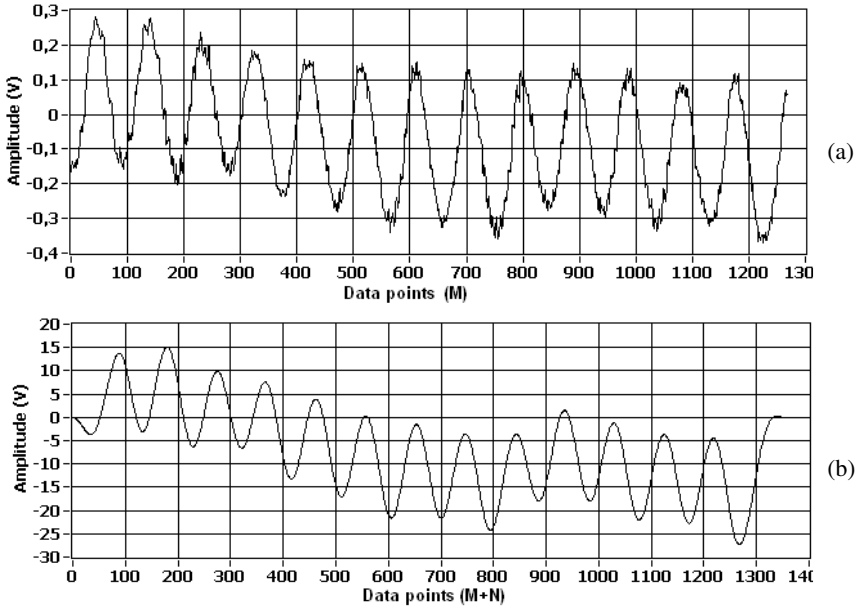

Figure 4.16 Real-time cross-correlation illustration, where (a) is 1D sinusoidal grating encoded signal, and (b) is cross-correlation signal (not normalized).

Cross-correlation template is also applied for real-time filtering amplitude-modulated sinusoidal signal as shown in figure 4.17 (a), which is generated when a 2D sinusoidal grating of 300 nm in pitch is scanned by a TF-AFM along direction *l* as shown in its 3D topographic figure 4.17(b).

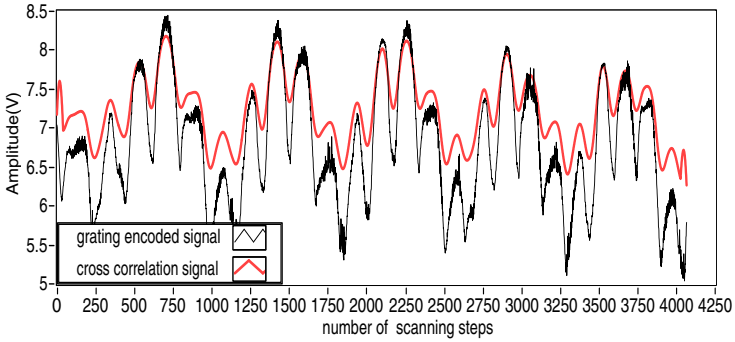

(a)

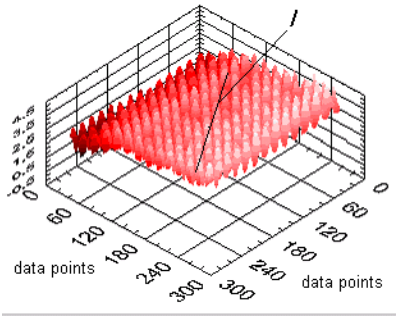

(b)

Figure 4.17 Cross-correlation filtering of 2D sinusoidal grating encoded signal in (a) when the grating in (b) is scanned in direction ***l*** by TF-AFM.

4.4.2 Real-time filtering and decoding to 1D grating position-encoded signal

A half sinusoidal waveform template has been applied for real-time filtering a 1D sinusoidal grating position-encoded signal and 1D rectangular grating

position-encoded signal scanned by TF cantilever as the encoding sensor. In order that the noised signal and cross-correlation signal filtered by cross-correlation template can be seen clearly, the piezoelectric scanning stage is randomly controlled to move to a preset short displacement value of 2947.43 nm at various step spacing. The step spacing means that piezoelectric scanning stage is controlled to move under 4 different step voltages. They can be called single step (Step 1), double step (Step 2), triple step (Step 3) and fourfold step (Step 4) with step voltage of 0.30538 mV, 0.61076 mV, 0.91614 mV and 1.22152 mV respectively. This means that the total number of scanning steps will decrease with the increase of step voltage for a preset displacement of 2947.43 nm. Also piezoelectric scanning stage is randomly chosen to move under open-loop or closed-loop controlled by its own controller. 300 nm in pitch and 80 nm step height 1D sinusoidal grating encoded signals as well as 200 nm in pitch and 60 nm step height 1D rectangular grating encoded signal are scanned by TF cantilever. Simultaneously the displacement can be measured in real time. As soon as the measured displacement is equal to the preset displacement, the piezoelectric scanning stage is stopped immediately by the program.

Because 1D grating encoded signal has different period p when scanning stage is controlled to move at different step spacing, a half sinusoidal waveform template with 1 arbitrary unit in amplitude and with different samples $N = p_T/2$ is applied as real-time digital filter, which are 80, 40, 30 and 20 for single step, double step, triple step and fourfold step respectively. Those template samples $p_T/2$ is selected only within a mathematic interval including or near to one half of encoded signal period $p/2$ but unnecessary equal to $p/2$ according to the mathematical analysis in this paper. Single time measurement results including scanning steps M, integer lengths $I \times P$ (nm), fractional lengths $(fs+fe)\cdot P$ (nm) and displacements $I \times P+(fs+fe)\cdot P$ (nm) etc are listed in table 4.1.

Here the purpose is not to prove how repeatable the displacement measurement in any step spacing but to compare the displacement measurement results in different step spacing. Because the resolution is decreased with the increase of step spacing, not very well repeatable but less variable and a little gradually increasing measurement results relative to the preset 2947.43 nm are predicted and expected. It should be noticed that there always exists a small in-plane tilt angle α between 1D grating orientation and scanning stage moving direction. If this angle is considered, the reference

pitch P of 1D grating in equation (4-1) should be $P/\cos\alpha$. Here in table 4.1 the real-time displacement measurement is performed based on the premise that displacement direction is perpendicular to 1D grating lines, i.e. $\alpha = 0$.

Table 4.1 Displacement measurement results obtained for a preset displacement of 2947.43nm.

Step spacing	1D grating	Scanning Steps M	Template samples N	Integer length(nm)	Fractional length(nm)	displacement (nm)
Step 1	Sinusoidal	1721	80	2700	247.928	2947.93
Step 2	Sinusoidal	869	40	2700	248.383	2948.38
Step 3	Sinusoidal	584	30	2700	247.996	2948.00
Step 4	sinusoidal	445	20	2700	251.041	2951.04
Step 1	Rectangular	1800	60	2800	148.740	2948.74
Step 2	Rectangular	908	40	2800	149.250	2949.24
Step 3	Rectangular	609	30	2800	148.645	2948.65
Step 4	Rectangular	454	20	2800	153.247	2953.25

The 1D 300nm pitch sinusoidal grating position-encoded signals and their cross-correlation signals are plotted in figure 4.18 (a), figure 4.18 (b) when the scanning stage is driven to move at single step and double step. 1D rectangular grating (200nm pitch) position-encoded signals and their cross-correlation signals are plotted in figure 4.18 (c) and figure 4.18 (d), when scanning stage is driven to move at triple step and fourfold step. From the figures, periods of encoded signal and different number of total scanning steps caused by either different pitch of 1D grating or different driving step voltage can be seen.

Likewise, a half sinusoidal waveform template has been applied for real-time filtering four kinds of 1D rectangular grating position-encoded signals scanned by TF cantilever. Four pieces of 1D rectangular grating have pitch of 80 nm, 100 nm, 120 nm and 160 nm respectively. In order that the noised signal and cross-correlation signal filtered by cross-correlation template can be seen clearly, the piezoelectric scanning stage is randomly controlled to move to a preset shorter displacement of 855.42 nm when x piezoelectric scanning stage is driven to move by single step voltage.

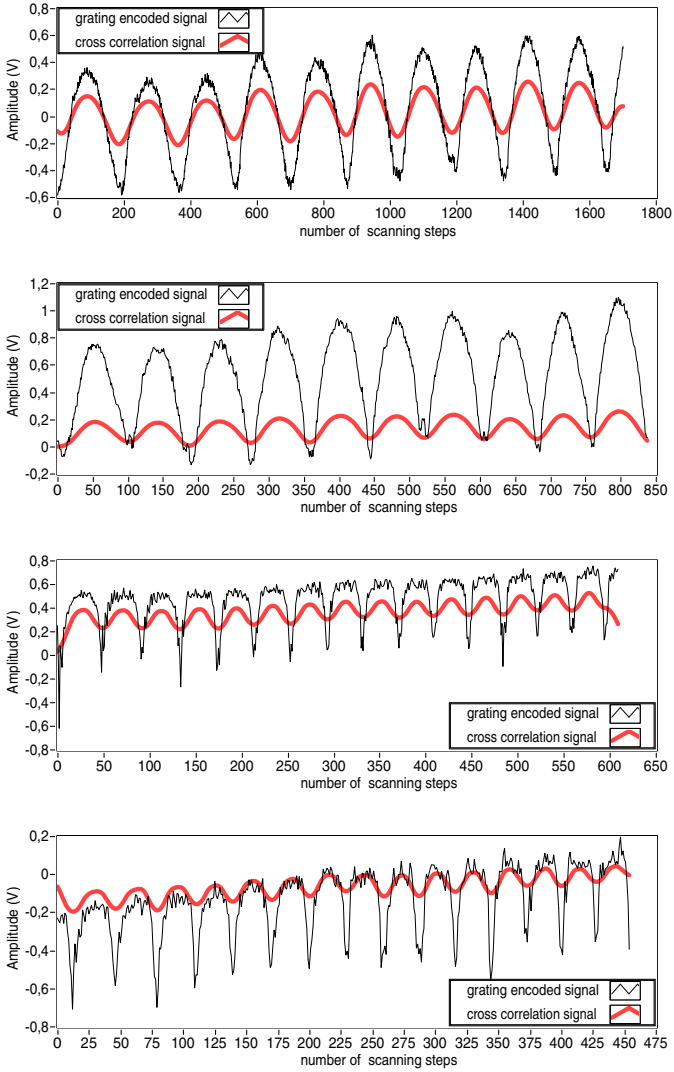

Figure 4.18 1D sinusoidal and 1D rectangular grating position-encoded signals and cross-correlation signals are plotted with single step in (a), double step in (b), triple step in (c) and fourfold step in (d) respectively.

Table 4.2 Displacement measurement results for a preset displacement of 855.42nm.

grating pitch (nm)	Template samples	Scanning steps	Integer periods	Integer length(nm)	Fractional length(nm)	displacement (nm)
80	40	528	9	720	135.281	855.28
100	40	533	7	700	160.530	860.53
120	60	536	6	720	134.895	854.90
160	60	525	4	640	215.874	855.87

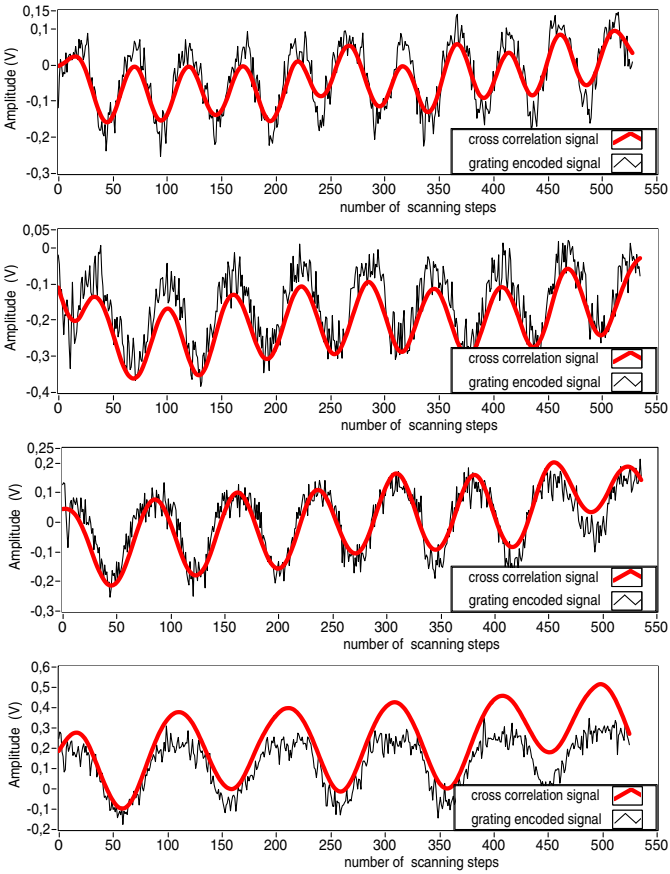

Figure 4.19 1D rectangular (a) 80 nm, (b) 100 nm, (c) 120 nm and (d) 160 nm pitch grating position-encoded signals and their cross-correlation signals.

Single time measurement results including scanning steps M, integer lengths $I \times P$ (nm), fractional lengths $(fs + fe) \cdot P$ (nm) and displacements $I \times P + (fs + fe) \cdot P$ (nm) etc are listed in table 4.2. Encoded signals and cross-correlation signals are plotted in figure 4.19 (a), 4.19 (b), 4.19 (c) and 4.19 (d) respectively.

4.4.3 Real-time displacement measurements in PEM

With preset displacement of 5460.6 nm, ramp voltages with two kinds of configuration output from signal generator are applied to the x-piezoelectric scanning stage:

(1) different frequency of 1 mHz, 2 mHz, 5 mHz and 10 mHz and amplitude of 5 Vpp,
(2) 1mHz in frequency and 1 Vpp, 2 Vpp, 3 Vpp and 4 Vpp in amplitude.

he 1D grating encoded signals with different periods, in configuration (1) caused by different frequencies of ramp voltage and in configuration 2 caused by different amplitudes of ramp voltage, are plotted together in figure 4.20 (a) and 4.20 (b) respectively. Correspondingly measured displacements are drawn together in figure 4.21 (a) and 4.21 (b) respectively. Single time measurement results including scanning steps M, integer lengths $I \times P$ (nm), fractional lengths $(fs+fe) \times P$ (nm) and displacements $I \times P + (fs+fe) \times P$ (nm) etc are listed in table 4.3.

If displacement is measured in PEM mode, when the measured micro-moving stage is controlled individually by other voltage sources or signal generator to move at a reasonable speed, for example ramp voltage at 1mHz in frequency and 4 Vpp, 3 Vpp and 2 Vpp in amplitude respectively, or 5 Vpp in amplitude and 10 mHz, 5 mHz and 2 mHz in frequency respectively, real-time displacement is measured at changing speed, fast at beginning and gradually slow with encoded signal data accumulating more and more, so that the periods of encoded signal are gradually decreasing with the increasing of acquired data like corresponding waveforms shown in figure 4.20 (a) and 4.20 (b), and corresponding displacement curve is basically smooth as shown in figure 4.21 (a) and 4.21 (b). However when it moves at very slow speed, for example ramp voltage at 1mHz in frequency and 1Vpp in amplitude, or 1mHz in frequency and 5Vpp in amplitude, real-time displacement is

measured at slowly changing speed, slow at beginning and gradually much slower with encoded signal data accumulating more and more, so that the periods of encoded signal is much larger compared with those of other encoded signals in figure 4.20 (a) and 4.20 (b) for configuration 1 and 2 respectively, and corresponding displacement curve respectively on the very right side in figure 4.21 (a) and 4.21 (b) is rising bumpily.

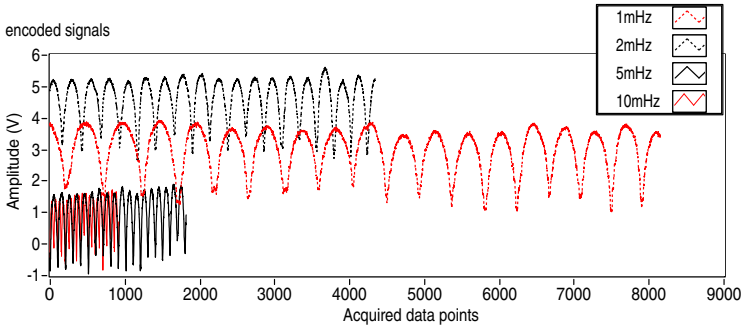

(a)

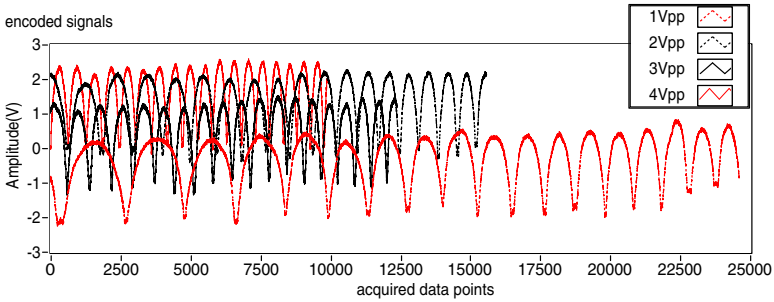

(b)

Figure 4.20 Encoded signals in PEM in (a) and (b) when scanning stage is driven by ramp voltage from a function generator in configuration (1) and (2) respectively.

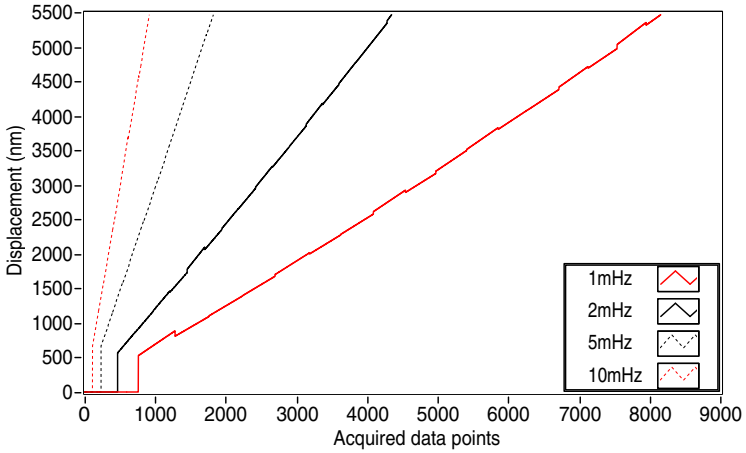

(a)

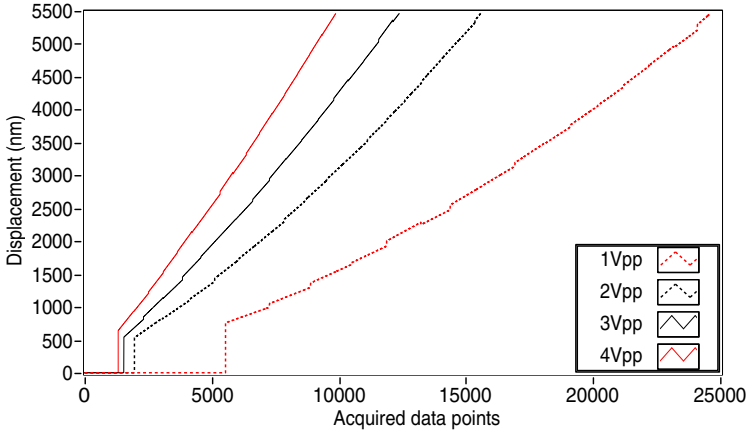

(b)

Figure 4.21 Real-time displacement curves in PEM in (a) and (b) when scanning stage is driven by ramp voltage with configuration 1 and 2 respectively.

Table 4.3 Measurement results when x-piezoelectric scanning stage is driven by ramp voltage with different frequency and amplitude.

Move speed		Template samples N	Steps M	Integer Number I	Fractional parts(nm) $(fs+fe)\cdot P$	displacement (nm) $I\times P+(fs+fe)\cdot P$
freq. (mHz)	ampl. (Vpp)					
1	1	400	24618	19	360.910	5460.62
1	2	320	15579	19	360.834	5460.83
1	3	160	12377	19	361.007	5461.01
1	4	120	5624	19	360.679	5460.68
1	5	80	8159	19	360.822	5460.91
2	5	80	4348	19	361.718	5461.70
5	5	40	1823	19	361.473	5461.45
10	5	20	918	19	361.577	5461.57

4.4.4 The applications of real-time displacement measurement

4.4.4.1 Hysteresis of piezoelectric scanning stage

Using TF cantilever paired with 1D sinusoidal grating of 300 nm in pitch, forward and backward displacements as well as hysteresis of a piezoelectric scanning stage as function of scanning steps have been measured. The stage is driven by single step voltage in open-loop and closed-loop mode based on its built-in capacitance. The results are shown in figure 4.22, where closed-loop forward and backward displacements are presented by solid thin line and dotted thin line in figure 4.22 (a), while the open-loop forward and backward displacements are presented by solid thin line and solid thick line in figure 4.22 (b). The given displacement is 68363.2 nm. Actually the measured forward and backward displacements for open-loop are 68364.3 nm and 64518.4 nm and for closed-loop are 68365.0 nm and 68402.9 nm respectively. The measured hysteresis is 13738.2 nm for open-loop mode and 292.1 nm for closed-loop mode within 70 μm range of movement.

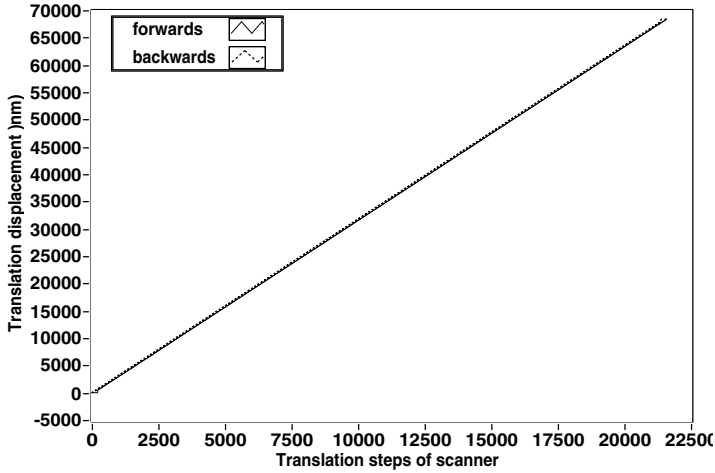

(a)

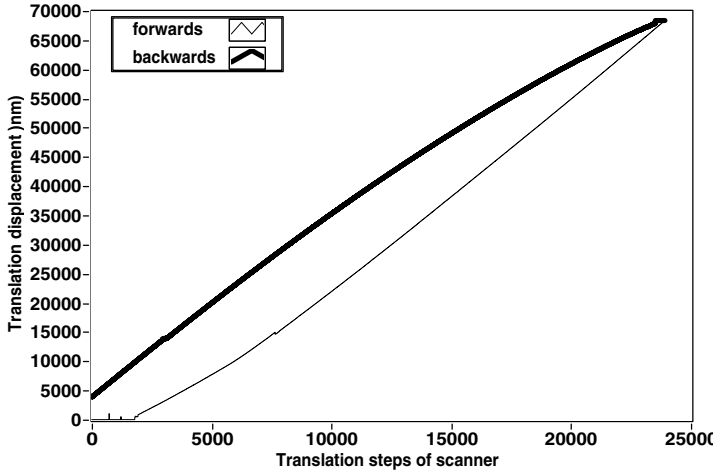

(b)

Figure 4.22 Real-time forward and backward displacement measurements of a piezo scanning stage when it is driven in (a) closed-loop control and (b) open-loop control.

4.4.4.2 In-plane small tilt angle

It is supposed that 1D grating is probed by one or two TF AFM cantilevers encoder in the displacement direction (forward or/and backward) perpendicular to the grating lines. Based on this the mathematics derived for displacement decoding from encoded signals probed in section 2.3 by two AFM cantilevers and in section 4.1 by one AFM cantilever as encoder. However in real measurement, there always exists a small tilt angle α between 1D grating orientation and displacement direction of the micro moving stage. Thus the pitch value along the displacement direction is $P / \cos\alpha$. For example, equation (4-1) should be

$$S = (fs + I + fe) \cdot P / \cos\alpha \tag{4-23}$$

α can be measured easily in the following procedures by performing an image scan of 1D grating *in x-y* plane. An example of small tilt angle is shown by the scanned image in figure 4.23 (a).

The stage is moved in the *x*-direction over *k* periods of the grating, whereas if the grating is tilted a small angle α, it will result in a change or shift of grating structure in the *y*-direction. The encoded signal sequences are $Y_1(n)$, $Y_2(n)$, ⋯, $Y_m(n)$. Cross-correlation signals $R_1(n)$, $R_2(n)$, ⋯, $R_m(n)$ could be obtained by applying cross-correlation filtering. The peak positions of each sequence of cross-correlation signals can be acquired in real time. Each peak corresponds to one line of 1D grating. Using *m* lines of scan in *y*-direction, there are totally m peak position data in each grating line along y-direction. For any scanned 1D grating line *i* (i = 1, 2, ⋯ , k), a least square fitting line $Y = A_i \cdot x + B_i$ is fitted to *m* peak position data. For each peak line the tilt angle α = arctan (A_i) is calculated. The average tilt angle should be

$$\alpha = \frac{1}{k}\sum_{i=1}^{k} A_i \tag{4-24}$$

For the example shown in figure 4.23 (a), 800 data points and 40 lines in *x*- and *y*-direction respectively are data-acquired. However the scanning steps are all 800 in *x*- and *y*-direction, which mean that data interval is 1 step in *x*-direction and line interval is 20 steps in *y*-direction. Eight 1D grating lines are measured and totally 8×9 peak coordinates are recorded as shown in figure 4.23 (b). Measurement results including each angle of eight lines, average angle and standard deviation (STD) are listed in table 4.4.

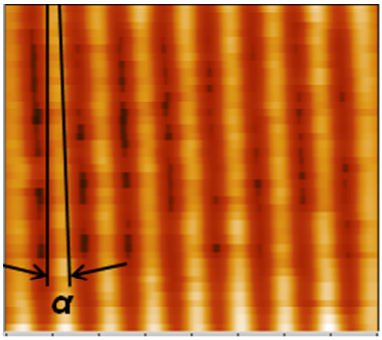

(a)

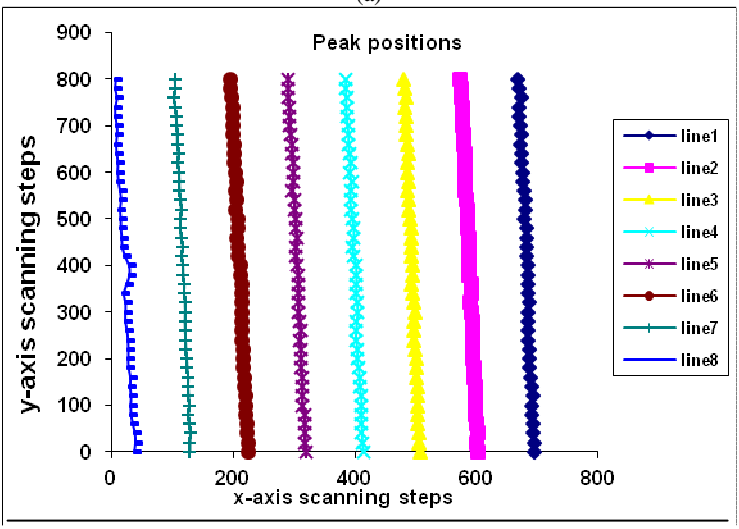

(b)

Figure 4.23 An example of small tilt angle measurement with (a) image of 1D grating orientation and (b) peaks positions of eight 1D grating lines.

Table 4.4 Measurement results of in-plane tilt of small angle α.

Angle measurement results (°)				Average (°)	STD (°)
-2.37	-1.84	-2.01	-2.04	-1.94	0.19
-1.93	-1.82	-1.95	-1.76		

4.4.4.3 In-plane rotation angle within 90° range

The decoding principle of direct integer period counting plus fractional calculation from encoded signal probed by one AFM cantilever can be employed for the measurement of in-plane big rotation angle between 1D grating orientation and micro-moving stage. Suppose that at the beginning the angle between 1D grating lines and horizontal *x*-axis is zero, which means 1D grating lines are parallel to horizontal axis as shown in figure 4.24 (a). If $o(x,y)$ is the centre of rotation table, *Ps* is the position of the AFM cantilever tip, when rotation table rotates counterclockwise by a angle α, the movement of 1D grating changes in-plane position relative to AFM cantilever tip from P_s to P_e as shown in figure 4.24 (b).

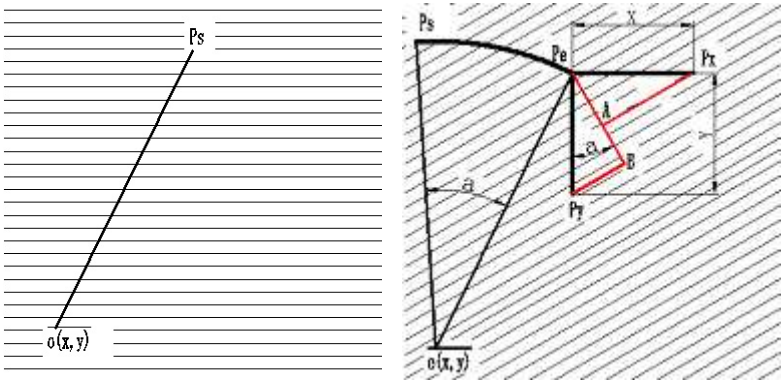

(a) (b)

Figure 4.24 Schematic of rotation angle measurement, in which (a) and (b) are AFM cantilever position, orientation of 1D grating lines of at the beginning and after rotating by α angle respectively.

If an *x*-*y* micro moving stage moves the 1D grating by a preset displacement *X* from P_e to P_x and then return back to P_e, afterwards moves the 1D grating by a reset displacement *Y* from P_e to P_y and then return back to P_e. According to one AFM cantilever decoding equation (4-1), *X* and *Y* can be respectively expressed as

$$X = (fsx + Ix + fex) \cdot P / \sin\alpha \tag{4-25}$$

and

$$Y = (fsy + Iy + fey) \cdot P / \cos\alpha \tag{4-26}$$

where, *Ix*, *fsx* and *fex* are the count of integer periods, fractional part at the beginning and fractional part at the end of *x* directional encoded signal respectively; *Iy*, *fsy* and *fey* are the count of integer periods, fractional part at the beginning and fractional part at the end of *y* directional encoded signal respectively. Therefore

$$\alpha = \arctan(\frac{Y}{X} \cdot \frac{Ix + fsx + fex}{Iy + fsy + fey}) \tag{4-27}$$

Three different in-plane orientation angles of 1D sinusoidal grating of 300 nm in pitch are imaged in figure 4.25 (a), figure 4.25 (b) and figure 4.25 (c) respectively, which are denoted as I, II and III. Here images have the resolution of 800 points and 40 lines in AEM along *x* and *y* direction respectively, but *x*- and *y*- piezoelectric scanning stages are both closed-loop controlled to move 800 steps by their own built-in capacitance sensors with non-linearity less than 0.1%.

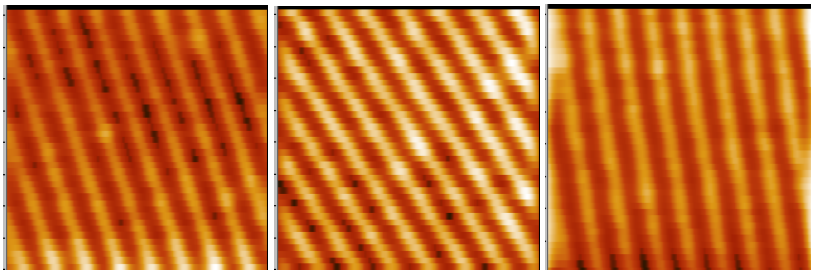

(a) (b (c)

Figure 4.25 (a), (b) and (c) are the images of 1D sinusoidal grating with in-plane orientation angle I, II and III.

If the *x*-*y* piezoelectric scanning stage is closed-loop controlled by its own built-in capacitance sensors with non-linearity less than 0.1% to move the same number of steps with same speed, and the starting point *Pe* is also controlled by x capacitance sensor and y capacitance sensor to ensure its repeatability, *X* and *Y* are almost equal. So that equation (4-27) can be rewritten as

$$\alpha = \arctan\left(\frac{Ix + fsx + fex}{Iy + fsy + fey}\right) \tag{4-28}$$

For in-plane orientation angles I, II and III which are respectively shown in figure 4.25 (a), (b) and (c), if their *X* and *Y* displacements are preset 3000, 2000 and 3000 scanning steps in closed-loop control and data-acquired in AEM mode, the results of 10 times of angle measurement averages, as well as STDs are listed in table 4.5.

Table 4.5 In-plane big angle measurement results

angle	Angle measurement results (°)					Average (°)	STD (°)
I	21.5601	21.5733	21.5690	21.5441	51.5467	21.57	0.02
	21.5434	21.5483	21.5741	21.6145	21.6140		
II	35.1994	35.1158	35.0793	35.0842	35.1194	35.12	0.04
	35.1321	35.0903	35.0649	35.1325	35.1343		
III	12.0863	12.0726	12.0552	12.0106	12.0054	12.03	0.05

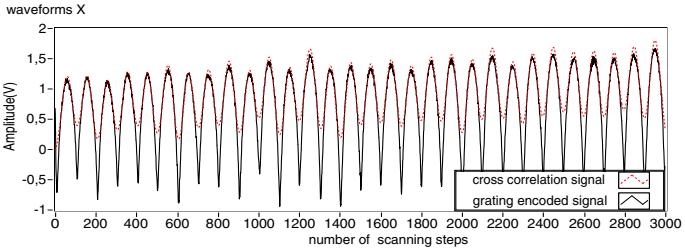

(a)

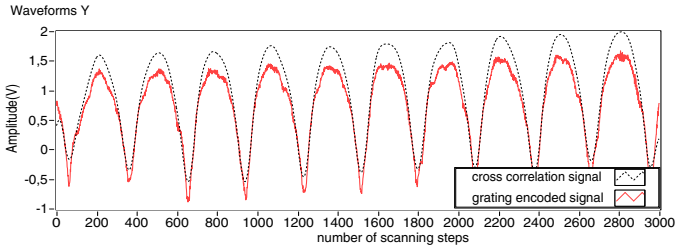

(b)

Figure 4.26 Encoded and cross-correlation signals along *x*-axis and *y*-axis are shown on left side and right side respectively. (a) and (b) correspond to orientation angle I.

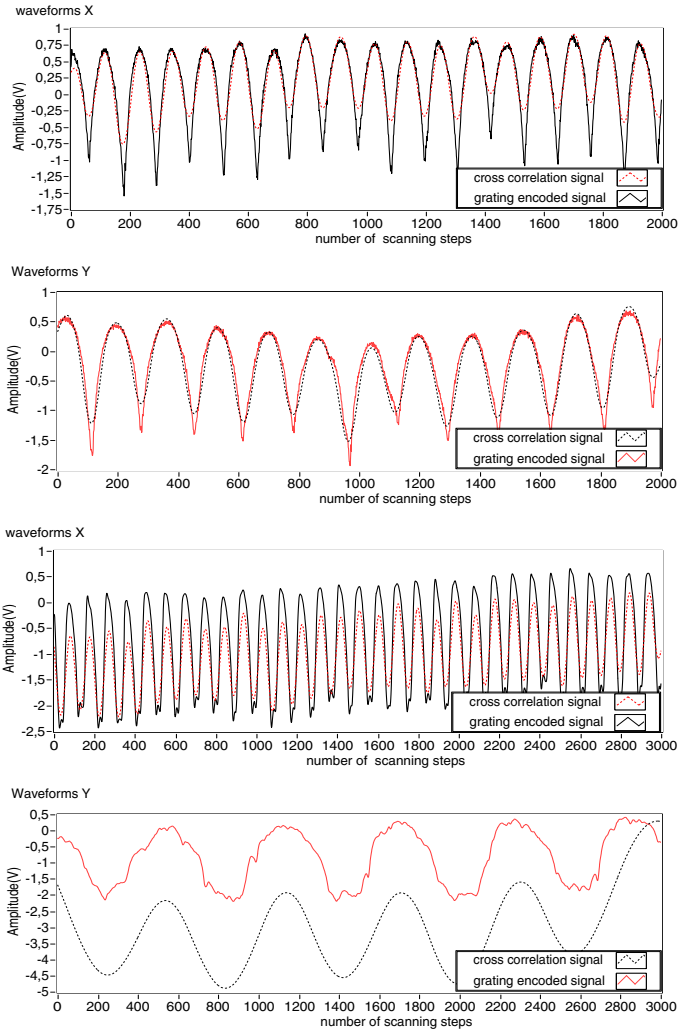

Figure 4.26 Encoded and cross-correlation signals along *x*-axis and *y*-axis are shown on left side and right side respectively. (c) and (d), (e) and (f) correspond to orientation angle II and III respectively.

The encoded signals and their cross-correlation signals along *x*-axis and *y*-axis are shown in figure 4.26 (a) and (b), figure 4.26 (c) and (d) as well as figure 4.26 (e) and (f) respectively. From figure 4.26 it can be seen that if orientation angle α is near to 45°, Encoded signals along x-axis and y-axis have narrow disparity in integer periods, otherwise have wide disparity in integer period.

4.4.5 Measurement speed experiment

With preset displacement of 2947.43nm, real-time displacements are measured by using cross-correlation filter and the real-time displacement measurement method introduced in this chapter when the scanning stage is driven at step spacing from single step voltage of 0.30538 mV up to 25 times of it. As soon as the measured displacement $S(n)$ is equal to or larger than the preset displacement, the measurement is stopped immediately. Each time the effective (RMS) amplitude of cross-correlation signal is calculated and the elapsed time t is recorded. The displacement measurement speed is calculated by $v = S(n) / t$.

The deviation of measured displacements away from preset displacement changing in winding ascent trend with the increase of measurement speed are plotted in figure 4.27 (a), and the RMS amplitudes of cross-correlation signal attenuating with the increase of measurement speed are plotted in figure 4.27 (b).

The robust speed for the displacement measurement of *x*-*y* piezoelectric scanning stage employed in this case is less than 2 μm/s if both the deviation and RMS amplitude are considered. Accordingly the step voltage to drive the scanning stage is less than 3 mV.

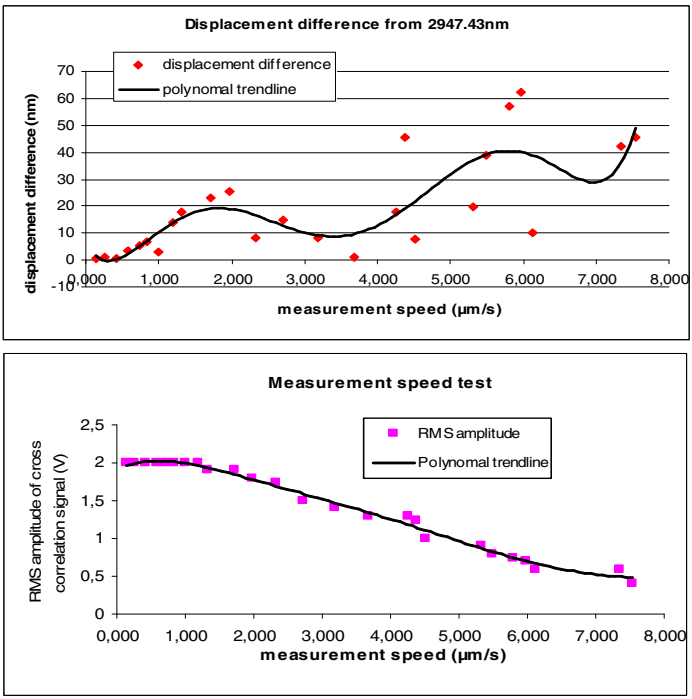

Figure 4.27 (a) Differences between measured displacement and preset displacement and (b) RMS amplitude of cross-correlation signal changes as a function of measurement speed.

4.4.6 Tests on other technical data

4.4.6.1 Repeatability and resolution in AEM

The repeatability of displacement measurement and control has been measured over various distances shown in figure 4.28. For each distance the scanning begins from the same starting point and is measured 6 times. The starting position is controlled by the built-in capacitance sensor with non-linearity less than 0.1%. The displacement has been measured by cantilever

and controlled by the capacitive senor of the scanning stage. The deviations between displacements obtained by cantilever and capacitive sensor together with the standard deviation as the function of preset displacements are shown in figure 4.28.

The repeatability of displacement measurement depends on the smallest step that can be translated by scanning stage driven by the voltage output from DAQ Unit. The DAQ unit has 16 bit analog outputs voltage within ±10 V. The x-y scanning stage that has been employed has a 100 µm stroke when the driving voltage is in the range of -2 V~12 V, so that the scanning step resolution is about 2.2 nm. Based on that resolution, the repeatability of displacement measurement over a distance of 70 µm is better than 2.2 nm. The deviation of displacement control is less than 2.5 nm. If the scanner has higher resolution, the displacement repeatability measured by TF cantilever will be better. Since the scan should stop as soon as the measured displacement (double precision data) is equal to or greater than the given displacement, standard deviations are all positive.

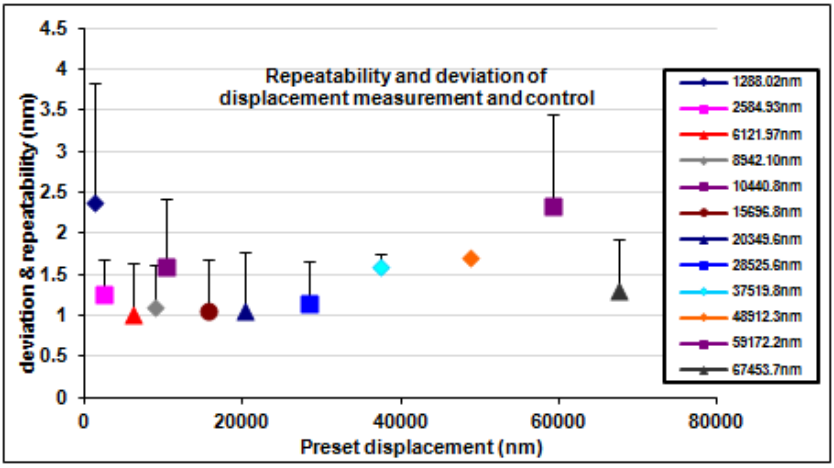

Figure 4.28 Repeatability and deviation results of the displacement measurements at different preset displacements.

4.4.6.2 Resolution in PEM

The real-time displacement measurement resolution of AFM cantilever encoded in AEM mode was decided by the smallest scanning step voltage output from DAQ unit that drives *x*-scanning stage to move, and also by the stroke of *x*- scanning stage. In 4.4.6.1, it is said that the resolution in AEM is 2.2nm based on single step voltage of 0.30538 mV output by DAQ unit and the maximum 100 μm stroke of *x*-scanning stage. If a measured micro scanning stage has only 10 μm or 1μm displacement range under 0~10 V voltage output from DAQ unit with 16 bit analogue voltage output, the smallest scanning step becomes 0.3 nm or 0.03nm.

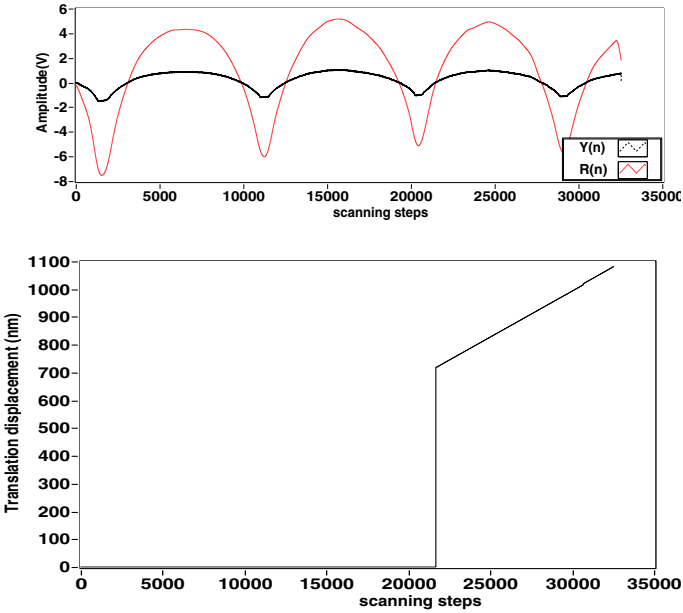

Figure 4.29 In PEM offline encoded signal and cross-correlation signal are shown in (a) and the displacement curve is shown in (b) when x scanning stage is driven by ramp voltage of 1mHz in frequency and 0.5Vpp in amplitude.

Because there was no smaller stroke scanning stage available, the smaller scanning step is expected to be achieved in PEM displacement measurement procedure. During *x* scanning stage is driven to move by independent signal generator with ramp voltage of 1 mHz in frequency and 0.5 Vpp in amplitude, the 1D sinusoidal grating of 300 nm in pitch is scanned by TF cantilever along the direction approximately perpendicular to the grating lines, and encoded signal is recorded. It has been shown in section 4.4.3 that real time displacement in PEM mode is measured in slowly decreasing speed when *x* scanning stage is independently driven by ramp voltage of very low frequency and very small voltage, the encoded signal data in one period are much fewer than that in the previous period. It is difficult to calculate the displacement resolution in PEM when the displacement is measured in real time, therefore the displacement resolution is calculated when the displacement is measured offline. (a)

The offline encoded signal and cross-correlation signal as well as the displacement curve are shown in figure 4.29 (a) and 4.29 (b) respectively. The offline displacement measurement results and resolution calculation result are listed in table 4.7 in detail. The resolution is 0.03 nm per step when the displacement is measured in PEM if the measured scanning stage is driven by ramp voltage of 1 mHz in frequency and 0.5 Vpp in amplitude.

Table 4.7 Resolution test in PEM with driven signal of 1mHz in frequency and 0.5 Vpp in amplitude.

Template samples	Steps count	Integer number	Measured displacement (nm)	Resolution (nm/step)
640	32547	4	1081.51	0.03

4.5 Discussions on direct decoding method

All the accuracy tests in figure 10 are based on following very good conditions:

(1) totally new and high resolution TF-AFM cantilevers (high Q-factor, small frequency difference $\Delta f < 200$Hz) are chosen, the parasitic capacitance of preamplifier circuit is compensated very well which means the amplitude-frequency curve is very symmetrical;
(2) template sample of cross-correlation filter is correctly chosen being

approximately equal to one half of the period of 1D grating encoded signal.

(3) tests are performed at ambient temperature of 21°C, and AFM cantilever encoder is covered by a shielding cover to avoid the influence of air flow.

In such good conditions, for example, to monitor the *x*-scanning stage moving to 2734.6 nm by TF cantilever paired with 1D sinusoidal grating of 300nm in pitch, real-time encoded signal has very high amplitude, good contrast between peaks and valleys and less noise in the signal as shown in figure 4.30 (a). Its cross-correlation signal shown in figure 4.30 (b) is obtained by cross correlating the encoded signal in figure 4.30 (a) with a half sinusoidal waveform template of 85 samples. When *x*-scanning stage moves to 1580 steps in single step voltage, it is stopped. The measurement results are 8 integer periods (2400 nm), two fractional parts in sum (335.29 nm) and measured displacement of 2735.29 nm. The displacement curve decoded from it shown in figure 4.30 (c) is increasing smoothly.

Nevertheless, if template samples are not chosen correctly, for the same signal, a half sinusoidal waveform template samples of 20 instead of 85, *x*-scanning stage is stopped after 818 steps. The encoded signal and cross-correlation signal shown in figure 4.31 (a) and 4.31 (b) respectively has actually 4 integer periods but in cross-correlation signal every small lump in the valleys are counted as integer period too, so that the integer period is also counted as 8 (2400 nm), two fractional part displacements in sum is 335.263 nm and total measured displacement amounts to 2736.26 nm. The displacement curve shown in figure 4.31 (c) is increasing bumpily. Those bumps are the local nonlinear error. The reason is analyzed in the next subsection.

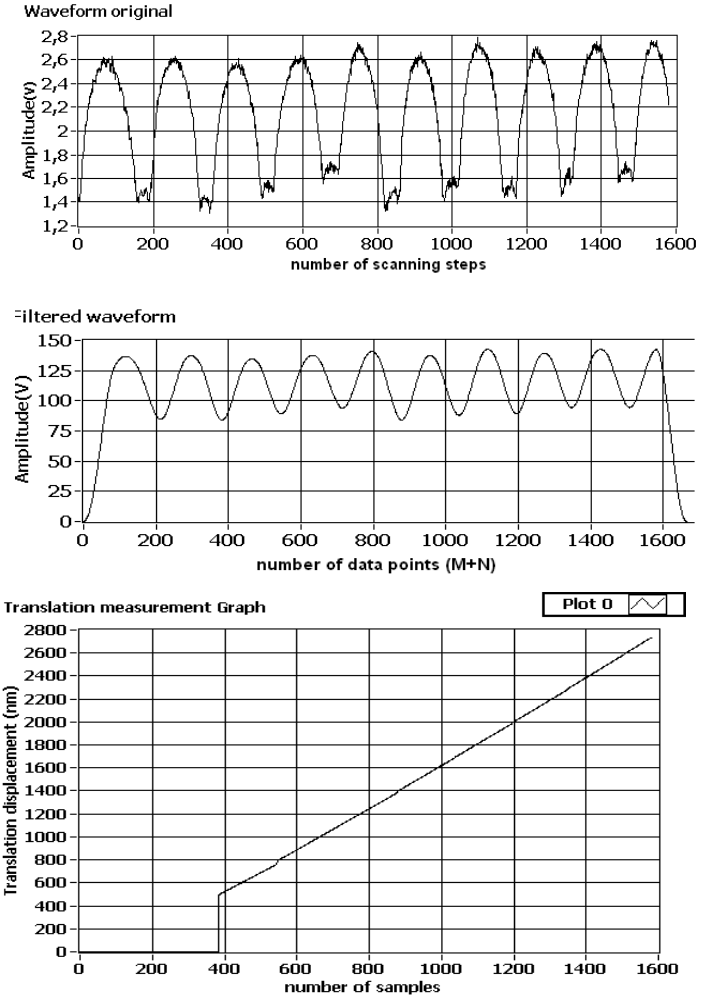

Figure 4.30 For good encoded signal (a) and cross-correlation signal (b) with correct template, displacement curve is smoothly increasing like (c).

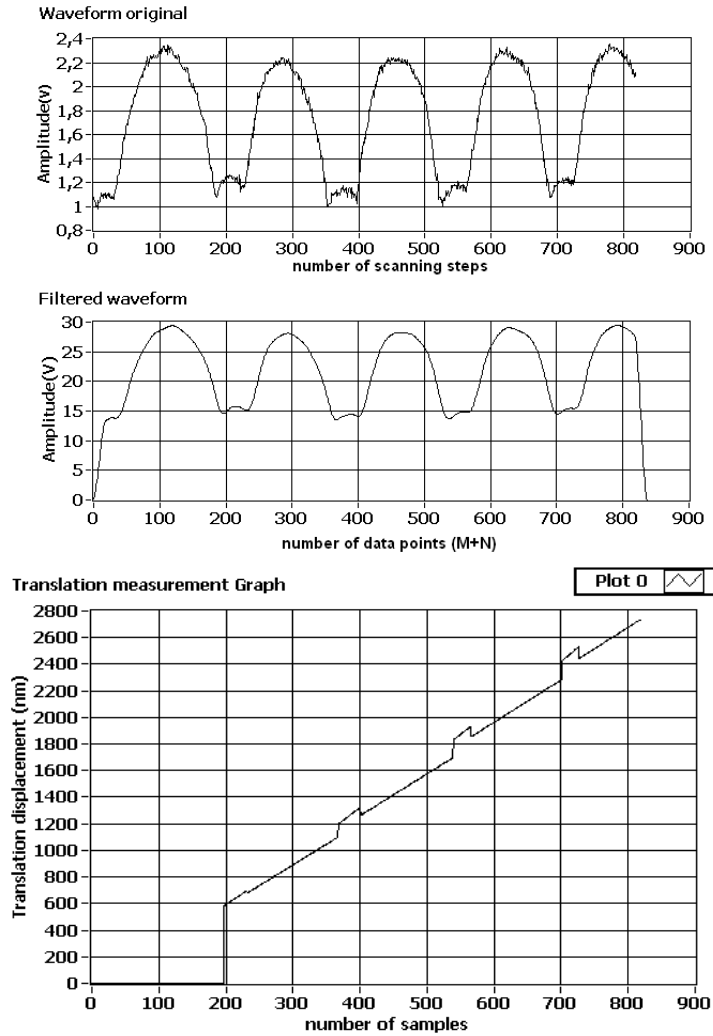

Figure 4.31 For good encoded signal (a) and cross-correlation signals (b) with incorrect template, displacement curve is increasing bumpily.

4.5.1 Local nonlinear displacement measurement error

For direct decoding of encoded signal by counting integer periods plus calculating fractional parts, the calculations of fractional part *fs* at the beginning and fractional part *fe* at the end need the first and the last integer pitch as reference. For direct decoding of encoded signal, let's consider the signal from integer period *I*(*i*) to period *I*(*i*+1) in figure 4.35. When AFM cantilever scans from step *M*(*i*) to step *M*(*i*+*fe*), the displacement will be

$$S_{i+fe} = [fs + I(i) + \frac{M(i+fe) - M(i)}{M(i) - M(i-1)}] \cdot P \tag{4-29}$$

When AFM cantilever scans to step *M* (*i*+1) , *fe*=1. If *fe*=1 is put into equation (1) and (2), they will become

$$S_{i+1} = [fs + I(i) + 1] \cdot P \tag{4-30}$$

$$S_{i+1} = [fs + I(i) + \frac{M(i+1) - M(i)}{M(i) - M(i-1)}] \cdot P \tag{4-31}$$

In equation (4-31), if $M(i+1) - M(i) = M(i) - M(i-1)$, which means scanning steps in period *I*(*i*) equal to that in period *I*(*i*+1), from step *M*(*i*) to step *M*(i+1), the displacement curve will be continuous line. If in equation (4-31) $M(i+1) - M(i) \neq M(i) - M(i-1)$, which means scanning steps in period *I*(*i*) unequal to that in period *I*(*i*+1), at step *M*(*i*) the displacement curve will be discontinuous at this point. If $M(i+1) - M(i) < M(i) - M(i-1)$, it will have a sudden jump as shown in figure 4.32 (a). Otherwise it will have a sudden drop as shown in figure 4.32 (b).

If one period of 1D grating encoded signal is not approximately equal to the previous and the next, this will result in local nonlinear displacement measurement error, which occurs within one pitch length of the displacement, it is not accumulated to the last scanning step of displacement, although it differs from one period to another period of cross-correlation signals.

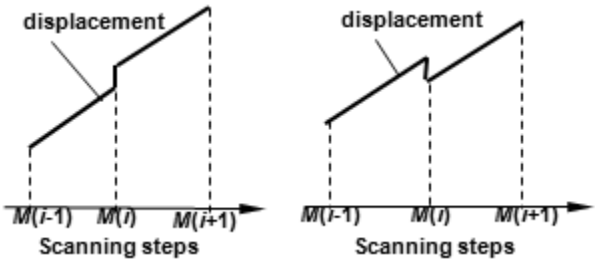

Figure 4.32 displacement corresponding to number of scanning steps: (a) when M(i+1) - M(i) < $M(i)$ - M(i-1); (b) $M(i$+1) - $M(i)$ > $M(i)$ - $M(i$-1).

4.5.2 Others reasons

Beside incorrect template samples, there are several other reasons found in the investigation which can cause local nonlinear displacement errors.

(1) If in AEM mode scanning step voltage is increasingly changing as shown in figure 4.33 (a), the displacement curve is rising in step form as shown in figure 4.33 (b).

(2) If displacement is measured in PEM mode: when the measured micro-moving stage is controlled individually by other voltage sources or signal generator to move at a reasonable speed, for example at 1 mHz frequency and 1 V peak-peak amplitude ramp voltage, real-time displacement is measured in a little different measuring speed, usually fast at beginning and slow gradually, so that the encoded signal is like that in figure 4.33 (a) and the displacement curve is basically smooth shown in figure 4.34 (a). However when it moves at very slow speed, for example at 1 mHz frequency and 0.5 V peak-peak amplitude ramp voltage, real-time displacement is measured in quite different measuring speed, usually faster at beginning and slower gradually, so that the encoded signal is much like that in figure 4.31 (a) and the displacement curve is rising in step form as shown in figure 4.34 (b)
(3) If cantilever has been used over long time so that encoded signal becomes noisy and the period of encoded signal fluctuates from one to another as shown in figure 4.35 (a), displacement curve is bumpy too as shown in figure 4.35 (b).

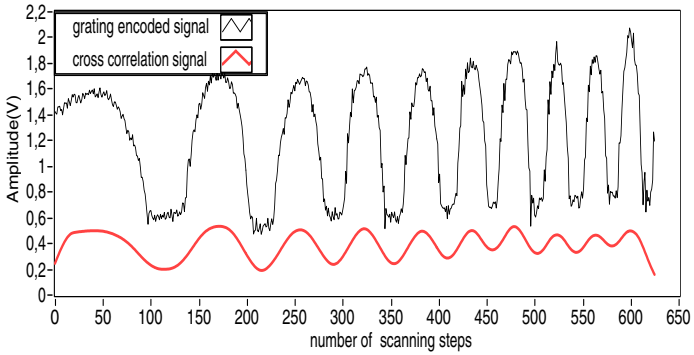

(a)

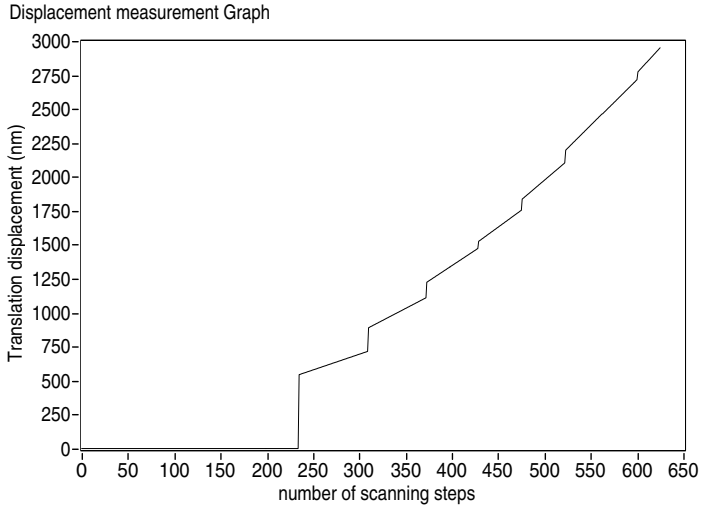

(b)

Figure 4.33 (a) Changing speed produces unequal periods of 1D sinusoidal grating position-encoded signal; (b) it causes displacement curve discontinuous and bumpy.

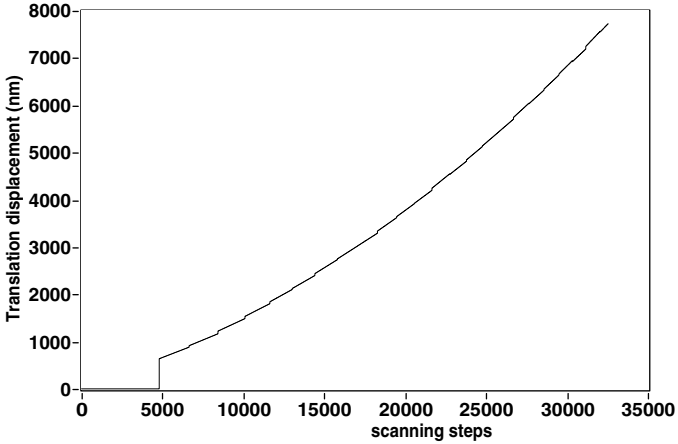

(a)

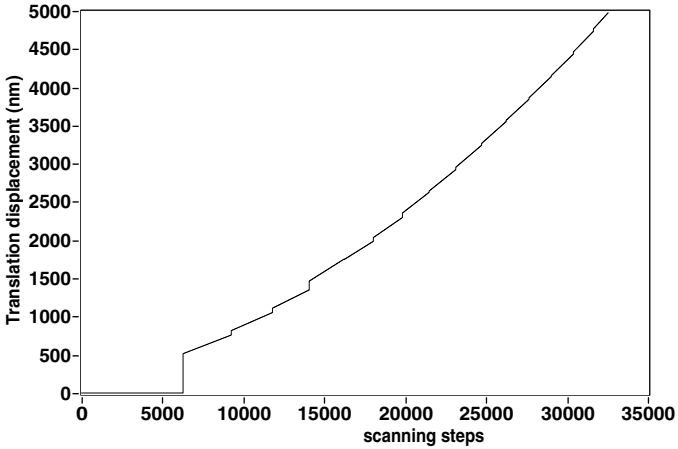

(b)

Figure 4.34 Displacement is measured in PEM with independent ramp driving voltage of (a) 1V peak-peak amplitude and 1mHz frequency and (b) 0.5V peak-peak amplitude and 1mHz frequency.

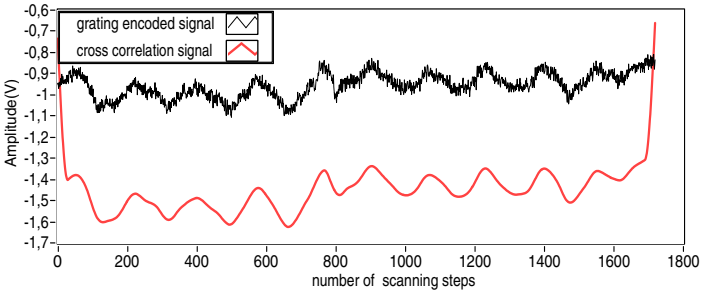

(a)

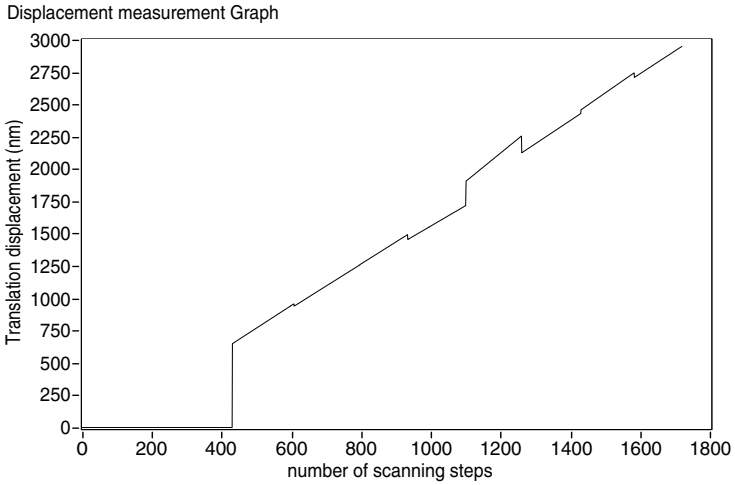

(b)

Figure 4.35 Worn cantilevers produces noisy and unequal periods of 1D sinusoidal grating position-encoded signal and cross-correlation signal in (a), which causes displacement curve not continuous but bumpy in (b).

4.6 Summary

It has been demonstrated in this chapter that one AFM cantilever can be used as an encoder to measure one directional displacement in AEM and PEM. The algorithm used to decode the encoded signal into the displacement is

based on the direct count of the integer pitches of 1D grating plus the calculation of the fractional parts of a pitch at the beginning and at the real-time or end position. A cross-correlation technique has been adopted and applied to the real-time signal filtering process for the determination of the pitch during scanning by using a half sinusoidal waveform template. For the first investigation, a 1D sinusoidal grating with the pitch of 300 nm and 2D rectangular gratings with the pitches of 80 nm, 100 nm, 120 nm, 160 nm and 200 nm are used.

One AFM cantilever as an encoder can be used to monitor the scanning stage to be controlled to move to a given displacement in open-loop and closed-loop by its own built-in capacitance sensors. Based on this advantage, several applications have been found, experimented and analyzed, such as hysteresis of piezoelectric scanning stage, In-plane small tilt angle and in-plane rotation angle between 1D grating orientation and micro-moving stage within 90° range. Another promising application should be the in-situ calibration to the built-in capacitance sensors of micro-moving stage.

When the motion of a scanning stage is controlled with a resolution of 2.2 nm, the measurement repeatability in AEM is better than 2.2 nm for a displacement of 70 µm. When the motion of a scanning stage moves in certain speed controlled by an independent voltage source, so called PEM, if the voltage rising with time in certain extent, the real-time displacement can also be precisely measured. When a scanning stage is controlled to move by an independent voltage source at the resolution of 0.03 nm per step, the displacement can be measured too regardless of the local nonlinear measurement error. The robust measurement speed is 2 µm/s.

AFM cantilever as an encoder for the displacement measurement and control is similar to optical encoder if it comes to the grating line encoding technique: metrologically both take grating or line-scale structure as a reference to be paired with them. If TF cantilever works in intermittent contact FM mode, usually one cantilever can be used for a long time in ambient conditions as other non-contact and intermittent contact cantilevers do.

One AFM cantilever as an encoder for one directional displacement measurement to a large extent does not rely on the waveform and quality of the 1D grating. For example, 1D sinusoidal, 1D rectangular, and 1D triangular or 1D trapezoidal grating all can be used as the reference. The

pitch of the grating can be much smaller than 80 nm. It is expected from the results that the uniformity of the grating structure in height will have a small effect on the displacement calculation due to the cross-correlation filtering. However in order to avoid local nonlinear error, one AFM cantilever as encoder is not suitable to monitor the micro-moving stage position change by real-time measuring the displacement in PEM when the measured micro-moving stage moves too slowly; also it is not suitable to measure the displacement of micro-moving stage when it moves in changing speed; and it is not suitable to measure two directional (forward and backward) displacements, because it cannot distinguish the direction. The AFM cantilever should be changed in time when it has been used for long time so that the signal to noise ratio of the encoded signal won't drop dramatically.

5 AFM head with multi TF cantilevers

5.1 Introduction

It has been demonstrated in chapter 4 that an AFM cantilever can be used as an encoder to measure one directional displacement and to control the scanning stage to move to a given displacement based on direct displacement decoding method, and by using a cross-correlation template of a half sinusoidal waveform to real-time process 1D grating position-encoded signal scanned by TF cantilever, the motion of a scanning stage has been controlled with a resolution of 2.2 nm up to 70 μm.

However, in order to decide between forward and backward movement, one additional signal is necessary. It might be obtained by a second cantilever, which means under certain conditions two TF cantilevers can realize two direction displacement measurements. For example, two such sinusoidal grating encoded signals are employed and each signal is individually picked up by one AFM cantilever and if there is a phase shift of 90° between them in ideal case, an optimistic quadrature phase procedure - well known in interferometry - might be used, forward and backward displacements can be measured. The reason for that has been explained by the decoding principles in chapter 2. The multi TF cantilevers AFM will be introduced in this chapter. Two AFM cantilevers as encoder and the computer algorithm will be discussed and the experiments are described in the next chapter.

5.2 AFM head with multi TF cantilevers

If two AFM cantilevers are needed for forward and backward displacement measurements in *x*-axis, another two cantilevers are necessary for forward and backward displacement measurements in *y*-axis too. Since available nanoscale grating of small pitch that could be used as the reference to pair with AFM cantilevers encoder are usually fabricated within small area, four AFM cantilevers should be mechanically integrated into one compact encoder head, so that the surface area formed by four cantilever tips is as small as possible when compared with that of 1D grating surface area. Although self-sensing and self-stimulating TF cantilever for the compactness becomes the favorite device compared to other cantilevers that either needs bulky optical detection unit or other detection methods, every cantilever tip in

the compact encoder head still needs to approach the surface and to follow the tilt and topography of the grating surface on its own. Therefore in the first approach, three TF cantilever tips are purposefully designed and developed.

Three cantilever tips 1, 2 and 3 are designed and arranged to constitute one equilateral plane triangle (tips triangle) with circumscribed circle diameter of d (mm) as shown in Figure 5.1(a). 1D sinusoidal grating is intentionally rotated at an angle α between grating lines and x-axis in x-y plane. Angle α can be measured by using one cantilever decoding method in section 4.4.4.3. If cantilever 1 is assumed to be fixed, and cantilever 2 and 3 can be controlled to slightly move forwards and backwards so that the tips distances between cantilever 1 and 2 in y-axis and cantilever 1 and 3 in x-axis are equal to $(N2+1/4)\cdot P\cdot\cos\alpha$ and $(N1+1/4)\cdot P\cdot\sin\alpha$ respectively, cantilever 1 and 3 can be used for displacement measurement in x-axis and cantilever 1 and 2 will be used for displacement measurement in y-axis. Here P is the pitch of 1D sinusoidal grating, where $N1$ and $N2$ are the positive integer numbers.

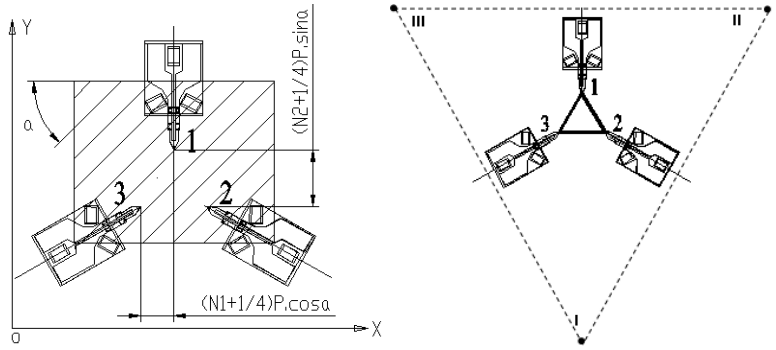

(a) (b)

Figure 5.1 (a) Schematic illustration of geometrical relationship between three TF cantilevers 1, 2 and 3 and (b) their geometric relationships with three support points I, II and III.

The central points of I, II and III which are in correspondence with three supporting points of approach and adjustment device have to be designed and arranged to constitute another equilateral plane triangle (props triangle) with circumscribed circle diameter of D (mm). Three micro step motors are used for approach and adjustment. Geometric position relationship between two

equilateral triangles is illustrated in figure 5.1(b). The positions of three tuning-fork AFM cantilevers are controlled during approach and adjustment to their set-points by AFM feedback control electronics which consists of preamplifier, self oscillation and PLL circuit, PI-controller and HV source. Approximately 0 V at the output of the PLL circuit is chosen as set-point for the cantilevers. When all three tuning-fork cantilevers have approached the set-points, the tips triangle basically should be parallel to 1D grating surface in the ideal case. If one of the cantilevers first comes to the set-point, it must be lifted up by two related micro step motors. For example, cantilever 1, 2 and 3 should be individually lifted up by micro step motor 2 and 3, micro step motor 1 and 2 and micro step motor 1 and 3, respectively. Afterwards the encoder head could be further lowered by three micro step motors consecutively in turn. The approach process repeats until all three cantilevers are coming to their own set-points. Because the props triangle is D/d times larger than the tips triangle, and slight tilt of the tips triangle relative to the 1D grating surface may result in one of three micro step motors raising to its maximum stroke limit and another of them may dropping to its minimum stroke limit. Therefore D should be as small as possible. According to the layout in figure 5.1(b), the AFM with three TF cantilevers is developed as shown in figure 5.2.

On the encoder head in figure 5.2 (a) there are three equal-angularly machined V-shape slots I, II and III which are used as the support points, so that the encoder head can be propped up by three micro step motor screw rods. Subjected to mechanical structural constraints, the supporting points of I, II and III make up an equilateral plane triangle with circumscribed circle diameter of ϕ = 90 mm. Three picomotor™ actuators (Model 8302 of Newport Corporation) are installed in the approach and adjustment device, so-called the picomotor framework shown in figure 5.2 (c). The picomotor™ actuators can be step-driven by driver kit (Model 8763-KIT) individually or consecutively in turn at the same or different steps. The driver kit is connected to computer through RS-232 bus and is automatically controlled by software to move to the desired position at certain pulse rate. Minimum incremental motion of 30nm/pulse and maximum incremental motion speed of 1.2 mm/min at 2000 kHz pulse rate are possible. The picomotor™ actuators, the sample holder together with a 100 µm × 100 µm x-y piezoelectric scanning stage (P-621.2CD of Physik Instrumente GmbH) are built inside the picomotor™ framework,. The scanning stage is used as micro displacement stage moving in open-loop as well as closed-loop mode,

whereby the position is controlled by internal capacitance sensors. When the encoder head is turned upside down and put onto the picomotor™ framework the whole mechanical device is shown in figure 5.2 (d).

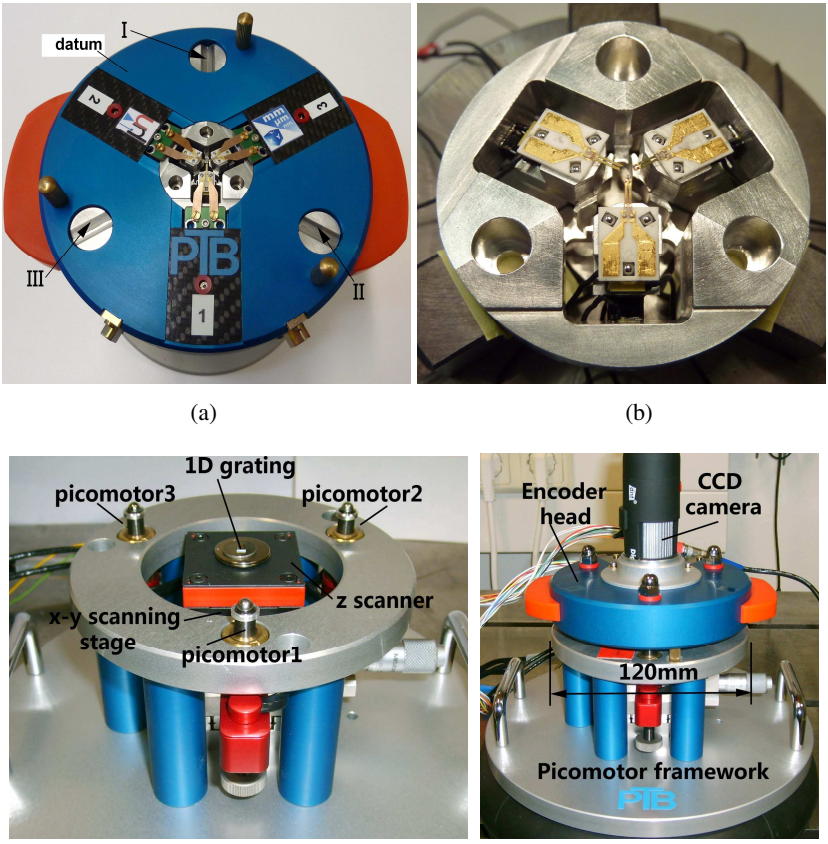

(a) (b)

(c) (d)

Figure 5.2 AFM with three TF cantilevers is shown in (d), where AFM head of three cantilevers is shown in (a), mechanical arrangement of cantilevers and their holders is shown in (b), approach & adjustment framework is detailed in (c).

The electronics and control unit schematic of three cantilevers TF-AFM is shown in figure 5.3, where the operation and control process of one of three

TF cantilevers is depicted in detail in electronics and control unit 1. A *z*-fine piezo is controlled to extend or contract by a high voltage controller (HV source), and the phase piezo is controlled to lengthen or shorten by another high voltage controller called tip phase HV source. Optionally, phase piezo can also be controlled by a tuneable direct current (DC) voltage source.

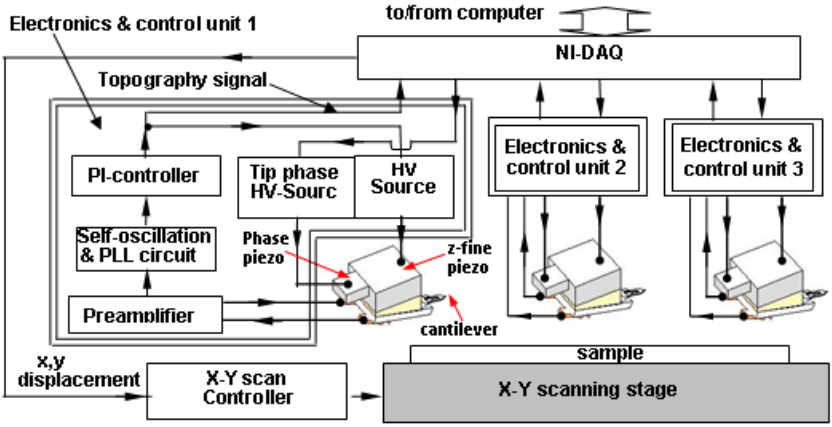

Figure 5.3 Schematic of AFM with three TF cantilevers as well as electronics and control units.

By the electronics unit, TF cantilever is oscillated at resonant frequency f_0. The frequency will change as the cantilever tip approaches 1D grating surface as well as retracts from it. The change of frequency is detected by a self-oscillation & PLL circuit and converted to DC voltage at its output port. Then the PLL voltage is amplified by PI-controller and HV source which on one side is used to feedback-control the *z*-fine piezo to extend or contract, and on the other side is acquired by computer through NI-DAQ as topography signal which actually is 1D grating position-encoded signal. During scanning, a small DC offset voltage is used as a set point, i.e. the sample surface is scanned at a constant frequency shift.

5.3 Experiments and results of AFM with two TF cantilevers

One TF cantilever and the AFM control loop in figure 5.3 can be extracted from the system as shown in figure 5.4. Compared with that of one cantilever TF-AFM shown by figure 3.2 in chapter 3, the configurations are the same, especially the preamplifier and self-oscillation & PLL circuit, except for the settings of PI-controller, HV source and the specifications of *z*-fine piezo. Nevertheless, those three modules are the decisive factors of the AFM performance and characteristic. The setting of the AFM control loop will be discussed in the following subsections.

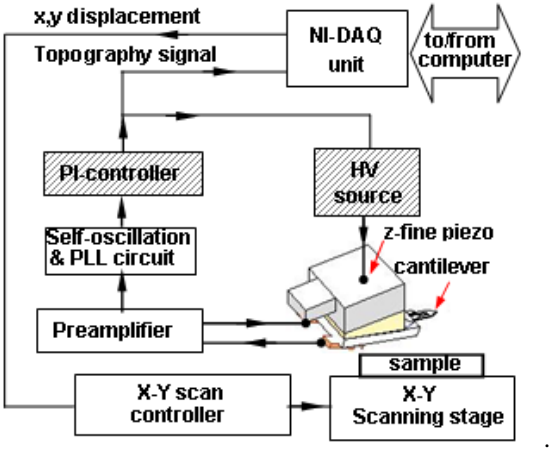

Figure 5.4 Schematic of one of three TF cantilevers and its control unit

5.3.1 TF cantilevers noise level

Since TF cantilever itself and its electronics do not change, the noise remains the same as that of one cantilever TF-AFM which are 14.82 mV (1.5 nm) and 34.38 mV (3.5 nm) respectively when TF cantilever is oscillating in free space and in periodic contact with sample.

5.3.2 Sensitivity of TF cantilevers

Each TF cantilever has its own specifications: resonant frequency f_O, Q-factor, approximate capacitance (pF) and maximum frequency shift Δf_{max} etc which are the intrinsic characteristics for one cantilever. Δf_{max} and sensitivity can be calculated from approach curve. Sensitivity is defined as the maximum frequency shift divided by the amount of tip displacement in the periodic contact region. Nevertheless according to the reference [42], the maximum frequency shift Δf_{max} does not depend on the tip vibration amplitude, although the sensitivity differs for each setting of the tip vibration amplitude, which is increased as the tip vibration amplitude is decreased. Tip vibration amplitude can be manually tuneable before cantilever tip does scan. Therefore each TF cantilever already has its own sensitivity after stabilized sinusoidal self-oscillation signals with 90° phase shift have been gained. It is explained by conducting the experiments on the following parameters.

5.3.2.1 Sensitivity of z-fine piezo

Different from z-scanner which has 9 μm stroke under ±40 V voltage applied by its HV source in one cantilever TF-AFM introduced in chapter 3, z-fine piezo has only 1.2 μm stroke under 0 ~ 120 V voltage applied by its HV source in the three cantilevers TF-AFM shown in figure 5.3. Therefore the voltage sensitivity is 100 nm/V for the z-scanner and only 10 nm/V for the z-fine piezo.

5.3.2.2 Gains of PI controller and HV source

Gain of PI controllers can be continuously tunable approximately from 0 to 8. However it is set much smaller than before. The reason will be explained in the late subsection. There are several gain shifts on the front panel of HV source; three of them are more often used. They are HV10, HV20 and HV40 which all can be continuously tuned to a voltage in the range from 0 to 120 V but have different gain. When the gain of PI controller is set rationally, it is measured by a voltmeter, while HV source at shift HV10, HV20 and HV40 are measured when the PLL output voltage is set from 0 to 10 V. Measured data are drawn in graph and shown in figure 5.5.

The calculated gains are listed in table 5.1, where gain denotes individual gain of PI controller, HV10, HV20 and HV40, while combined gain includes PI gain and HV source gain together, which can be expressed as $K_i = k_i \times k_{PI}$ (i=10, 20 and 40).

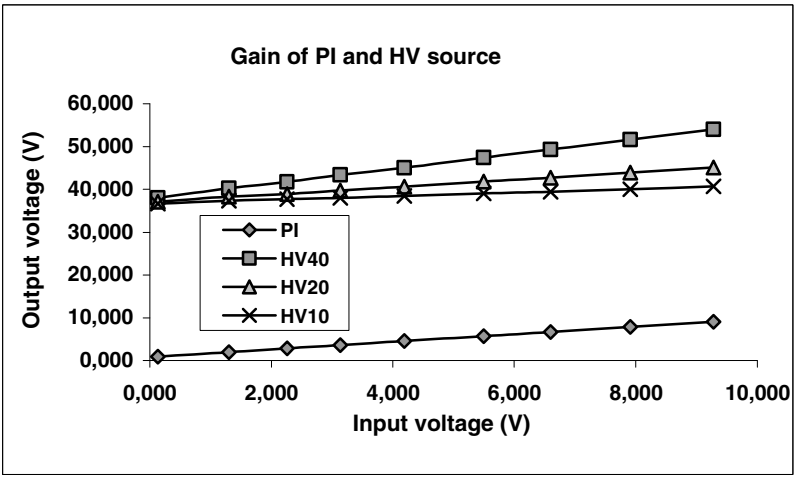

Figure 5.5 Gain measurement results of PI controller and shifts HV10, HV20 and HV 40 of HV source.

Table 5.1 Gain measurement results

Descriptions	PI	HV10	HV20	HV40
Gain	$k_{PI} = 0.89$	$k_{10} = 0.48$	$k_{20} = 0.96$	$k_{40} = 1.95$
Combined gain		$K_{10} = 0.43$	$K_{20} = 0.85$	$K_{40} = 1.73$

5.3.2.3 Approach curve and sensitivities

The approach curve has been tested. The procedure is as simple as that of one cantilever TF-AFM stated in subsection of 3.3.2.3.

(1) set gain of HV source to HV40 shift ($k_{40} = 1.95$, see table 5.1), tune the voltage to a preset value of 30 V ~ 50 V by observing the voltage change in the digital voltage indicator on the front panel,

which means z-fine piezo extends nearly to a half of its maximum stroke. Then let TF cantilever AFM work as usual as configured in figure 5.3, let cantilever tip approach the 1D grating surface to such a position that the PLL voltage drops from 1 V offset approximately to 0 and HV source voltage displayed in the indicator also drops by a factor of k_{40}, therefore the distance between cantilever tip and sample is in the periodical contact region;

(2) disconnect the cable between PI controller output and HV source input, and the connect oscilloscope to PLL output as shown in figure 5.6;

(3) manually tune the HV source voltage from 0 to 100 V to make the z-fine piezo from the half of its maximum stroke contract to the zero stroke and then extend to its maximum stroke, which makes the cantilever tip relative to the sample change from its oscillating at resonant frequency in free space to its oscillating at higher frequency in the contact with sample. In this procedure however, the PLL voltage changes from high to low. Each tuned HV source voltage and each pair of PLL voltage and frequency value can be taken down.

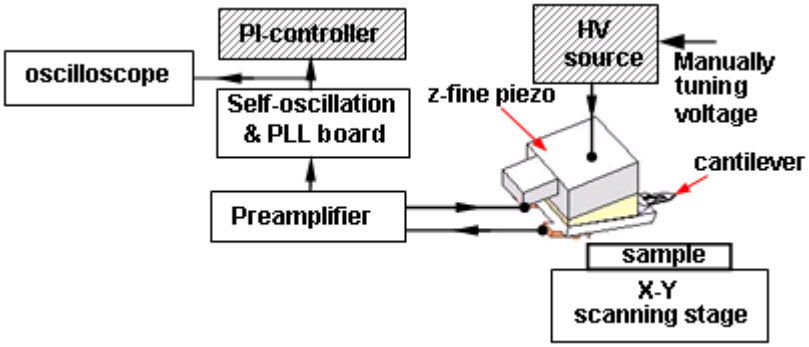

Figure 5.6 Schematic of experiment on approach curve.

The PLL voltage changes from high level V_{PLLH} to low level V_{PLLL} and correspondingly cantilever working frequency changes from low frequency f_L to high frequency f_H. If the low level amplitude and high level amplitude in HV source is tuned further, lower and higher respectively, it is found that V_{PLLH}, V_{PLLL}, f_L and f_H do not change anymore, which means TF cantilever

frequency shift already has already come to its maximum. Therefore from contraction to extension, the effective voltage V_{HVeff} applied to *z*-fine piezo which contributes to the maximum frequency shift should be the voltages in a range that make the frequency linearly increase or decrease.

Since it has already been known that the sensitivity of z-piezoelectric scanner is 10 nm/V, the effective stroke L_{eff} of *z*-piezoelectric scanner should be

$$L_{eff} = V_{HVeff} \times 10 \text{ (nm)} \tag{5-1}$$

Thus the sensitivity of TF cantilever AFM can be calculated as

$$S_{TF} = (f_H - f_L) / L_{eff} \text{ (Hz/nm)} \tag{5-1}$$

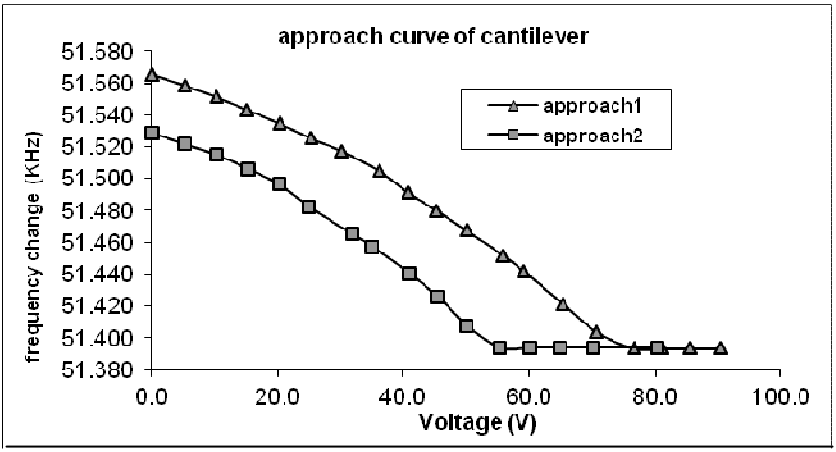

Figure 5.7 Approach curve for one TF cantilever with two different preset voltages which is 65 V and 40.7 V for approach 1 and approach 2 respectively.

Two approach curves of one typical TF cantilever are drawn together in figure 5.7, where two preset voltages are 65 V for approach 1 and 40.7 V for approach 2. Figure 5.8(a) is the approach curve of one TF cantilever while figure 5.8 (b) is the approach curve of another TF AFM cantilever. The related data directly measured in figure 5.7 and 5.8 or derived by using equation (5-1) and (5-2) are listed in table 5.2. It can be seen from the data in table 5.2 that the cantilever with low Q-factor and large frequency shift is more sensitive than that with high Q-factor and small frequency shift.

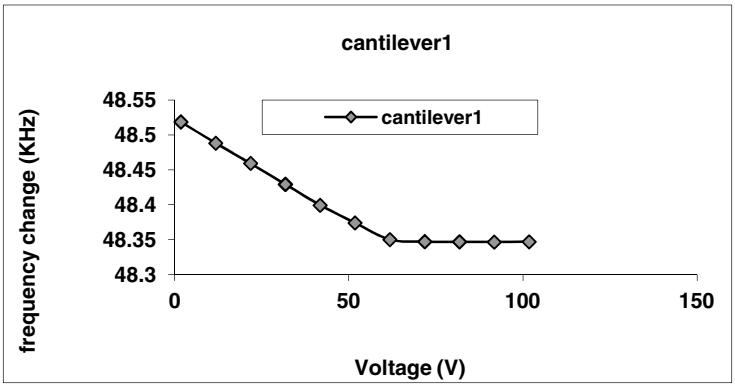

(a)

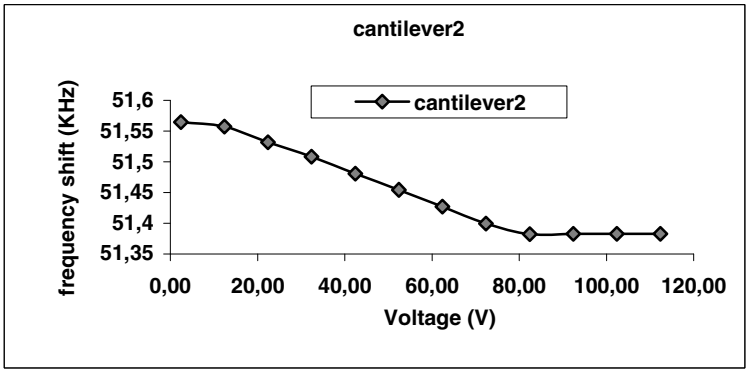

(b)

Figure 5.8 Approach curves of two cantilevers with the similar Q-factor and frequency shift Δf, where (a) for cantilever 1 and (b) for cantilever 2.

Table 5.2 Cantilever sensitivity experiment results

	Frequency(kHz)		Δf	V_{HVeff}	L_{eff}	Sensitivity
	Low f_L	High f_H	(Hz)	(V)	(nm)	S_{TF} (Hz/nm)
Approach 1	51,4036	51,5657	126.1	70.8	708	0.18
Approach 2	51,4076	51,5291	121.5	50.1	501	0.24
Cantilever 1	41.35	41.5184	168.5	60	600	0.28
Cantilever 2	51,3994	51,557	157.6	60	600	0.26

5.3.3 Experiments on setting the optimum scanning parameters

Scanning parameters include set-point, offset PLL voltage, PI gain and the voltage range of HV source etc. The experiments are conducted to get optimum scanning parameters.

5.3.3.1 Gains of PI controller and voltage range of HV source

Since HV source is ground reference source which is tunable from 0 to 120 V, its output voltage should be preset to the middle of its full range, for example, 50 V, to make the *z*-fine piezo extend to the middle of its full stroke if PLL offset voltage is 1 V. Based on this extension, if combined gain of HV source and PI controller is K_i (i=10, 20 and 40), HV source output voltage is (50-K_i×1) V when cantilever comes to the set-point where the tip periodically contacts with sample and PLL voltage drops to zero. Because the multi cantilevers TF-AFM has a resolution of 10 nm/V, to encode 300 nm 1D sinusoidal grating with 80 nm in amplitude, the HV source output voltage should change ±8 V relative to (50-K_i×1) V to keep the cantilevers following the topography of the grating. During scanning along the sample, cantilever tip continuously from the previous set-point comes to the present point. When coming to the present point, the cantilever needs to approach the set-point. Suppose at present point PLL voltage drops from 0 to the negative, frequency decreases relative to the resonant frequency, which means that the gap between the tip and the sample tends to be enlarged and z-fine piezo should extend to narrow the gap. If K_i is set too large, the z-fine piezo extends considerably, and the distance between tip and sample suddenly becomes too smaller than before, so that cantilever tip from in periodical contact with the sample comes to in contact with the sample or even cantilever tip is broken by the sample's bumping. If K_i is set too small, the *z*-fine piezo extends little, the distance between tip and sample suddenly becomes larger than that at the previous set-point instead, so that the tip from in contact with sample comes to free space. K_i is the combined gain of PI controller k_{PI} and HV source k_i. Because the choice of k_i of HV source is already decided in advance by the roughness amplitude of the sample, correct setting k_{PI} of PI controller can keep the synchronization between cantilever tip and z-fine piezo in step. Gain measurement results in table 5.1 are already based on the correct setting of k_{PI}.

The cantilever tip and z-fine piezo should synchronize not only in steps, but also in speed. Because capacitance of z-scanner in one cantilever TF-AFM is 26 nF while capacitance of z-fine piezos in three cantilevers TF-AFM is 39 nF, which means it will take more time for the latter than for the former to extend or contract to a certain stroke, and time constant $\tau=RC$ of integral part of the PI controller should be set larger for latter than for the former.

The schematic of PI controller is drawn in figure 5.9. PLL output voltage $\delta(t)$ is amplified by the proportional part and integral part of PI controller, which are $Gp\cdot\delta(t)$ and $Gi\cdot\int\delta(t)\,dt$, where Gp and Gi are the gains of proportional part and integral part respectively, and $Gi=1/\tau$. then proportional part and Integral part are added by a summing amplifier, and last amplified by a high voltage amplifier (HVA) and input into HV source to drive the z-fine piezo to extend or contract, proportional part, integral part and HVA are all adjustable. Based on the circuit analysis and practical experiments, it is found that the most substantial measures to reduce K_i are firstly to reduce the gain of HVA by tuning it down, and secondly to increase time constant τ by increasing present values of R and C or to decrease the gain Gi of integral part by dividing the output voltage of it. Finally a trimmed resistor is soldered to divide the output voltage of the integral part, as shown in figure 5.11. The voltage curve at point ① is indicated with ①, while the voltage curve at point ② and point ③ are indicated with ② and ③, where dashed line and solid line are the voltage curves before and after the trimmed resistor is soldered respectively. This also is the reason why the gains in table 5.1 are all smaller values.

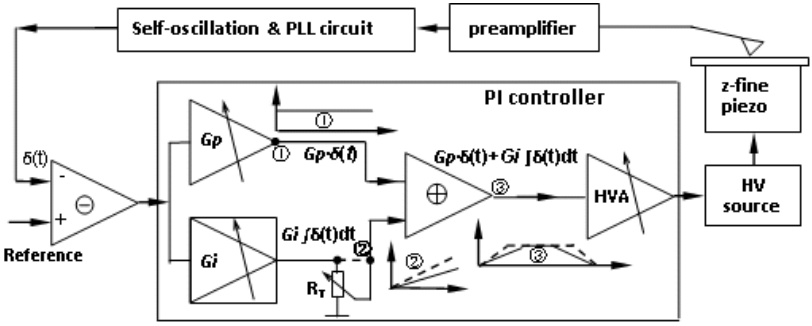

Figure 5.9 Schematic of PI controller for AFM with three TV cantilevers.

5.3.3.2 Set-point and PLL voltage offset

In scanning, set-point is the voltage V_{set} which is maintained by AFM control loop to make the TF cantilever oscillate at constant amplitude of a certain value. Zero voltage (V_{set}=0 V) of PLL is chosen as the best set-point. PLL voltage offset V_{offset} is the offset of frequency f which differs from resonant frequency f_O of cantilever at free space as illustrated in amplitude-frequency curve in figure 3.12. If V_{offset} is set too high, Δf is bigger, which means the tip vibration amplitude is smaller when the tip comes to the set-point. Usually Δf is chosen (10~20) Hz, which means V_{offset} is set about (0.5 ~1) V just as one TF cantilever AFM does. Usually the gain of integral part in PI controller is set as large as possible, so that the AFM control loop is more sensitive, and the tip scans better along the sample surface.

Since the gain of PI controller, especially integral part is rated amount, the topographies of 1D sinusoidal grating of 300 nm in pitch scanned by the TF-AFM at different set-points vary apparently as shown in figure 5.10 (a), 5.10 (b), 5.10 (c) and 5.10 (d).

5.4 Performance of AFM with two TF cantilevers

The 1D sinusoidal grating of 300 nm in pitch is scanned by two cantilevers. The grating position encoded signals and scanned image are shown in figure 5.11 (a), 5.11 (b), 5.11 (c) and 5.11 (d) respectively. Image resolution is chosen 256 pixels and scanning area is about 2.5 μm × 2.5 μm. In most cases, the set-points and the amplitudes of two encoded signals are different as shown in figure 5.11 (a) and 5.11 (b) because two TF cantilevers are intrinsically different in maximum frequency shift Δf and Q factor which result in the different sensitivity, additionally their PI controllers have not exactly the same gains . Therefore with the signals like figure 5.11 (a) the one image will be bright and another image will be dark. With the signals like figure 5.11 (b), one image is strong and another image is week in contrast. Only if two TF cantilevers nearly have the same values in maximum frequency shift Δf and Q factor, which means the sensitivity will have a little difference as shown in figure 5.11 (c), the scanned images are comparable in contrast and brightness as shown in figure5.12.

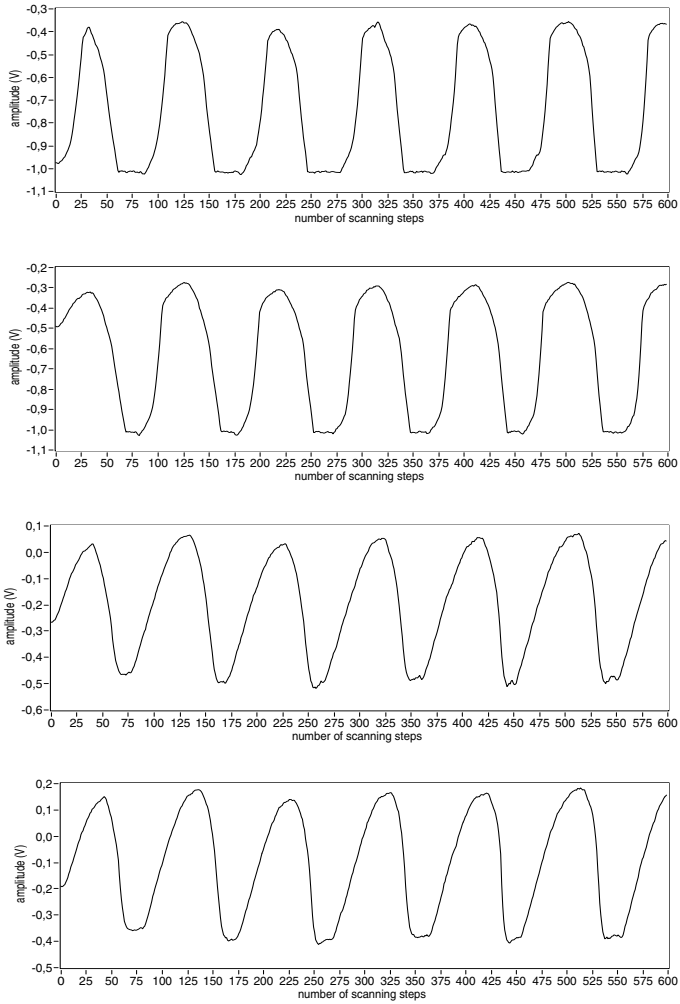

Figure 5.10 Topographies of 1D sinusoidal grating of 300 nm in pitch scanned at different set-points.

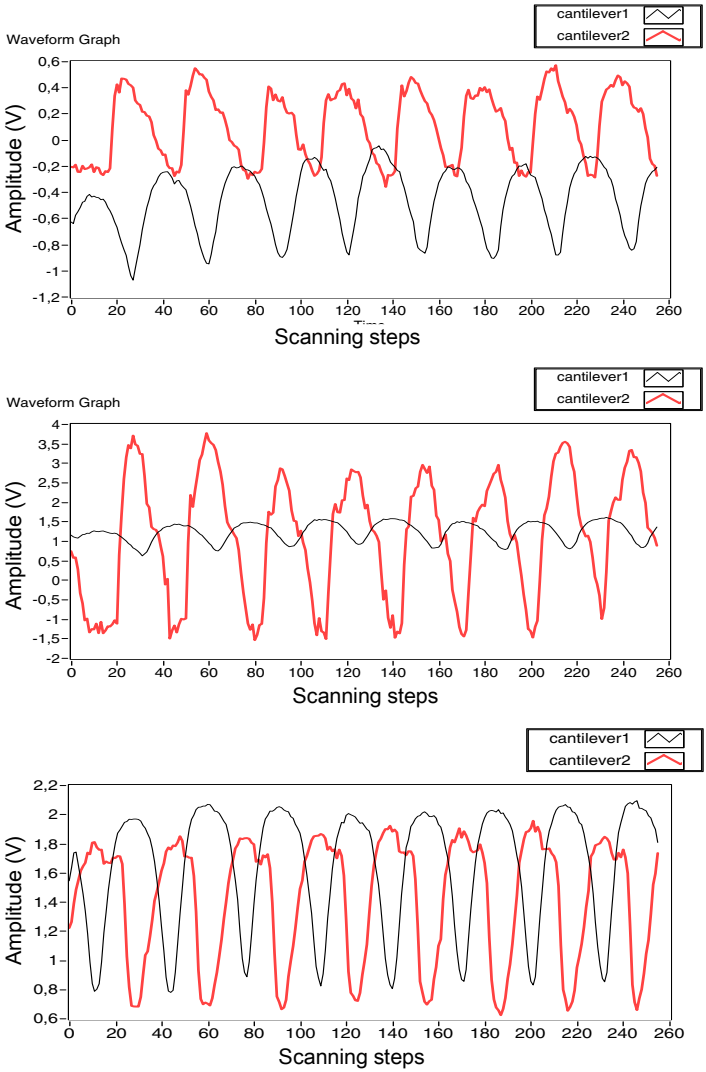

Figure 5.11 Signals of 1D sinusoidal grating of 300nm in pitch scanned by two TF cantilevers with (a) different set-points, (b) large different amplitudes but nearly the same set-points and (c) nearly the same set-points and amplitudes.

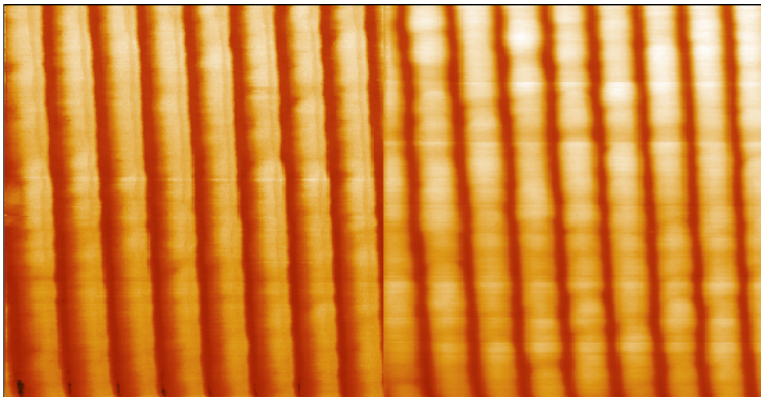

Figure 5.12 Simultaneously scanned images (2.5 μm × 2.5 μm).

5.5 Summary

The design and development of three cantilevers TF-AFM are presented. The characteristics and the performance of it with two TF cantilever are investigated and tested respectively.

6 AFM cantilevers as encoder for forward and backward displacement measurements

6.1 Decoding principle – phase unwrapping

In chapter 2, mathematic derivations have explained that two AFM cantilevers are needed to measure the forward and backward displacements along *x*- or *y*-axis by encoding 1D sinusoidal grating position. If two encoded sinusoidal signals expressed in equation (2-35) or (2-37) have π/2 phase shift between them and equal amplitudes which are in quadrature phase relationship in reference [50], the displacement can be decoded by using Equation (2-36) or (2-38), when one cantilever tip is motionless and another cantilever tip is controlled in advance by its tip phase HV-source to such positions that the distance of two cantilever tips are about equal to $(N+1/4)\cdot P$. Here suppose that 1D sinusoidal grating line is perpendicular to *x*-axis or *y*-axis. Equation (2-35) and (2-37) can be rewritten as:

$$\begin{cases} Y1(n) = A1\sin[\dfrac{2\pi}{P}S(n)] \\ Y2(n) = A2\cos[\dfrac{2\pi}{P}S(n)] \end{cases} \tag{6-1}$$

$Y1(n)$ and $Y2(n)$ denotes two 1D sinusoidal grating position-encoded signals probed by two AFM cantilevers. $S(n)$ denotes the displacement along *x*- or *y*-axis, which can be rewritten as

$$S(n) = \frac{P}{2\pi}\cdot\phi(n) \tag{6-2}$$

where, $\phi(n) = arc\tan(\dfrac{A2\cdot Y1(n)}{A1\cdot Y2(n)})$ (6-3)

Assuming two encoded quadrature signals without noise, they are expressed by equation (6-1) as usual, the forward and backward simulated encoded quadrature signals of 128 data points in period and 1 arbitrary unit in amplitude are plotted in figure 6.1(a), where *F*-$Y1(n)$ and *F*-$Y2(n)$ denote forward displacement signals while *B*-$Y1(n)$ and *B*-$Y2(n)$ denote backward displacement signals. The derived phases for forward displacement and backward displacement are plotted together in figure 6.1 (b), where they are expressed as *F*-phase and *B*-phase respectively by the legends.

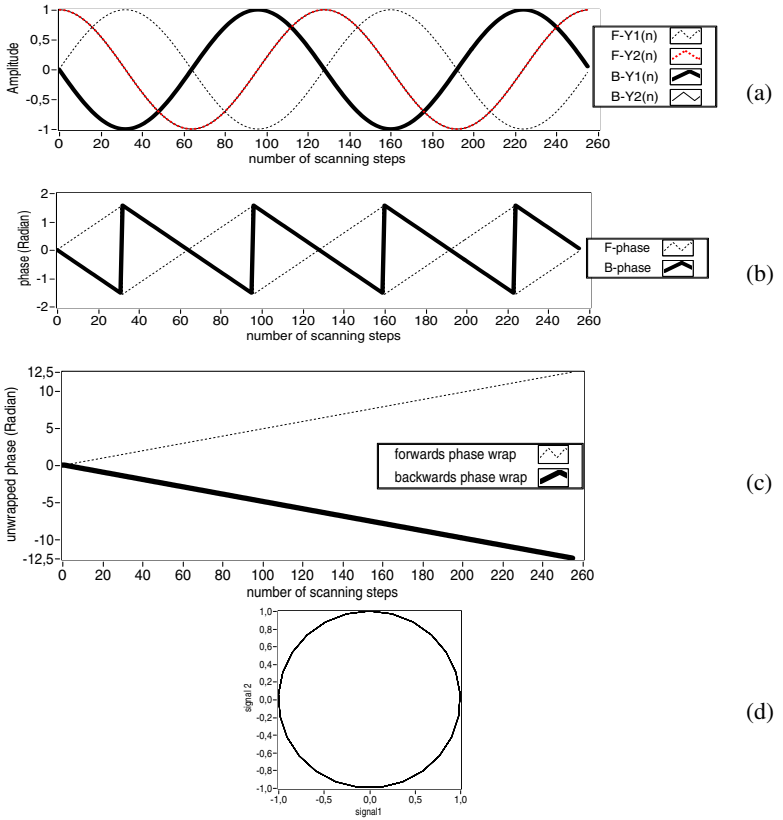

Figure 6.1 Ideal encoded quadrature signals for forward and backward displacements in (a), their quadrature phases are exhibited in (b), their unwrapped phases $\Phi(n)$ are plotted together in (c) and Lissajous circle is plotted in (d).

Ideal encoded quadrature phases as shown in figure 6.1(b) look like ramp waveforms in right triangle. The period of qaudrature phases are equal to a half of that quadrature signals. Its vertexes are $\pi/2$ and $-\pi/2$ for forward displacement phase (F-phase) or $-\pi/2$ and $\pi/2$ for backward displacement phase (B-phase) in correspondence to two consecutive phase elements $\phi(n\text{-}1)$ and $\phi(n)$. In any phase period there is always $\phi(n) > \phi(n-1)$ for forward displacement, and $\phi(n) < \phi(n-1)$ for backward displacement. Therefore the

direction can be distinguished. The phase $\phi(n)$ can be unwrapped. Referred from the algorithm in LabVIEW, the phase $\Phi(n)$ will be unwrapped by

$$\Phi(n)=\begin{cases}\sum_{i=1}^{n}\{[\phi(i)-\phi(i-1)]-\left\lfloor\frac{\phi(i)-\phi(i-1)}{\pi}+0.5\right\rfloor\cdot\pi\} & n=1,2,\cdots,M-1\\ \phi(n) & n=0\end{cases} \quad (6\text{-}4)$$

where M is the length of phase sequence. The expression $\left\lfloor\frac{\phi(i)-\phi(i-1)}{\pi}+0.5\right\rfloor$ denotes the floor function operation. The real-time displacement $S(n)$ can be calculated as

$$S(n)=\frac{P}{2\pi}\cdot\Phi(n) \quad (6\text{-}5)$$

By using unwrapping equation (6-4), the unwrapped phase for quadrature signals in figure 6.1(a) are plotted in figure 6.1 (c). The ideal Lissajous figure for quadrature signals is a circle with centre point at (0, 0) and radius of 1 arbitrary unit as shown in figure 6.1 (d).

It can be concluded from figure 6.1 and equation (6-5) that similar to the wavelength in optical interferometry, the smaller the pitch of 1D grating is, the higher the decoding resolution is.

6.2 Phases and unwrapped phases of two simulated 1D grating position-encoded signals

6.2.1 1D sinusoidal grating encoded signals

The two encoded sinusoidal signals of 128 data points in period, 1 arbitrary unit in amplitude with noise of 0.5 arbitrary units and with phase shift of π/2 for forward and backward displacements are plotted in figure 6.2(a), where *F-Y*1(*n*) and *F-Y*2(*n*) are forward displacement signals while *B-Y*1(n) and *B-Y*2(*n*) are backward displacement signals. Their phase waveforms are plotted in figure 6.2(b), where F-phase is derived from F-Y1(n) and B-Y1(n), while B-phase is derived from F-Y2(n) and B-Y2(n).

The unwrapped phases are plotted in figure 6.2 (c). Although noisy in the encoded sinusoidal signals, it seems that the phases possess some quadrature

property to some extent. However, Lissajous figure shown in figure 6.2 (d) is very noisy.

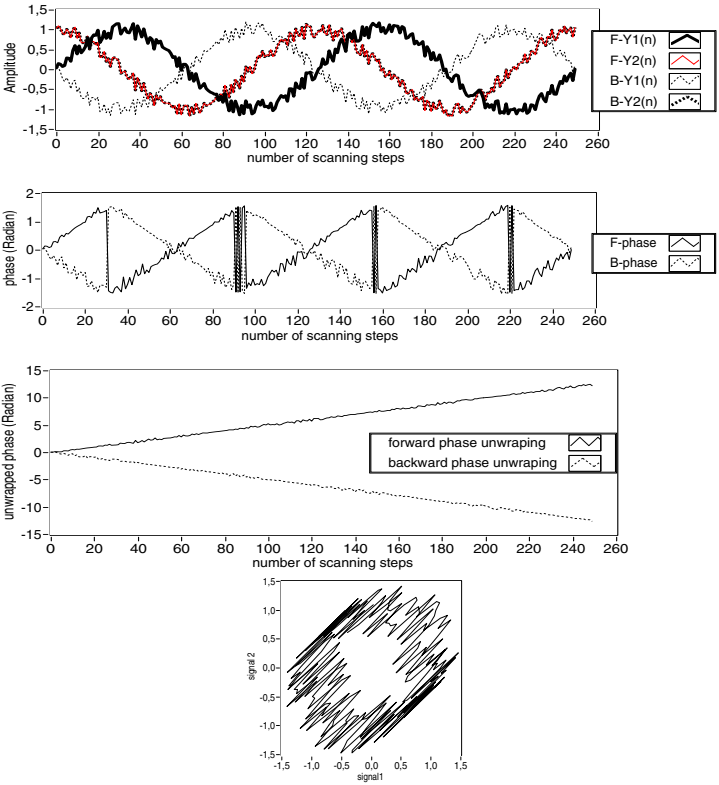

Figure 6.2 Encoded quadrature signals of forward and backward displacement with noise are plotted in (a), their phases in (b), unwrapped phases $\Phi(n)$ in (c) and Lisajous figure in (d).

Lacking the quadrature feature like optical encoders [51] and laser interferometers [52-53], the phase waveforms will deviate from quadrautre phase in various degrees. The simulations for several typical pairs of signal which lack the quadrature features are made by programming in LabVIEW, the plots of encoded signals, phase waveforms and unwrapped phase are shown in table 6.1 – table 6.3.

(1) If two encoded signals have phase shift between them, for example, of 60° ($\pi/3$) and 150° ($5\pi/6$) respectively in table 6.1 row (a), the hypotenuses of right triangle will become concave or convex as shown by their actual phase $\phi(n)$ plotted in table 6.1 row (b). It depends on whether the phase shift between two 1D sinusoidal grating encoded signals is more or less than $\pi/2$. It also depends on whether the two encoded signals are probed from forward displacement or backward displacement. As a comparison, the unwrapped phases and quadrature phase are plotted together in table 6.1 row (c), where the nonlinear error depends on how much actual phases deviating away from quadrature phase. In table 6.1 for phase shift of 60° (-30° deviation away from 90°) the nonlinear error is relatively small, while for phase shift of 150° (60° deviation away from 90°) the nonlinear error is relatively large. If the phase shift of two encoded signals is less than 90°, actual unwrapped phases are in wavy lines periodically smaller than or equal to unwrapped quadrature phase. If phase of two encoded signals is larger than 90°, the actual unwrapped phases will be wavy lines periodically larger than or equal to unwrapped quadrature phase.

(2) If two encoded signals have initial phase difference of 90° but different amplitude, for example the amplitudes of two encoded signals are 1 and 3 arbitrary units respectively in table 6.2 row (a), the hypotenuses of right triangle will become curved too, as shown by their actual phase $\phi(n)$ plotted in table 6.2 row (b). As a comparison, the unwrapped phase and unwrapped quadrature phase are plotted together in table 6.2 row (c), where the nonlinear error depends on how much amplitude difference between two encoded signals compared with that between two quadrature encoded signals.

(3) The worst is that two encoded signals have various different offset values which result in the different phase waveforms. For example, in table 6.3 row (a), offsets of $Y1(n)$, $Y1'(n)$, $Y2(n)$ and $Y2'(n)$ are 0, 2, 1 and 2 arbitrary units respectively, and the phases between $Y1(n)$ and $Y2(n)$, $Y1(n)$ and $Y2'(n)$, $Y1'(n)$ and $Y2(n)$, $Y1'(n)$ and $Y2'(n)$ plotted in table 6.3 row (b) are various waveforms which result in the unwrapped phases in various degrees of deviation from unwrapped quadrature phase from the beginning to the end shown in table 6.3 row (c).

Lacking the quadrature feature as discussed above, the Lissajous figures are in ellipse with different centre point, long axis, short axis and direction respectively shown in row (d) of table 6.1 – table 6.3.

Those scenarios described from table 6.1 to table 6.3 are observed in the experiments when 1D sinusoidal grating is encoded by two AFM cantilevers at present. This will be discussed in the next section of this chapter.

Table 6.1 other phase shifts than 90°

(a) Encoded signals	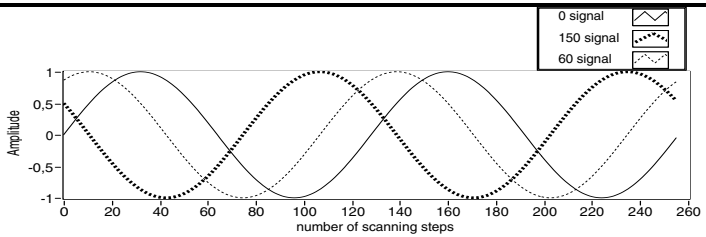
(b) Phase difference	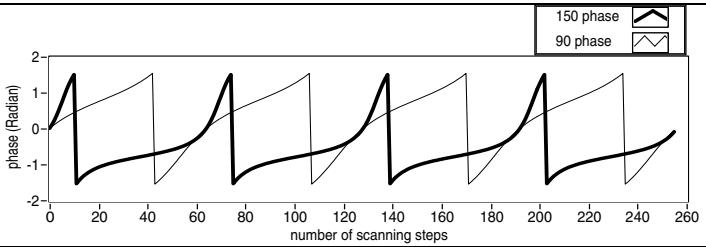
(c) Unwrapped phase	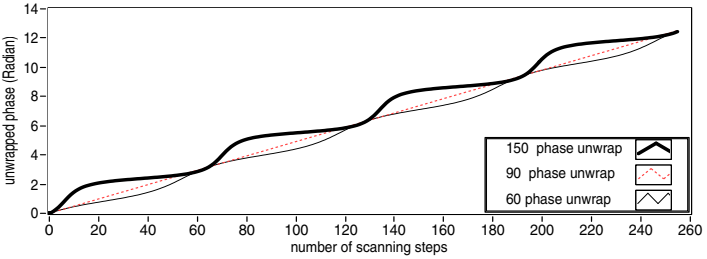
(d) Lisajous figure	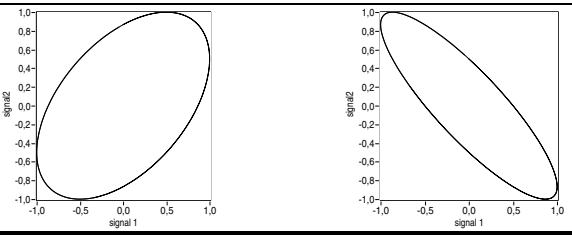

Table 6.2 different amplitudes of signals

(a) Encoded signals	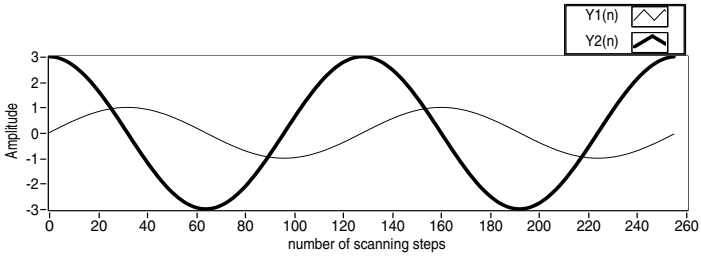
(b) Phase difference	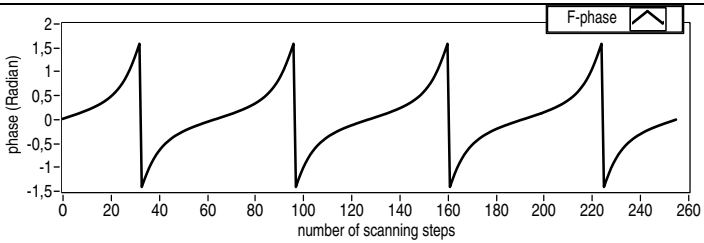
(c) Unwraped phase	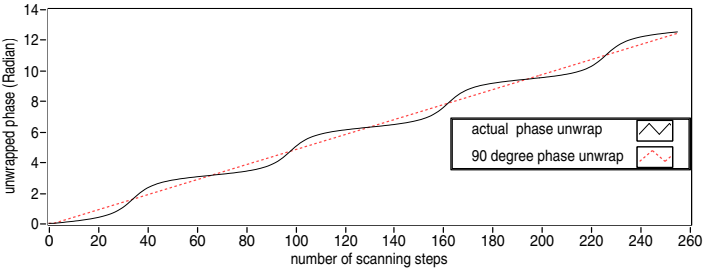
(d) Lisajous figure	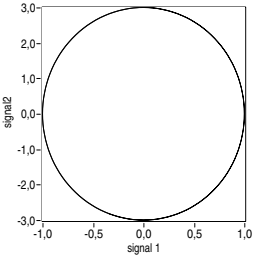

Table 6.3 Different offsets of signal

(a) Encoded signals	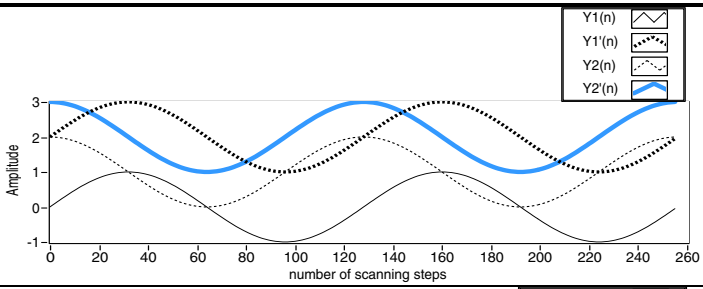
(b) Phase difference	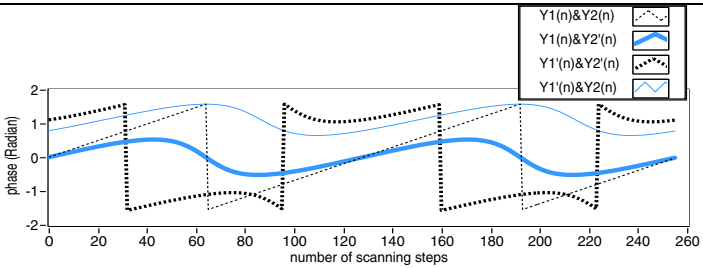
(c) Unwraped phase	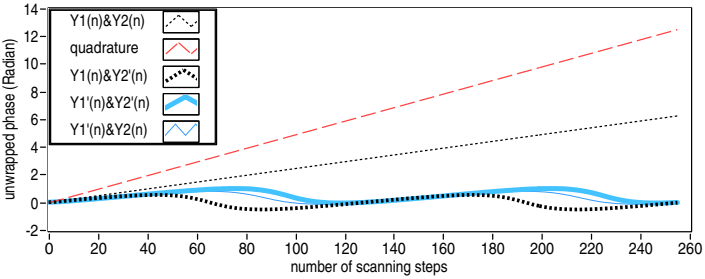
(d) Lisajous figure	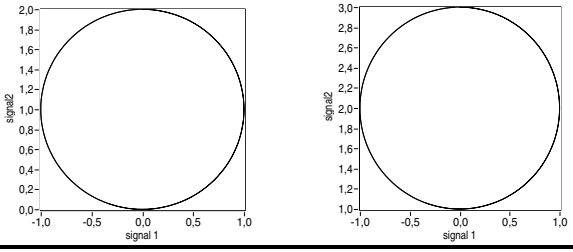

6.2.2 Phase of cross-correlation signals

The simulation in the previous sub-section has approved that 1D sinusoidal grating is a reasonable choice as the reference for generating quadrature signals, and for real-time displacement decoding by unwrapping the actual phases of two encoded sinusoidal signals with phase shift of $\pi/2$ as long as two encoded signals have neither tilt nor offset relative to zero. The smaller the pitch of 1D sinusoidal grating is, the higher the resolution of displacement measurement is. Nevertheless, it seems that at present fabrication techniques are more capable of fabricating 1D and 2D rectangular grating than fabricating 1D and 2D sinusoidal grating if it comes to the small pitch.

Of course, quadrature phase and unwrapped phase calculation equation (6-3) and (6-4) which are based on two quadrature signals expressed by equation (6-1) cannot be directly used for two 1D rectangular grating position-encoded signals and two 1D triangular grating position-encoded signals, even though they are in 90° phase shift. Without noise they are shown in figure 6.3 (a) and figure 6.4 (a) respectively, and their actual phase waveforms by using quadrature phase calculation equation (6-3) are shown in figure 6.3 (b) and figure 6.4 (b) respectively. As a matter of fact, phase peaks between two rectangular signals do not reach $\pi/2$ and $-\pi/2$ and phase peaks between two triangular signals intermittently reach $\pi/2$ and $-\pi/2$. Persisting on using the phase unwrapping equation, the unwrapped phases are plotted in figure 6.3 (c) and figure 6.4 (c). They are both discontinuously changing with data points just like saw teeth. Even the unwrapped phase changes with data points both toward to the backward displacement direction no matter the two simulated 1D rectangular signals are encoded from forward displacement or backward displacement.

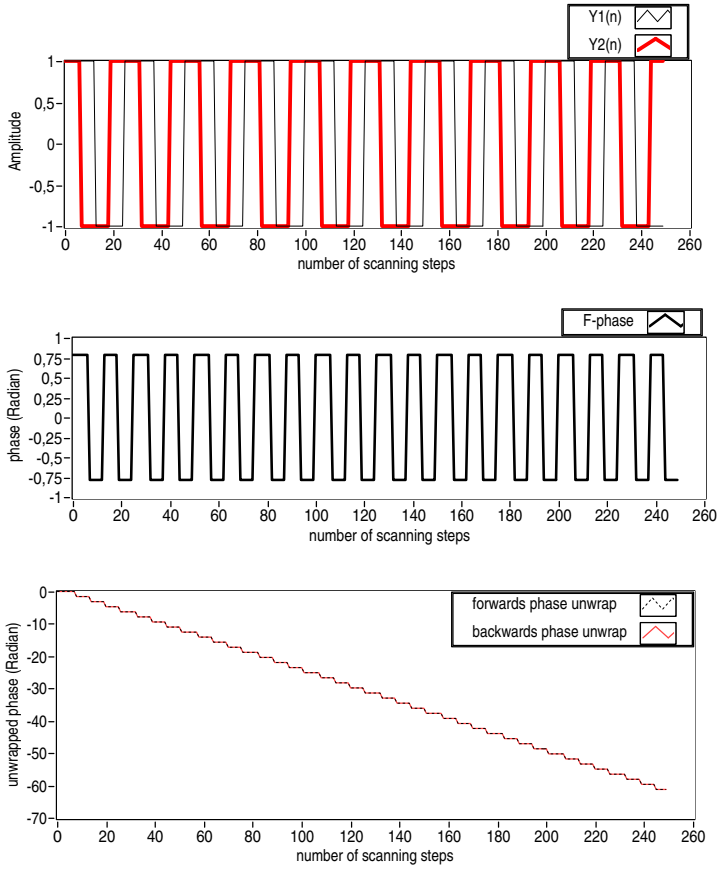

Figure 6.3 (a) Two 1D rectangular grating encoded signals with 90° phase difference and without noise; (b) The phase; (c) Unwrapped.

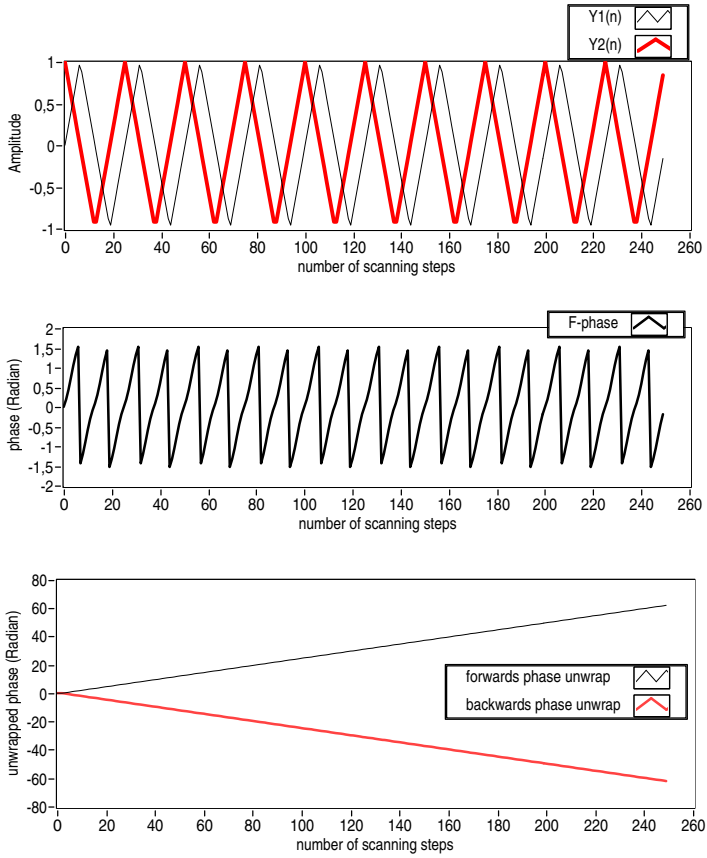

Figure 6.4 (a) Two 1D triangular grating encoded signals with 90° phase difference and without noise; (b) The phase ; (c) Unwrapped phase.

In chapter 4, it has been shown that 1D rectangular grating and 1D triangular grating are suitable to be used as the reference to pair with one AFM cantilever encoder for real-time displacement measurement based on the decoding principle - the count of integer period plus the calculation of fractional parts of a period from encoded signals. After cross-correlated with a half sinusoidal waveform template if its samples are approximately equal to

the half period of encoded signals, the cross-correlation signals have nearly the same periods as that of 1D rectangular grating and 1D triangular grating encoded signals. Nevertheless it is necessary to discuss the possibility of 1D rectangular grating and 1D triangular grating as the reference to pair with two AFM cantilevers encoder based on the decoding principle of quadrature phase unwrapping. It needs to be addressed that to what extent two 1D rectangular or triangular grating encoded signals probed by two AFM cantilevers and their cross-correlation signals resemble to sinusoidal signal.

Apparently, if the noise exists in 1D sinusoidal grating encoded quadrature signals probed by two AFM cantilevers from the beginning to the end, unwrapped phase is throughout accompanied with noise as illustrated in figure 6.2. Since two cross-correlation signals derived from two1D sinusoidal grating encoded signals can almost be free of noise and the phase shift between them should be the same as two encoded signals, cross-correlation signals derived from two encoded sinusoidal signals will also be considered in this section.

The cross-correlation signals expressed as $R1(n)$ and $R2(n)$ respectively are quadrature signals and in quadrature phase relationship, which are expressed as

$$\begin{cases} R1(n) = A_1 \sin[\dfrac{2\pi}{P} S(n)] \\ R2(n) = A_2 \cos[\dfrac{2\pi}{P} S(n)] \end{cases} \tag{6-6}$$

Then for one direction (forward) displacement perpendicular to the grating lines, the displacement calculated will be

$$S(n) = \frac{P}{2\pi} \cdot \phi(n) \tag{6-7}$$

where $\phi(n) = Arc\tan[\dfrac{R1(n)}{R2(n)} \cdot \dfrac{A_2}{A_1}]$ (6-8)

To answer the question that to what extent two1D rectangular or triangular grating encoded signals probed by two AFM cantilevers and its cross-correlation signals resemble to sinusoidal signals, the FPS of those cross-

correlation signals which have been investigated in section 4.2.4 should be mentioned again.

To make a comparison between the power spectra before and after cross-correlation calculation, it is found that the profiles of frequency distribution curves hardly change except that the amplitudes are increased by a factor. This means cross-correlation filtering can best suppress the high frequency part of noise, but it cannot suppress the multiple frequency components beyond the basic frequency (0.04 Hz) for the spectra of rectangular signals before and after cross-correlation filtering as shown in figure 4.9 (a) and figure 4.9 (b) as well as triangular signals before and after cross-correlation filtering as shown in figure 4.10 (a) and figure 4.10 (b).

To make a comparison among figure 4.3, figure 4.9 and figure 4.10, it is shown that 1D triangular grating encoded signal without noise is more sinusoidal and weaker in multiple frequency components before and after cross-correlation filtering than 1D rectangular grating encoded signal without noise. And it is unnecessary to say 1D sinusoidal grating encoded signal without noise is sinusoidal before and after cross-correlation filtering.

In table 6.4 the cross-correlation filtered signals are plotted in row (a), row (b) and row (c) for 1D sinusoidal grating, 1D rectangular grating and 1D triangular grating encoded simulation signals with amplitude of 1 arbitrary unit, 250 data points (number of scanning steps) in 10 cycles (period is 25) with 90° phase shift, without noise (in the legends of 'R1(n)-noiseless' and 'R2(n)-noiseless') and with noise of 0.5 arbitrary units in amplitude (in the legends of 'R1(n)-noise' and 'R2(n)-noise'). The simulated phase waveforms in the legends of 'noise' and 'noiseless' calculated from a pairs of cross-correlation filtered signals 'R1(n)-noise' and 'R2(n)-noise' as well as 'R1(n)-noiseless' and 'R2(n)-noiseless' are plotted respectively in row (a), row (b) and row (c) of table 6.5.

At a glance of the phase waveforms at row (a) and row (c) of table 6.5, it seems no large difference before and after cross-correlation filtering for two 1D sinusoidal grating and 1D triangular grating encoded signals without noise when compared with their phase waveforms before cross-correlation filtering shown in figure 6.1 (b) and figure 6.4 (b) respectively. However, for two 1D noiseless rectangular grating encoded signals, the phase waveform at row (b) of table 6.5 seems to be improved after cross-correlation filtering

compared with the phase waveform before cross-correlation filtering shown in figure 6.3 (b). Waveform amplitudes nearly approach to π/2 (about ±1.57) radian, which is the basic feature of quadrature phase.

Table 6.4 Cross-correlation signals derived from two encoded signals

(a) 1D sinusoidal signals	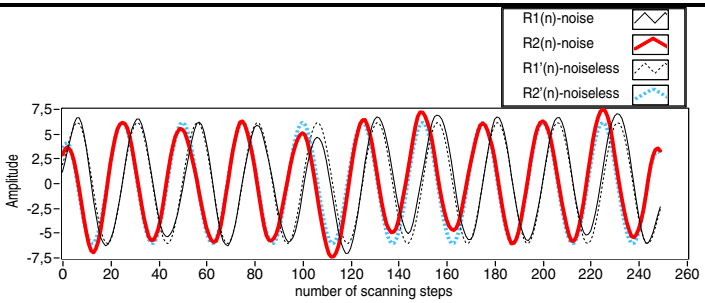
(b) 1D rectangular signals	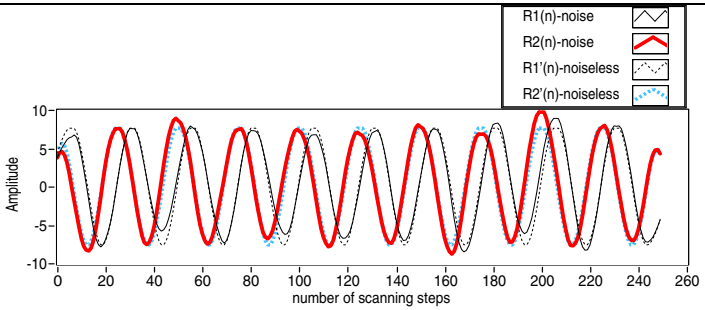
(c) 1D triangular signals	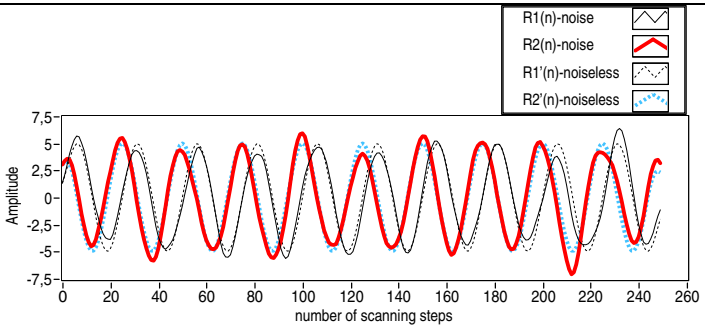

Table 6.5 Phase waveforms of two cross-correlation signals

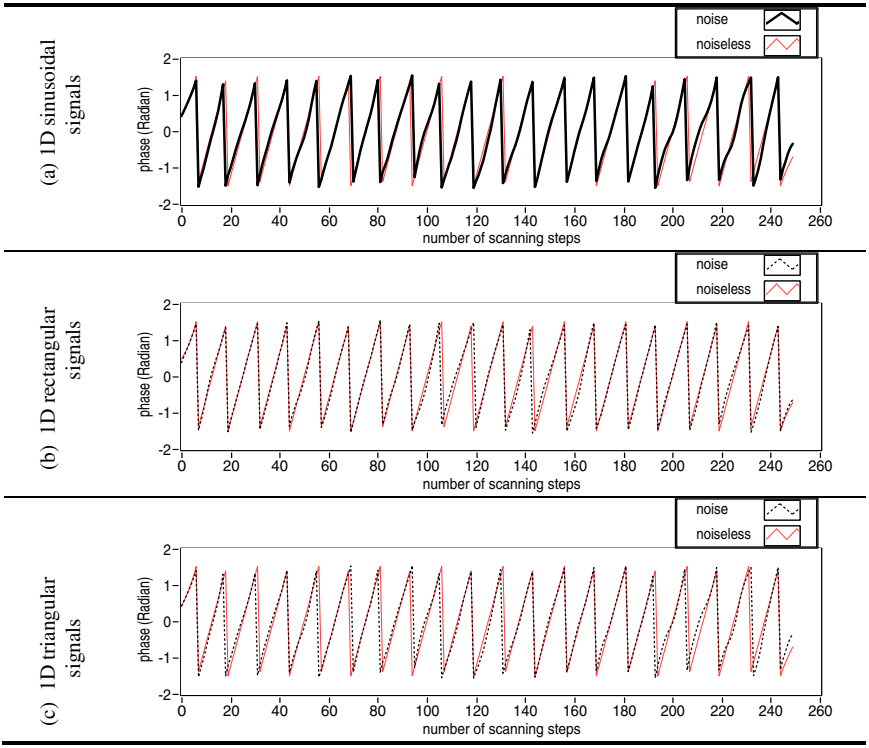

If 1D rectangular grating and 1D triangular grating are used as reference paired with two AFM cantilevers as encoder, and two cross-correlation signals calculated from two encoded signal are in 90° phase shift between them, what do the phase and unwrapped phase look like? The simulation results are plotted in figure 6.5 (a) and figure 6.5 (b) for the phase waveforms of two quadrature signals and two cross-correlation filtered signals of 1D sinusoidal, 1D rectangular and 1D triangular encoded signals with 90° phase shift between them and without noise and with noise 0.5 arbitrary. The phase waveforms of two cross-correlation filtered 1D sinusoidal, 1D rectangular and 1D triangular signals deviate from quadrature phase in variable degree. The phase deviations from quadrature phase are plotted in figure 6.6 (a) and 6.6 (b) without and with noise of 0.5 arbitrary units in amplitude respectively.

Dsq, *Drq* and *Dtq* are the legends which denote the difference between quadrature phase and the phases of two sinusoidal cross-correlation signals, two rectangular cross-correlation signals and two triangular cross-correlation signals respectively.

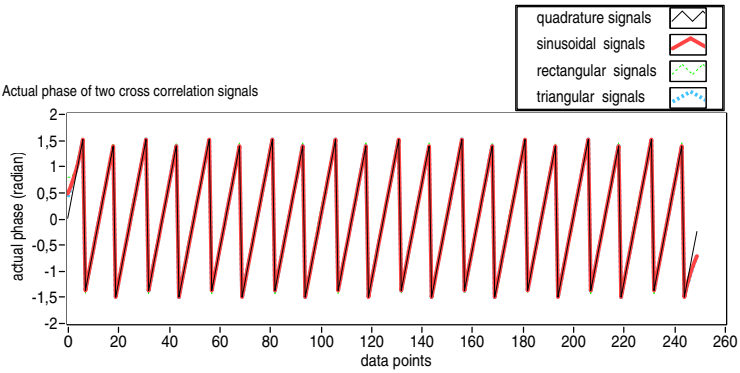

(a)

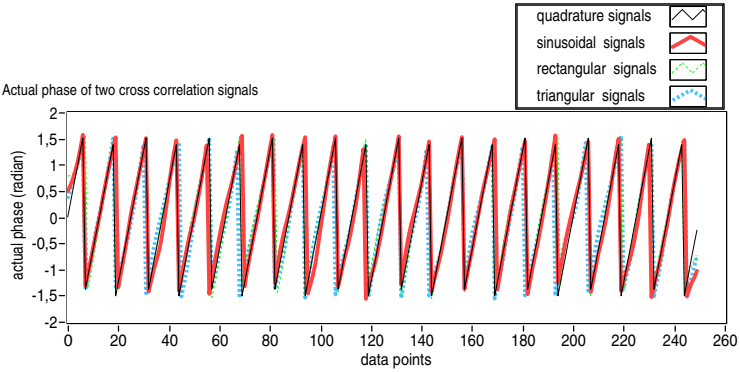

(b)

Figure 6.5 Phase waveforms of quadrature signals and two cross-correlation filtered sinusoidal, rectangular and triangular signals with 90° phase shift between them; (a) for the signals without noise and (b) for the signals with noise of 0.5 arbitrary units in amplitude.

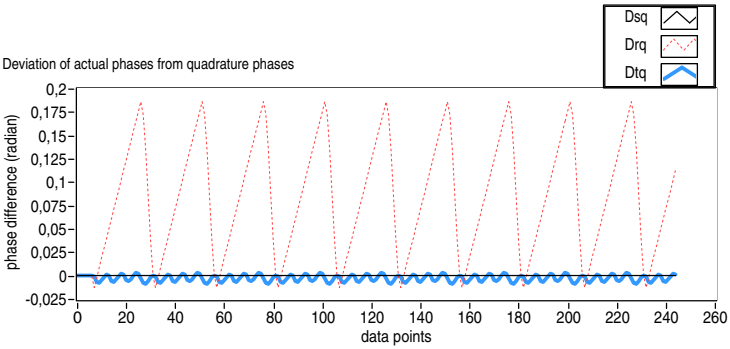

(a)

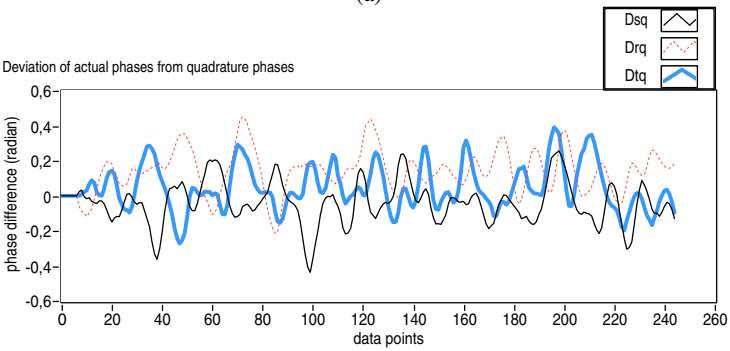

(b)

Figure 6.6 Deviations of two cross-correlation filtered 1D grating encoded signals from that of quadrature signals; (a) and (b) are for the signals without noise and with noise of 0.5 arbitrary units in amplitude respectively.

Table 6.6 RMS amplitudes and DC of *Dsq*, *Drq* and *Dtq*

		Dsq (radian)	*Drq* (radian)	*Dtq* (radian)
Without noise	RMS	0	0.1023	0.0045
	DC	0	0.0820	-0.0029
With noise	RMS	0.1382	0.1854	0.1360
	DC	-0.0416	0.1371	0.0453

Effective (RMS) amplitudes and mathematical means (DC) of *Dsq*, *Drq* and *Dtq* with and without noise are calculated. The data are listed in table 6.6. From table 6.6 it can be seen that *Drq* is quite larger than *Dsq* and *Dtq*. To

some extent, 1D rectangular grating is not suitable as a references for displacement measurement in phase unwrapping.

6.2.3 Criteria for choice of 1D grating

From simulation and analysis in subsection 6.2.1, 6.2.2, it is suggested that not 1D rectangular grating but 1D sinusoidal grating and 1D triangular grating can be used to be paired with AFM cantilevers encoder for forward and backward displacement measurement based on quadrature phase unwrapping.

6.3 Phase of differentiation signal

The sensitivity of TF cantilever is defined as the maximum frequency shift divided by the amount of tip displacement in the periodic contact region. It differs for each setting of the tip vibration amplitude of one cantilever. Because the maximum frequency shift and Q-factor etc are the specifically intrinsic and constant values for each TF cantilever and differ from other TF cantilevers. The amplitudes of any two encoded signals appear different. Besides, the noise exists throughout in the encoded signal. To deal with those problems, the cross-correlation filtering to the encoded signal discussed and explained in chapter 4 could be applied to suppress the noise. Furthermore, the cross-correlation signals can be normalized to be equal in signal amplitude.

The minimum displacement of Picomotor^{TM} is 30 nm per step. Although it is minimized to 10 nm due to the leverage between the props triangle and the tips triangle shown in figure 5.1 (b), the minimum step and its hysteresis does not allow stopping the TF cantilever at exactly zero PLL voltage set-point. Another point to be considered is the tilt of the sample surface relative to the plane given by the tips triangle during scanning. With the displacement of the sample, this is detected by the AFM cantilevers and generated as additional low frequency tilt components in the signals as shown in figure 6.7(a), which make the $Y1(n)$ and $Y2(n)$ tilted at different extent. It makes $R1(n)$ and $R2(n)$ even more tilted too. Therefore, it is necessary to differentiate the normalized cross-correlation signals to eliminate the low frequency tilt component. Usually the low frequency tilt component can be considered as linear, thus $R1(n)$ and $R2(n)$ will be expressed as

$$\begin{cases} R1(n) = A_1 \sin[\dfrac{2\pi}{P} S(n)] + B_1 n + C_1 \\ R2(n) = A_2 \cos[\dfrac{2\pi}{P} S(n)] + B_2 n + C_2 \end{cases} \tag{6-9}$$

To calculate the first differentiation of $R1(n)$ and $R2(n)$, equation 6-9 will become

$$\begin{cases} D_1(n) = A'_1 \cos[\dfrac{2\pi}{P} S(n)] + B_1 \\ D_2(n) = A'_2 \sin[\dfrac{2\pi}{P} S(n)] + B_2 \end{cases} \tag{6-10}$$

where $A'_1 = \dfrac{2\pi}{P} A_1$ and $A'_2 = -\dfrac{2\pi}{P} A_2$.

To calculate the second differentiation of $R1(n)$ and $R2(n)$, equation (6-10) will become

$$\begin{cases} D''_1(n) = A''_1 \sin[\dfrac{2\pi}{P} S(n)] \\ D''_2(n) = A''_2 \cos[\dfrac{2\pi}{P} S(n)] \end{cases} \tag{6-11}$$

where $A''_1 = -(\dfrac{2\pi}{P})^2 \cdot A_1$ and $A''_2 = -(\dfrac{2\pi}{P})^2 \cdot A_2$. $D_1''(n)$ and $D_2''(n)$ can be called second differentiated signals. From equation (6-11), it can be seen that the tilts of signal can be eliminated. However the phase difference between $D_1(n)$ and $D_2(n)$ signals as well as between $D_1''(n)$ and $D_2''(n)$ remain $\pi/2$ as shown in figure 6.7(b), which respectively can be expressed as

$$\phi(n) = Arc\tan[\frac{D_1(n) - B1}{D_2(n) - B2} \cdot \frac{A'_2}{A'_1}] \tag{6-12}$$

$$\phi(n) = Arc\tan[\frac{D''_1(n)}{D''_2(n)} \cdot \frac{A''_2}{A''_1}] \tag{6-13}$$

The actual phases between $Y1(n)$ and $Y2(n)$, $D1(n)$ and $D2(n)$ and $D1''(n)$ and $D2''(n)$ are plotted in figure 6.7 (c), where they are represented by the legends of $Y(n)$-phase, $D'(n)$-phase and $D''(n)$-phase respectively.

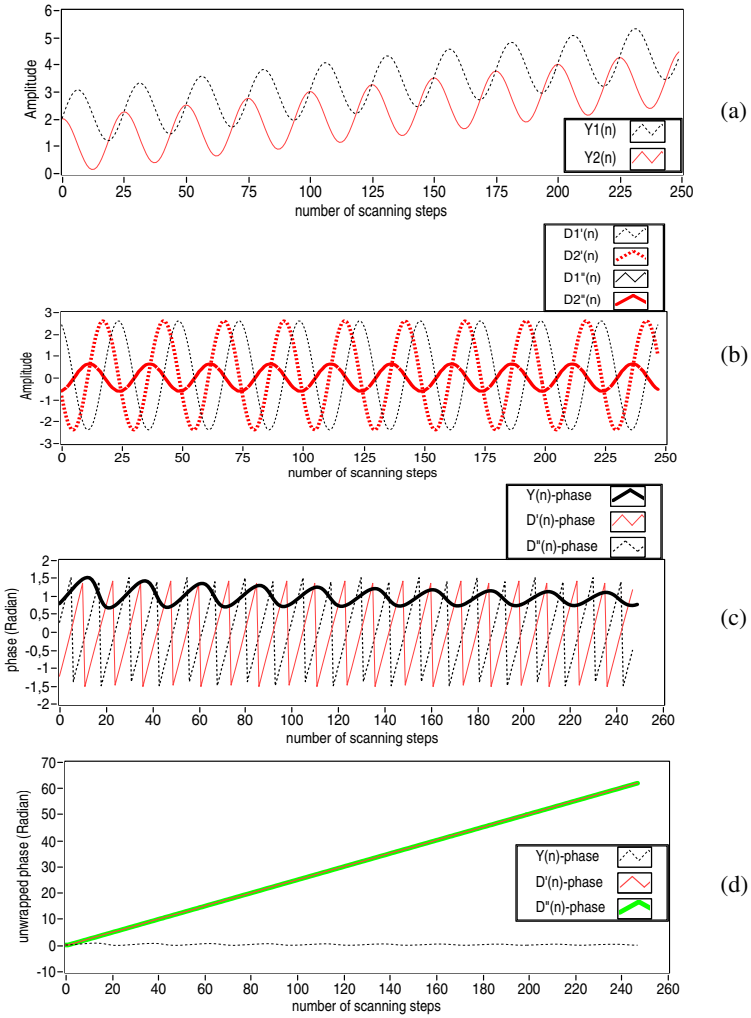

Figure 6.7 (a) Two tilted encoded signals $Y1(n)$ and $Y2(n)$; (b) First and second differentiation signals $D1(n)$ and $D2(n)$, $D1''(n)$ and $D2''(n)$; (c) Actual phases between $Y1(n)$ and $Y2(n)$, $D1(n)$ and $D2(n)$, $D1''(n)$ and $D2''(n)$; (d) Unwrapping of $Y(n)$-phase, $D'(n)$-phase and $D''(n)$-phase.

6. 4 Experiments and results

6.4.1 Phase of cross-correlation signals and real-time displacement

Unwrapping the phase from cross-correlation signals, the experimental results are shown in figure 6.8.

6.4.2. Phase of differentiation signals and real-time displacement

Unwrapping the phase from differentiation signal, experimental results are shown in figure 6.9.

6.4.3 Real-time two direction displacement measurements

The two direction displacements have been measured in AEM and PEM, respectively.

Two 1D sinusoidal grating encoded signals $Y1(n)$ and $Y2(n)$ in AEM are plotted together in figure 6.10 (a). They have approximately 90° phase shift when the x-scanning stage is controlled to move forwards from the beginning to about 563 scanning steps, and approximately -90° phase shift when the x-scanning stage is controlled to move backwards for 515 scanning steps. Their noiseless differentiation signals $D1(n)$ and $D2(n)$ plotted in figure 6.10 (b) look more intuitive when the forward or backward displacement is concerned. However, the phase waveform of two differentiation signals shown in figure 6.10 (c) is the most obvious to tell the direction of displacements. Correspondingly the phase is unwrapped as forward and backward displacements in real time shown in figure 6.10 (d).

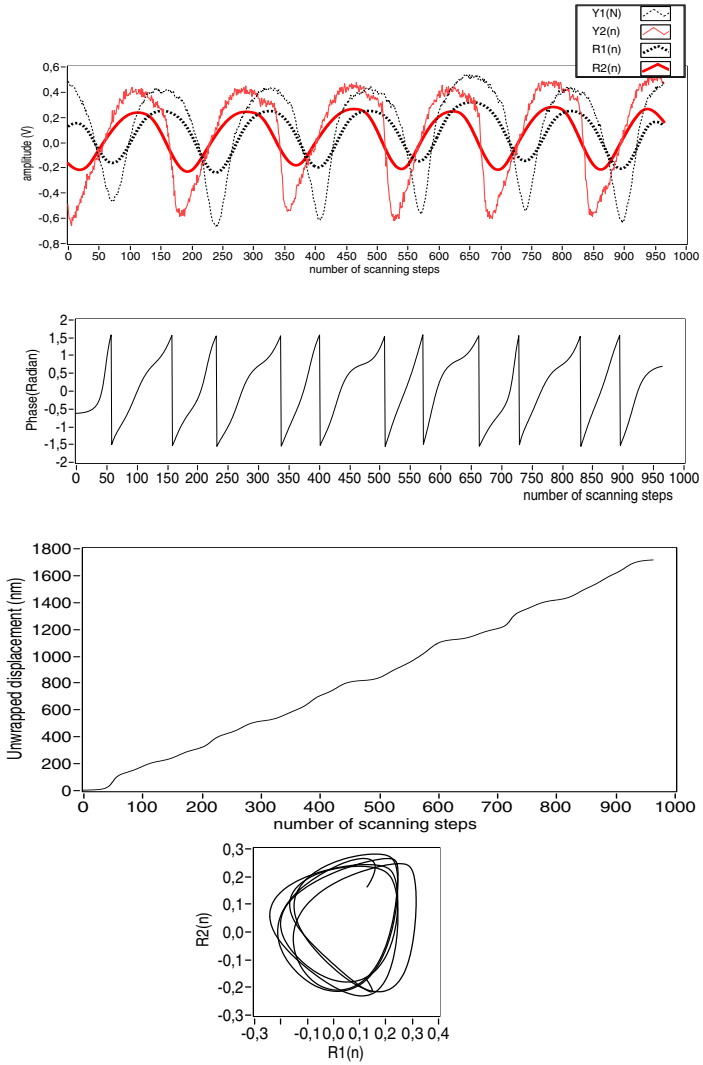

Figure 6.8 Waveforms of $Y1(n)$ and $Y2(n)$, $R1(n)$ and $R2(n)$ with approximate $\pi/2$ phase differences are shown in (a) , their phase difference derived from (a) is shown in (b), unwrapped displacement is shown in (c) and Lissajous figure is shown in (d).

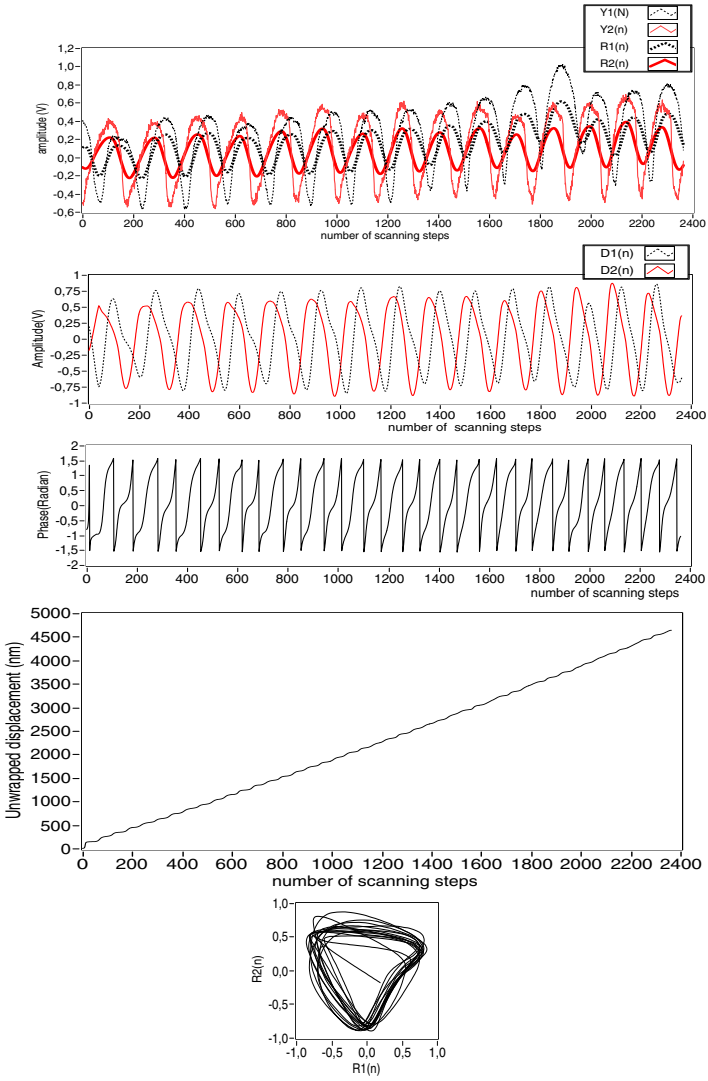

Figure 6.9 (a) signals of $Y1(n)$ and $Y2(n)$, $R1(n)$ and $R2(n)$ have low frequency tilt components; (b) their differentiation signals $D1(n)$ and $D2(n)$; (c) the phase waveform; (d) unwrapped displacement; (e) Lisajous figure is shown in (e).

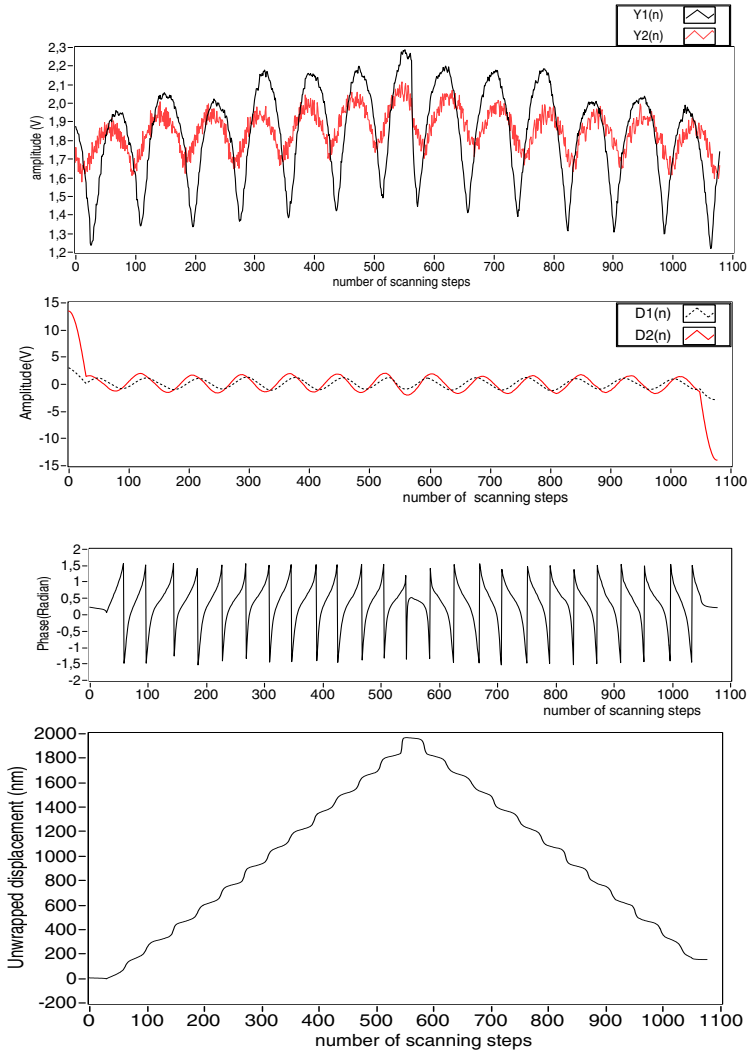

Figure 6.10 Encoded signal $Y1(n)$ and $Y2(n)$ is shown in (a), differentiation signals $D1(n)$ and $D2(n)$ is shown in (b), phase waveform is shown in (c) and real-time forward and backward displacements unwrapped from phase waveform in (c) is shown in (d).

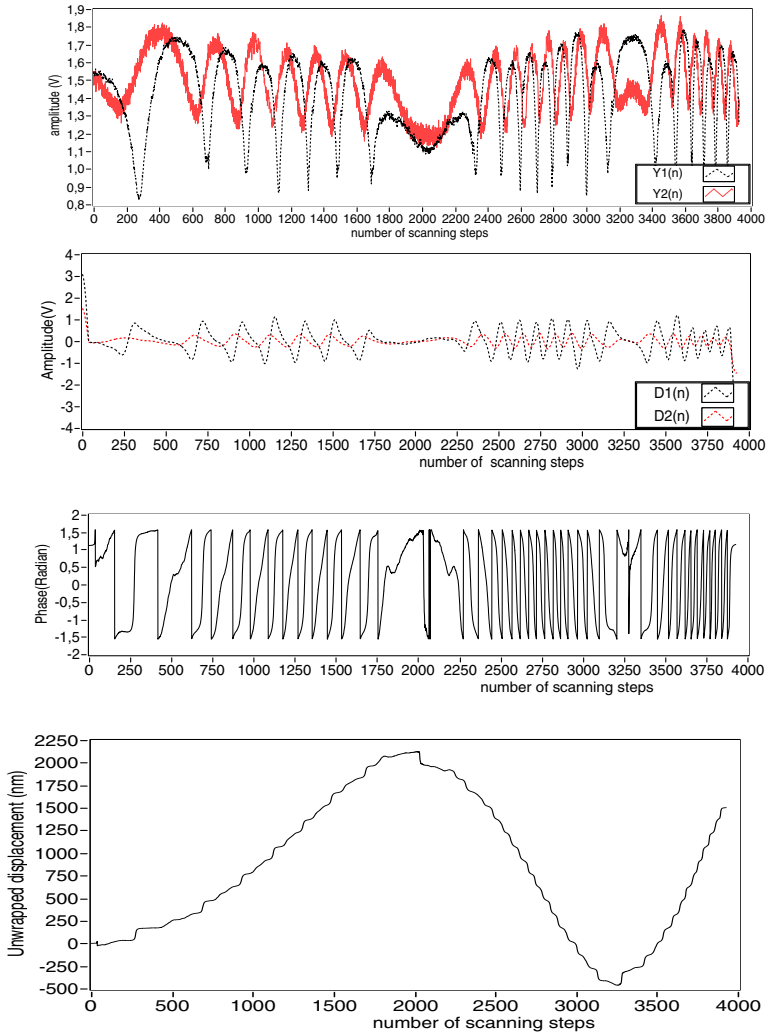

Figure 6.11 Experiment in PEM: (a) is encoded signal $Y1(n)$ and $Y2(n)$, (b) is differentiation signals $D1(n)$ and $D2(n)$, (c) is the phase waveform and (d) is the real-time forward and backward displacements unwrapped from the phases in (c).

Two 1D sinusoidal grating encoded signals $Y1(n)$ and $Y2(n)$ in PEM are plotted together in figure 6.11 (a) when x-scanning stage is individually driven by ramp voltage of 10mHz in frequency and 200 mV in peak-peak amplitude with 100 mV offset output from the signal generator. When driven by the rising edge and falling edge of the ramp voltage, x-scanning stage moves forwards and backwards respectively. From the encoded signals recorded in figure 6.11 (a), it can be seen that the displacement changes direction twice. So are their differentiation signals $D1(n)$ and $D2(n)$ as well as phase waveform plotted in figure 6.11 (b) and figure 6.11 (c) respectively. Correspondingly the phase is unwrapped in real time as forward and backward displacements shown in figure 6.11 (d). With PEM, if one encoded data is digitally acquired by DAQ, only after the encoded data sequence is cross-correlation filtered, and real-time displacement is decoded, the next encoded data can be digitally acquired. If the time interval between any two encoded data becomes longer and longer with the accumulated data increasing, the data acquired in a period of grating line becomes less and less. Therefore PEM mode is actually similar to that displacement is measured when x-scanning stage is driven to move in gradually changing speed. That is the reason why the waveform widths of encoded signals $Y1(n)$ and $Y2(n)$, subsequently their differentiation signals $D1(n)$ and $D2(n)$ as well as phase waveform become narrower and narrower.

6.4.4 Comparison between the decoding methods

When x-scanning stage is controlled in open-loop to move, its displacements have been measured by two cantilevers based on direct decoding from encoded signals as shown in figure 6.12 (a). The displacement differences between two cantilever encoded signals from scanning step to scanning step are calculated. The average of displacement differences is within 50 nm for the displacement between 800nm and 13000 nm as shown in figure 6.12(b). Real-time displacement measurements, legends in ‘displacement1’ and ‘displacement2’ start from 800nm and 600nm respectively. Displacements are linearly extrapolated from 0 to 800nm for ‘displacement1’ and from 0 to 600nm for ‘displacement’ based on the fact that hysteresis of piezoelectric scanning stage at the beginning is small. If the In the scanning stage is driven in certain step voltage, the scanning steps Nq in the first one or two integer pitches corresponding to that step voltage is measured in advance, the

displacement in this part will be extrapolated by $S(n) = P \cdot n / Nq$, where P is the pitch of 1D grating. Nevertheless the consequence of extrapolation is that the displacement differences are quite larger from 600nm to 800nm in figure 6.12 (b), which means this kind of linear extrapolation is unsuccessful.

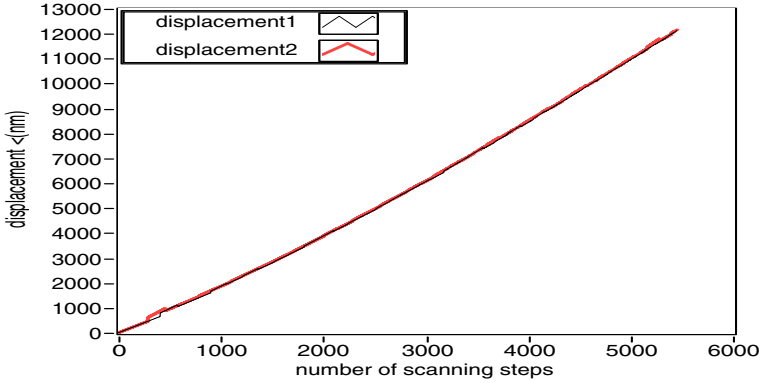

(a)

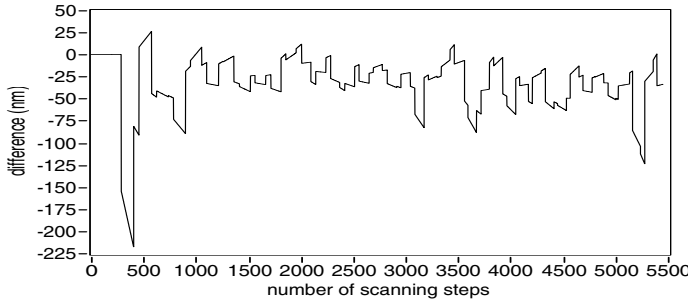

(b)

Figure 6.12 Displacements directly decoded from two encoded signals are shown in (a) and displacements difference is shown in (b).

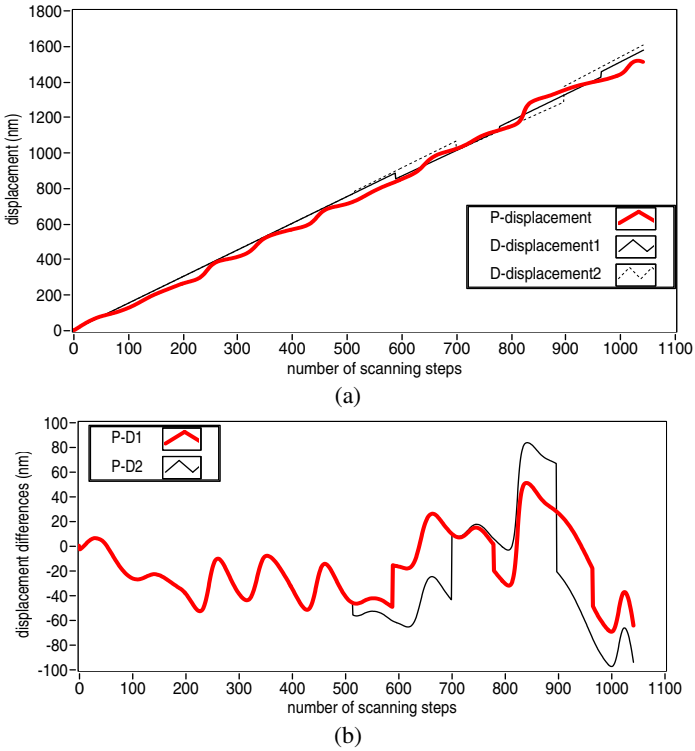

Figure 6.13 Displacements decoded by two methods are shown in (a) and displacement differences are plotted in (b) .

The displacements are both real-time measured by direct decoding method and the phase unwrapping method. The displacement curves shown in figure 6.13(a) are directly decoded from encoded signal probed by cantilever 1 in the legend of 'D-displacement1' and cantilever 2 in the legend of 'D-displacement2' as well as unwrapped from the phase in the legend of 'P-displacement' derived from two encoded signals picked-up by cantilever 1 and cantilever 2 in real time. The displacement differences between 'P-displacement' and 'D-displacement1' as well as between 'P-displacement' and 'D-displacement2' from one scanning step to another are plotted in figure 6.13(b).

From figure 6.12 (b) and figure 6.13 (b) it can be seen that at present the displacement differences larger than that expected. The main reasons for that are briefly explained as follows.

For direct decoding of encoded signal, 1D sinusoidal grating position-encoded signal in one area scanned by one TF cantilever is not only point to point but also pitch to pitch different from the signal in another area scanned by another TF cantilever because of the lack of uniformity of 1D sinusoidal grating. That results in the differences of displacements corresponding to the scanning steps as shown in figure 6.12 (a) and 'D-displacement1' and 'D-displacement2' in figure 6.13 (a).

For direct unwrapping of actual phase, 1D sinusoidal grating position-encoded signals scanned by TF cantilevers are distorted as lacking sinusoidal property. It results in the lack of quadrature phase between two signals scanned by two AFM cantilevers, so that there are local nonlinear errors within each pitch of displacement as shown in figure 6.8(c), figure 6.9(c), figure 6.10(d), figure 6.11(d) and the 'P-displacement' curve in figure 6.13(a). Even if 1D sinusoidal grating position-encoded signal is sinusoidal in a short displacement, it cannot last for a long displacement because of the imperfect of AFM cantilever as the encoder so far.

6.5 Summary

Two TF cantilevers as the encoder are investigated and the experiments have proven that without knowledge of direction in advance, forward and backward displacement measurements are feasible and practically operable based on the developed decoding principles—phase unwrapping, although the nonlinear errors caused by lacking quadrature phases have not been addressed so far. Based on the decoding principle, the AFM cantilevers as encoder seem very promising for the high resolution displacement measurement and positioning. However, in order to realize long and precision displacement measurement, AFM cantilevers encoder needs to be improved and optimized in mechanical unit and AFM feedback control loop, so that nearly perfect sinusoidal or quasi sinusoidal signals with quadrature phase shift can be consistently acquired, and the nonlinear errors caused by lacking quadrature phases in AFM cantilevers encoder can be real-time compensated or corrected just as what have been done in optical interferometer [54-56].

7 Conclusion and prospect

7.1 Conclusion

In this thesis it has been fulfilled that

1) a proposition on how AFM cantilevers can be used as the qualified encoder,
2) mathematical derivation and simulation of decoding methods which allowing direct decoding and phase unwrapping of the relevant 1D grating position encoded signals,
3) design, development and test of instruments: one TF cantilever AFM and AFM head equipped with three TF cantilevers,
4) real-time displacement measurement experiments accomplished by using one AFM cantilever and two AFM cantilevers used as encoder based on direct decoding and phase unwrapping respectively.

When one AFM cantilever is used as encoder paired with 1D grating of any shape, it can realize the real-time forward or backward long displacement measurement based on directly decoding the encoded signal, which is the count of integer waveforms plus the calculation of fractional parts of a waveform at beginning and at the actual or end position. The measurement resolution in AEM depends on the control resolution of measured micro-moving stage, for instance, x-y piezoelectric scanning stage of 100 μm × 100 μm in stroke (P-621.2 CD of Physik Instrumente GmbH) in this application has step control resolution of **2.2 nm**. And in PEM a measurement resolution of **0.03 nm** has been achieved. The robust measurement speed is ≤ **2 μm/s** if the repeatability and resolution are considered. To monitor x-y piezoelectric stage mentioned above moving to a preset displacement when it is controlled by a computer through its controller in closed-loop and open-loop based on its built-in capacitance sensors, the measurement repeatability is **2.2 nm** in a 70 μm displacement range. Direct decoding method is very practical for the measurements of in-plane small tilt angle, in-plane rotation angle within 90° range and hysteresis of piezoelectric scanning stage etc.

When two AFM cantilevers are used as encoder paired with 1D sinusoidal grating, it can realize real-time forward and backward displacement measurements in AEM and PEM based on phase unwrapping, which is to

wrap the phases of two encoded signals if they have approximately 90° initial phase shift between them.

7.2 Application prospect

To compare of the advantages among nanometre scale displacement measurement techniques at the beginning of this thesis with AFM cantilevers as the encoder on

1. non-contact, low-cost and high speed,
2. miniaturization, integration and high resolution,
3. metrologically direct and simple SI-traceability.

The results are presented in table 7.1. It can be seen that capacitive position sensor and AFM cantilevers encoder are two robust nanometre scale displacement measurement techniques if the comprehensive performance is considered.

Table 7.1 Comparison among nanometre scale displacement measurement techniques

	Typical resolution	Speed	Typical cost	Miniatu-rization	Traceability
laser heterodyne interferometry	< 1 nm	high	high	bulky	direct
x-ray interferometry	< 10 pm	very low	high	bulky	direct
diffraction grating encoder	< 1 nm	high	medium	bulky	by calibrated grating
Capacitive position sensor	< 10 pm	high	medium	smaller	by laser interferometer
AFM cantilevers encoder	< 1nm	low	medium	small	by calibrated grating

However if metrological traceability is considered, AFM cantilevers encoder allows real-time displacement measurement traceable to a certified calibration grating of high quality. This provides a displacement measurement in a more or less direct way. In opposite the capacitive position

sensor can only give voltage or current values in real time, and has therefore to be calibrated by the laser interferometer shown in figure 1.2. Due to its sensitivity to environment drift, capacitive position sensor needs to be periodically recalibrated. For AFM cantilevers encoder, as mentioned above only 1D grating needs to be calibrated beforehand. Such grating can be used over long time and if a low thermal expansion substrate is used, its parameters won't be subjected to the temperature change, although it might be exposed to the ambient dust.

In this PhD work, each of the two TF cantilevers is independently closed-loop controlled by a cantilever bending detection unit which includes a preamplifier, a self-oscillation and PLL circuit, a PI controller, a HV source and a z-fine piezo. Before only two STM tips [34-35, 57] and four STM tips [58] were handled similarly like this. When it comes to AFM, only array-based micromechanical cantilevers in one chip were investigated as multi-cantilevers AFM [59-60] before, because of the limitation of AFM cantilevers choice. This PhD work is all a great success - thanks to Dr Akiyama, the inventor of TF cantilevers.

7.3 Challenges and improvements

7.3.1 Increase of measurement speed

As shown in table 7.1, to guarantee the measurement accuracy, the real-time displacement measurement speed of AFM cantilevers encoder is low compare with laser interferometer, optical encoder and capacitive position sensor when it paired with 1D grating as a reference. The reason is that encoded signal sequence but not single data is cross-correlated with a half sinusoidal waveform template. The calculation time increases with growing signal data. To reduce the calculation time, two methods are suggested.

(1) Hardware solution: using field programmable gate array (FPGA) as digital signal processing module to replace the DAQ module, which can assure high speed real-time input and output (RIO) and computer cross-correlation processing simultaneously,
(2) Software solution: calculating cross correlation with a half sinusoidal waveform template in real time by using only a fractional length of data Γ but not the whole encoded signal sequence M.

Using this method, two conditions must be distinguished:

$$M \le \Gamma, \quad R(m) = \sum_{n=0}^{N-1} T(n) \cdot Z(n+m), \quad 0 < m \le M-1$$

$$M > \Gamma, \quad R(m) = \sum_{n=0}^{N-1} T(n) \cdot Z(n+m), \quad M - \Gamma \le m < M-1$$

Flowchart of cross-correlation filtering and real-time displacement decoding should be like that shown in figure 7.1.

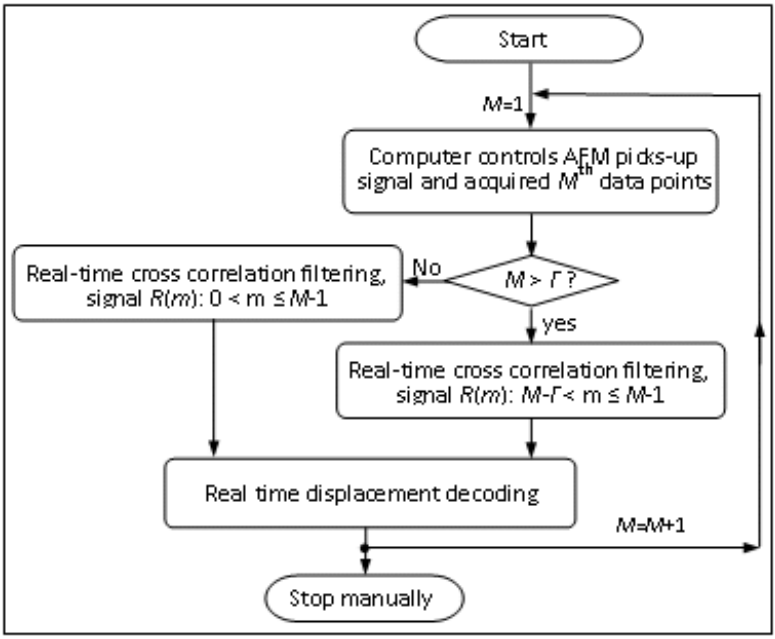

Figure 7.1 Flowchart of cross-correlation filtering and real-time displacement decoding

A combination of both certainly would be more useful for AFM cantilever to achieve the displacement measurement in the high speed.

7.3.2 Improvement of mechanical structure

In ideal situation, the tips triangle is approximately equilateral as shown in figure 7.2 (a), where it can be seen that effects of light reflections from three tuning forks make them appear in the same color in the photo, which means that each of three tuning forks is one face of a virtual normal triangular pyramid as shown in figure 7.2 (b), which means three tuning forks tilt the same angle in out-of-plane.

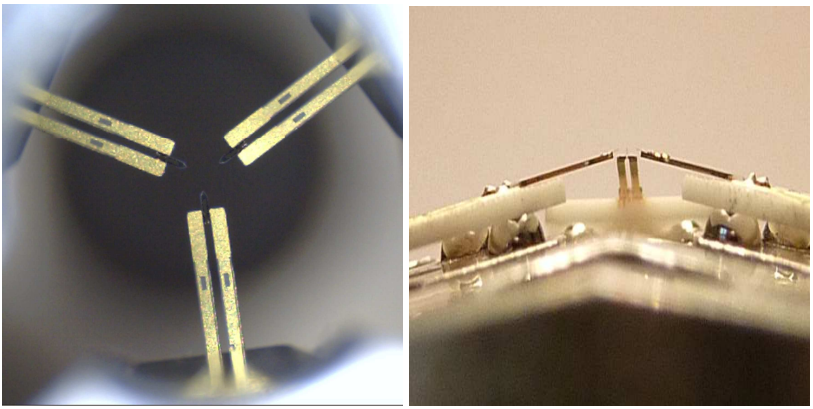

(a) (b)

Figure 7.2 Ideal installations of three TF cantilevers which form an equilateral tip triangle in (a) and form a normal triangular pyramid in (b).

In real situation, the tips triangle is not equilateral as shown in figure 7.3 (a), where it can be seen that effects of light reflections from three tuning forks make them appear in different color in the photo, which means that three tuning forks cannot form a normal triangular pyramid, and each of three tuning forks tilts an angle in out-of-plane. The reasons are

(1) the dimension of one fabricated tuning fork differs from that of the others, so that the lengths vary from 2.5 mm to 2.9 mm as shown in figure 7.4,
(2) the thicknesses of the ceramic plate vary from 0.35 mm to 0.48 mm, so that small change of tilt results in a large offset in the height.

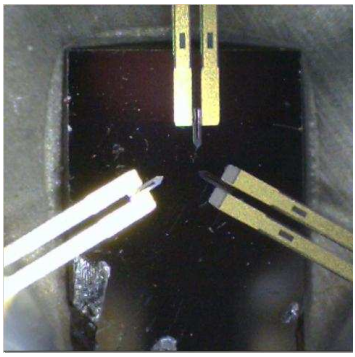

Figure 7.3 Real tips triangle

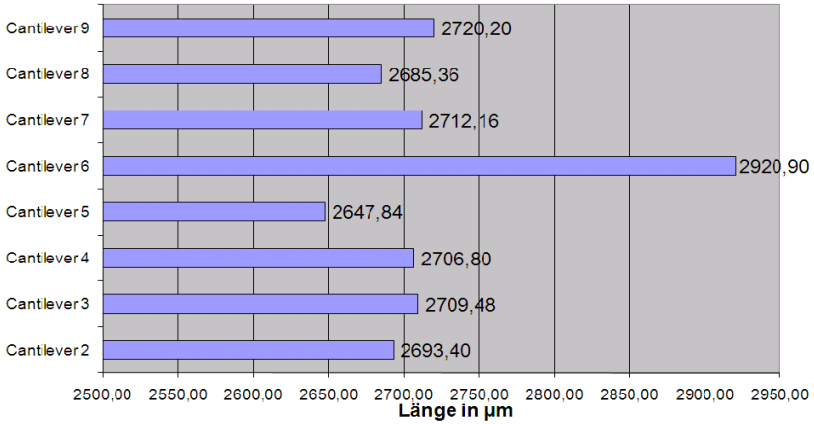

Figure 7.4 Lengths of tuning forks in one box

Therefore during this PhD work, it is very psychologically and physically demanding to align even two of three cantilevers to approach to 1D grating samples because three TF cantilevers are mechanically mounted in one monolithic base as shown in figure 5.2 (b), and if one TF cantilever tip is controlled to approach to and retract from sample by two picomotors^{TM} in vicinity, the positions of two other TF cantilever tips relative to the sample

surface will be influenced to change. Recently it took several days to do this, but finally failed and as a result a half dozen of TF cantilevers were damaged.

The best solution would be that each cantilever has its own base and is controlled to approach to and retract from sample independently by one picomotor™ or the z-fine piezo has larger stroke for fine-aligning of each TF cantilever.

Appendix

Appendix A: Scanning probe microscopy (SPM) [20, 21]

A.1 Scanning tunneling microscopy (STM)

The scanning tunneling microscope (STM) is the ancestor of all scanning probe microscopes. It was invented in 1981 by Gerd Binnig and Heinrich Rohrer at IBM Zurich [22]. Five years later they were awarded the Nobel Prize in physics for its invention. Scanning tunneling microscopy (STM) measures the quantum tunneling current between a sharp conducting wire tip and the sample surface with a small bias voltage applied between the tip and the sample as shown in figure A.1. When the tip is brought close enough to the sample, electrons begin to tunnel through the gap from the tip into the sample or vice versa, and depending on the polarity of the bias voltage an external current can be measured. The resulting tunneling current, the detecting signal used to create an STM image, varies as an exponential function of the distance between tip and sample. If the separation between the tip and the sample changes by about an Angstrom i.e. a tenth of a nanometre, the tunneling current changes by an order of magnitude. The STM was the first instrument to images the sample surfaces with atomic resolution vertically and laterally. But typically STM is applied for conductive and semi conductive surfaces only. Lateral and vertical resolutions are 0.1 nm and 0.01 nm.

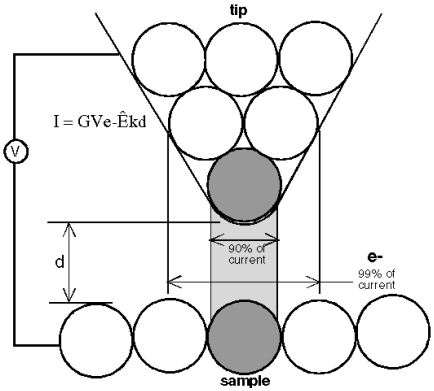

Figure A.1 Schematic of tip and sample interaction for STM [20]

A.2 Atomic force microscopy (AFM)

Atomic force microscope (AFM) probes the sample surface with a tiny sharp tip. The tip is located at the free end of a cantilever of 100 μm to 500 μm long and very thin (2 μm ~ 4 μm).. Interaction forces between the tip and the sample surface cause the cantilever to bend or deflect. A sensing element measures the cantilever deflection as the tip is scanned over the sample or the sample is scanned under the tip with the Z feedback control. The measured cantilever deflection data allow a computer to map or image the sample surface topography. AFM can be used to study insulate and semi-conductive as well as electrical conductive materials. Therefore AFM has more versatilities of application.

Several forces typically contribute to the deflection of an AFM cantilever according to the tip-sample distance. The force most commonly associated with atomic force microscopy is inter-atomic force called the van der Waals force. The dependence of the van der Waals force upon the distance between the tip and the sample is shown in Figure A.2.

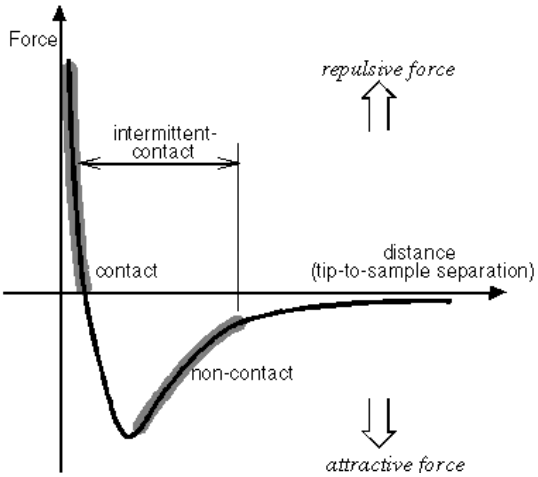

Figure A.2 force vs. distance curve [20].

There are two distance regions in figure A.2 which are contact region and non-contact region. In the contact region, the cantilever is held less than a few angstroms from the sample surface, and the inter-atomic force between the cantilever and the sample is repulsive. In the non-contact region, the cantilever is held on the order of tens to hundreds of angstroms from the sample surface, and the inter-atomic force between the cantilever and sample is attractive.

Therefore an AFM can work in contact region called Contact AFM (C-AFM) mode, non-contact region called Non-contact AFM (NC-AFM) mode and intermittent contact region called intermittent contact AFM (IC-AFM) mode.

A.3 Near-field scanning optical microscopy (NSOM/SNOM)

Near-field scanning optical microscopy (**NSOM/SNOM**) is a microscopic technique for nanostructure investigation that breaks the far field resolution limit by exploiting the properties of evanescent waves. This is done by placing a single-mode drawn optical fiber with a sub-micron aperture formed at the end very close (distance much smaller than wavelength λ) to the specimen surface, and light passing through the tiny aperture to excite the sample. This allows for the surface inspection with high spatial, spectral and temporal resolution. With this technique, the resolution of the image is limited by the size of the detector aperture and not by the wavelength of the illuminating light. In particular, lateral resolution of 20 nm and vertical resolution of 2 nm ~ 5 nm have been demonstrated [23], which is far lower than STM and AFM.

Fluorescence is the most commonly used imaging mode. Other modes include V-visible, IR, and Raman techniques etc. As in optical microscopy, the contrast mechanism can be easily adapted to study different properties, such as refractive index, chemical structure and local stress. Dynamic properties can also be studied at a sub-wavelength scale at resolutions better than 100 nm [21].

Appendix B: Self-oscillation and PLL circuit [43]

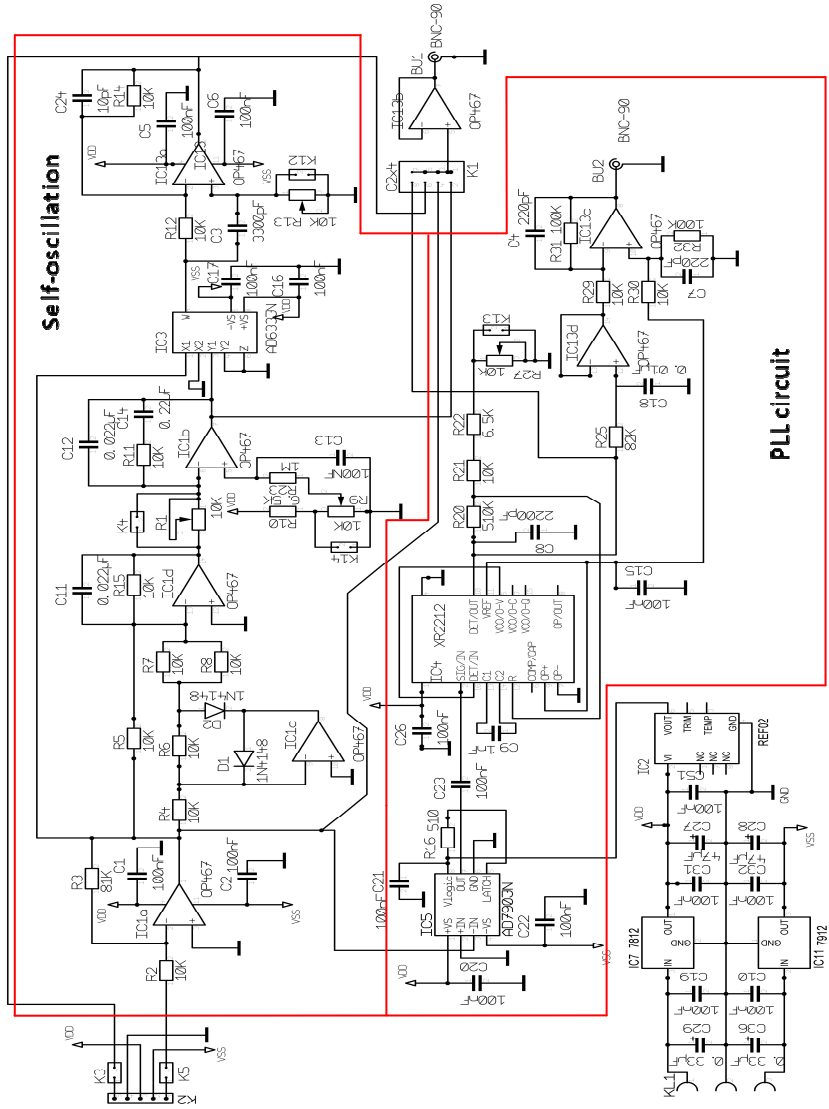

Abbreviations

Abbreviations	Full name
AEM	active encoding mode
AFM	atomic force microscope
AM	amplitude modulation
B-IGSM	Braunschweig International Graduate School of Metrology
BS	beam splitter
C-AFM	contact AFM
CD	critical dimension
CIMM	Changcheng Institute of Metrology & Measurement
CMM	coordinate measuring machine
D1, D2	photo diode 1, photo diode 2
DTU	dual-tunneling unit
FM	frequency modulation
FPS	frequency Power spectra
FPGA	field programmable gate array
HOPG	highly oriented pyrolytic graphite
HV	high voltage
HVA	high voltage amplifier
LD	laser diode
LLL	three thin crystal lamellas
MEMS	micro electromechanical system
MIT	Massachusetts Institute of Technology
NC-AFM	non-contact AFM
NNM	Nanopositioning and Nanomeasuring Machine
NPL	National Physics Laboratory
NSOM/SNOM	near-field scanning optical microscopy
PCB	printed circuit board
PEM	passive encoding mode
PI	proportional and integral
PLL	phase-lock loop
PSPD	position-sensitive photo detector
PTB	Physikalische-Technische Bundesanstalt
RIO	real-time input and output
RMS	effective amplitude
SFM	scanning force microscope, scanning force microscopy
SNR	signal to noise ratio
SPM	scanning probe microscope, scanning probe microscopy
SPPE	scanning probe position encoder
STM	scanning tunneling microscope
TF	tuning fork

References

[1] Linear Encoders http://auto-met.com/heidenhain/08PDF/NC%20Linear.pdf
[2] Magnetic encoder http://www.rls.si/default.asp?prod=LMencoders
[3] Inductosyn http://www.ruhle.com/bar_scale.htm
[4] Capacitor encoder http://www.micromo.com/n112782/i515759.html
[5] Zhang J, Cai L. Autofocus laser rotary encoder *appl. opt*. 1998, **37** 2691-95.
[6] Kao C, Lu S, Lu M. High resolution planar encoder by retro-reflection *Rev. Sci. Instr.* 2005,**76** 085110
[7] Liu C, Chen L and Wang C. Nanoscale displacement measurement by a digital nano-moiré method with wavelet transformation, *Nanotechnology* 2006, **17** 4356.
[8] Xia H, Fei Y, Fan G and Cheng F. 2D Nano-Displacement Measurement with diffraction Grating *Nanotechnology and Precision Engineering* 2007, **5**.
[9] Li J and Feldman M. A prototype optical encoder system with nanometre measurement capability, *Journal of Meodern Optics* 2010, **57** 1150-1156.
[10] Nanopositionier- und Nanomessmaschine NMM-1 http://www.sios.de/DEUTSCH/ PRODUKTE/NMM.PDF
[11] Stage Position Metrology http://www.zygo.com/?/met/markets/stageposition/zmi/
[12] Bones U and Hart M. An X-ray interferometer, *Appl. Phys. Letters* 1965, **6** 155-156.
[13] Yacoot A, Kuetgens U, Koenders L, Weimann T. A combined scanning tunneling microscope and X-ray interferometer [for grating structures calibration, *Meas. Sci. Technol.* 2001, **12** 1660-1665.
[14] Wang L, Li D, Cao M, Koenders L, Kuetgens U, Becker P, Angstrom ruler for high-accuracy pitch measurement, *Applied Optics* 2000, **39** 4535-4539.
[15] X-ray optics http://www.ptb.de/cms/en/fachabteilungen/abt4/fb-43/ag-433.html#c2124
[16] Lee J, Chen H, Hsu C and Wu C. Optical heterodyne grating interferometry for displacement measurement with subnanometric resolution**,** *Sensors and Actuators A: physical* 2007, **l 137** 185-191**.**
[17] Xia H, Fei Y, Fan G and Cheng F. 2D Nano-Displacement Measurement with Diffraction Grating *Nanotechnology and Precision Engineering* 2007, **5**. 311-314.
[18] Hsieh H, Lee J, Wu W, Chen J, Deturche R and Lerondel G. Quasi-common-optical-path heterodyne grating interferometer for displacement measurement, *Meas. Sci. Technol*. 2010, **21** 115304.
[19] Tutorial: Capacitive Position Sensors – Measuring Displacement with Sub-Nanometre Precision. http://www.capacitance-sensors.com/
[20] Howland R and Benatar L, A practical guide to scanning probe microscopy. http://web.mit.edu/cortiz/www/AFMGallery/PracticalGuide.pdf

[21] A practical guide to scanning probe microscopy http://www.veeco.com/pdfs/library/ SPM_Guide_0829_05_166.pdf

[22] Binnig G, Rohrer H, Gerber C h and Weibel E. Tunneling through a controllable vacuum gap *Appl. Phys. Lett.* 1982, **40** 178–80.

[23] Oshikane Y et al. Observation of nanostructure by scanning near-field optical microscope with small sphere probe, *Sci. Technol. Adv. Mater.* 2007, **8** 181-185.

[24] Meli F and Thalmann R. Long-range AFM profiler used for accurate pitch measurements *Meas. Sci. Technol.* 1998, **9** 1087–92.

[25] Misumi I, Gonda S, Kurosawa T and Takamasu K. Uncertainty in pitch measurements of one-dimensional grating standards using a nanometrological atomic force microscope *Meas. Sci. Technol.* 2003,**14** 463–71.

[26] Dai G, Koenders L, Pohlenz F, Dziomba T and Danzebrink H-U. Accurate and traceable calibration of one-dimensional grating *Meas. Sci. Technol.* 2005,**16** 1241–9.

[27] Kawakatsu H and Higuchi T. A dual tunneling –unit scanning tunneling microscope, *J. Vac. Sci. Technol*. 1990, **A 8** 319-323.

[28] Kawakatsu H, Hoshi Y, Kitano H, Higuchi T. Positioning and Measurement using a crystalline lattice reference scale – A feasibility study of STM application to MEMS, *Proceedings IEEE micro Electro Mechanical Systems* 1990, 197-202.

[29] Kawakatsu H, Hoshi Y and Higuchi T. Crystalline lattice for metrological applications and positioning control by a dual tunneling-unit scanning tunneling microscope, *J. vac. Sci. Technol.* 1991, **B 9** 651-654.

[30] Ohara T. A new high precision position measurement system, Ph.D. Thesis, MIT Mechanical Engineering, May 1995. http://dspace.mit.edu/bitstream/handle/1721.1/11258/34791342.pdf?sequence=1

[31] Ohara T and Youcef-Toumi K. Real-time subnanometre position sensing with long measurement range, *IEEE Robotics and Automation* 1995, 369-374.

[32] Ohara T. Scanning Probe Position Encoder (SPPE)-a new approach for high precision and high speed position measurement system, *SPIE proceeding on Annual International Symposium on Microlithography Proceedings* 2001, **4344** 552-561.

[33] Makinouchi S, Imai T, Watenabe A, Ong J and Ohara T. Introduction of SPPE-1000 scanning interference optical encoder, http://www.nanowave.com/ files/SPPE_1000_wp.pdf

[34] Aketagawa M and Takada K. 1μm range comparative length measurement using a regular crystalline lattice and a dual tunneling unit scanning tunneling microscope, *J. Vac. Sci. Technol*. 1997, **B15** 574-578.

[35] Aketagawa M, Takada K et al. Long atomic imaging over a 5-μm-long region using an ultralow thermally drifted dual-tunneling-unit scanning tunneling microscope in a thermostabilized cell, *Rev. Sci. Instr.* 1999, **70** 133-136.

[36] Aketagawa M, Kakada T et al. Real-time atomic encoder using scanning tunneling microscope and regular crystalline surface, *Meas. Sci. Technol*. 2006, **17** 513-518.
[37] Aketagawa M et al. Two-dimensional encoder with picometre resolution using lattice spacing on regular crystalline surface as standard, *Meas. Sci. Technol*. 2007, **18** 342-349.
[38] Chaikool P, Aketagawa, M and Okuyama E. A two-dimensional atom encoder using one lateral-dithered scanning tunneling microscope(STM) tip and a regular crystalline lattice *Meas. Sci. Technol.* 2009, **20** 084006.
[39] Hembacher S, Giessibl F J, Mannhart J and Quate C F. Revealing the hidden atom in graphite by low-temperature atomic force microscopy *PNAS* 2003,**100** 12539–42.
[40] Härtig F, Kniel K, Koenders L, Reinhard P. Verfahren und Vorrichtung zur Bestimmung einer Winkelteilung *Bundesrepublik Deutschland Deutsches Patent-und Markenamt* 2010.05.12, DE 10 2006 021 289 B4 http://www.ptb.de/s/c/rSUgreVx/ patentDB_Dokumente /A295.pdf
[41] Minne S, Manalis S and Quate C. Bringing scanning probe microscopy up to speed, *Kluwer Academic Publishers* 1999.
[42] Akiyama-probe guide, 2009 http://www.akiyamaprobe.com/information/downloads/
[43] Akiyama-probe technical guide, 2009 http://www.akiyamaprobe.com/information/downloads/
[44] Ferrara M. Amplitude controlled oscillator for lateral force microscopy. High sensitivity and cheap and compact design without the use of lock-in detection systems *Nanotechnology* 2003,**14** 427-432.
[45] Jersch J, Maletzky T, and Fuchs H. Interface circuits for quartz crystal sensors in scanning probe microscopy application *Rev. Sci. Instr.* 2006, **77** 083701.
[46] Qin Y, Reifenberger R. Calibrating a tuning fork for use as a scanning probe microscope force sensor *Rev. Sci. Instr.* 2007, **78** 063704.
[47] Turin George L. A introduction to matched filters *IRE Transactions on Information Theory* 1960, **6** 311- 329.
[48] Förster F, Medalia O, Zauberman N, Baumeister W and Fass D. Retrovirus envelope protein complex structure in situ studied by cryo-electron tomography, PNAS 2005, **102** 4729-34.
[49] Rana K, Singh R, Sayann K. Correlation based novel technique for real-time oscilloscope triggering for complex waveforms, *Measurement* 2010, **43** 299-311.
[50] Peter L, Heydemann M. Determination and correction of quadrature fringe measurement errors in interferometers, *Applied optics* 1981, 20 3382-3384.
[51] Sanchet-Brea L-M and Morlanes T. Metrological errors in optical encoders *Meas. Sci. Technol.* 2008**, 19** 115104.
[52] Gregorčič P, Požar T and Možina J. Quandrature phase-shift error analysis using a homodyne laser interferometer, *Optics Express* 2009**, 17** 16322-16331.

[53] Wu C and Su C. Nonlinearity in measurements of length by optical interferometry *Meas. Sci. Technol.* 1996**, 7** 62-68.
[54] Wu C, Su C and Peng G. Correction of nonlinearity in one-frequency optical interferometry *Meas. Sci. Technol.* 1996**, 7** 520-524.
[55] Eom T, Kim J and Jeong K. The dynamic compensation of nonlinearity in a homodyne laser interferometer *Meas. Sci. Technol.* 2001**, 12** 1734-1738.
[56] Kim J, Kim J, Kang C, Eom T and Ahn J. A digital signal processing module for real-time compensation of nonlinearity in a homodyne interferometer using a field-programmable gate array *Meas. Sci. Technol.* 2009**, 20** 017003.
[57] Matsui A, Shigeta Y. Development of probe-to probe approach method for an independently controlled dual-probe scanning tunneling microscope *Rev. Sci. Instr.* 2007**, 78** 106107.
[58] Hobara R, Nagarmura N, and Hasegawa S. Variable-temperature independently driven four-tip scanning tunneling microscope *Rev. Sci. Instr.* 2007**,78** 053705.
[59] Baller M, Lang H et al. A cantilever array-based artificial nose *Ultramicroscopy* 2000**, 82** 1-9.
[60] Lang H, Berger R et al. Sequential position readout from arrays of micromechanical cantilever sensors *Appl. Phys. Lett.* 1998**, 72** 383-385.

Relevant published papers and posters during PhD work

Published papers

A.1 Chen X, Koenders L, Wolff H, Haertig F. Tuning-fork atomic force microscopecantilever encoder and applications for displacement and in-plane rotation angle measurement, ***Procedia Eng.*** Proc. Eurosensors XXV, Sep. 4-7 2011, Athens, Greece.

A.2 Chen X, Koenders L, Wolff H, Neddermeyer H and Haertig F. Atomic force microscope cantilevers as encoder for real time forward and backward displacement measurements, ***Meas. Sci. Technol.*** 2011, **22** 094017 . http://stacks.iop.org/0957-0233/22/094017

A.3 Chen X, Koenders L and Haertig F. Real-time cross-correlation filtering of 1D grating position-encoded signal, ***Meas. Sci. Technol.*** 2011, **22** 085105. http://stacks.iop.org/0957-0233/22/085105

A.4 Chen X, Koenders L, Wolff H, Haertig F and Schilling M. Atomic force microscope cantilever as an encoding sensor for real-time displacement measurement ***Meas. Sci. Technol.*** 2010, **21** 105205. http://stacks.iop.org/0957-0233/21/105205

A.5 Chen X, Wan Y, Koenders L and Schilling M. Measurements of dimensional standards and etalons with feature size from tens of micrometres to millimetres by using sensor strengthened nanomeasuring machine, ***Measurement*** 2010, **43** 1369-1375. http://dx.doi.org/10.1016/j.measurement.2010.07.014

A.6 Yang T, Zuo Y, Chen X. Auto-focus technology and its application based on image processing, ***Computer Simulation*** 2009, Vol 26, No. 7. (Chinese Journal) http://d.wanfangdata.com.cn/Periodical_jsjfz200907065.aspx

A.7 Chen X, Ma X, Zhu Z, Yang D. Development of SFM of probing sensor look-alike, ***Journal of Electronic Measurement and Instrument***, Vol.22 No. Z2, 359-365, 2008 (Chinese Journal). http://cspm.cn/papers/280.pdf

Conference Posters

B.1 Chen X, Koenders L, Wolff H, Neddermeyer H and Haertig F. Atomic force microscope cantilevers as encoder for real-time two direction displacement measurement, NanoScale 2010, Oct 27-29, Brno, Czech Republic

B.2 Chen X, Koenders L, Wolff H, Haertig F and Schilling M. Tuning fork AFM as a sensor for real time one directional translation displacement measurement and control, UK SPM conference, 30th June -1st July 2010, ExCeL, London.

B.3 Chen X, Koenders L, Wolff H, Haertig F and Schilling M. AFM as a sensor to detect translation, UK SPM 2009, 24-25 June 2009, National Physical Laboratory (NPL), UK.